DOE/ER/53269--T1

Final Documentation on DOE Contract 88ER53269
Methods for Testing Transport Models

Enclosed from today's thesis defense is a document fully supported by and representing final documentation of results obtained under DOE Contract 88ER53269. The work described here substantially advanced the state of the art in applying theoretical transport models to simulation of experimental data and analysis of the probability of achieving desired performance in planned tokamak experiments. Most notably, within the context of a very carefully defined set of assumptions, this work produced a rather modest probability of achieving a sustained thermonuclear burn in the Conceptual Design Activity (CDA) version of ITER, but a formally quite high probability of achieving this in with Engineering Design Activity (EDA) parameters. When considering future policy, it could be well worth while for the Magnetic Fusion Energy program to review both the historical role played by the work under this contract in renewing interest in application of theory-based tokamak transport models to analysis of experiments and machine design, and the reasons why the results appear to differ from recent widely discussed theoretically based transport studies of ITER ignition by another group.

We started this work in the context of a broad-based skepticism concerning the utility of computational transport models based on detailed theories. Princeton had abandoned simulation of experiments based on an older so-called ``six-regime" approach based on early theories of drift waves, and Oak Ridge had apparently concluded that a resistive ballooning theory had at best limited utility in describing certain experiments on ISX-B. By carefully coordinating our work with an ongoing review of transport model theories, however, we were able to evolve an integrated theory of flux-surface averaged transport. Combined with statistically systematic calibration of turbulence saturation levels and a systematically calibrated physically based empirical model of boundary conditions appropriate to a location very near the outermost "closed" flux surfaces, this provided a single model which incorporated detailed theory and did an unexpectedly good job of simulating a wide variety of experimental data without any case-by-case adjustment of parameters. This approach recognized that any theoretical treatment inevitably involves some approximations which leave the theory with a priori uncertainty before it is tested against experimental data. The calibration procedures we developed provided a systematic method for reducing this uncertainty by calibration against experimental data. It is a tribute to the vision of those in the Office of Fusion Energy who provided support for this work that we were able to carry through with such an ambitious program to the extent documented in the enclosed thesis.

Especially during the early stages of this work, the pace at which a similarly systematic database collection and statistical calibration effort was proceeding elsewhere was admittedly frustratingly slow. Work funded under our contract concentrated on carefully with multiple experimental teams on collection of appropriately time-sequenced data and repeatedly presenting examples of systematic experimental calibration of theoretical transport models at transport workshops and other meetings. Part of this work has now been emulated and extended using larger databases and more recent transport theories. With respect to systematic use of appropriate statistical methods and calibration of boundary conditions, however, some recently reported work has yet to meet use as systematic an approach as reported in the accompanying thesis. Progress along these lines could go a long way towards reducing unnecessary confusion concerning why different approaches appear to give different results. Of particular importance in this regard is a systematic and credible model of uncertainties resulting from the many approximations inevitably involved in moving from a basic theoretical formulation to a simulation of actual experiments, much less a prediction of the probability of achieving a given level of performance within the context of a well defined set of assumptions about the configuration of a future experiment.

The support of the Office of Fusion Energy for the work summarized here is much appreciated, and I hope that you will have the opportunity to reflect on these comments and use them to your advantage in planning future work.

16 September, 1997
Clifford Singer
Prof. Nuclear Engineering

DISCLAIMER

MATHEMATICAL MODELING PLASMA TRANSPORT IN TOKAMAKS

BY

JI QIANG

B. S. University of Electronic Science and Technology of China, 1991
M.S., University of Illinois, 1995

THESIS

Submitted in partial fulfillment of the requirements
for the degree of Doctor of Philosophy in Nuclear Engineering
in the Graduate College of the
University of Illinois at Urbana-Champaign, 1997

Urbana, Illinois

ABSTRACT

In this work, we have applied a systematic calibration, validation and application procedure based on the methodology of mathematical modeling to international thermonuclear experimental reactor (ITER) ignition studies. The multi-mode plasma transport model used here includes a linear combination of drift wave branch and ballooning branch instabilities with two a priori uncertain constants to account for anomalous plasma transport in tokamaks. A Bayesian parameter estimation method is used including experimental calibration error/model offsets and error bar rescaling factors to determine the two uncertain constants in the transport model with quantitative confidence level estimates for the calibrated parameters, which gives two saturation levels of instabilities. This method is first tested using a gyroBohm multi-mode transport model with a pair of DIII-D discharge experimental data, and then applied to calibrating a nominal multi-mode transport model against a broad database using twelve discharges from seven different tokamaks. The calibrated transport model is then validated on five discharges from JT-60 with no adjustable constants. The results are in a good agreement with experimental data. Finally, the resulting class of multi-mode tokamak plasma transport models is applied to the transport analysis of the ignition probability in a next generation machine, ITER. A reference simulation of basic ITER engineering design activity (EDA) parameters shows that a self-sustained thermonuclear burn with 1.5 GW output power can be achieved provided that impurity control makes radiative losses sufficiently small at an average plasma density of $1.2 \times 10^{20}/m^3$ with 50 MW auxiliary heating. The ignition probability of ITER for the EDA parameters can be formally as high as 99.9% in the present context. The same probability for concept design activity (CDA) parameters of ITER, which has smaller size and lower current, is only 62.6%. This suggests that EDA parameters for ITER tokamak are very likely to achieve the self-sustained thermonuclear reaction, but CDA parameters are risky for the realization of ignition.

ACKNOWLEDGMENTS

The author wishes to express a sincere thanks to Dr. Clifford E. Singer for his gracious support, instructive guidance, and constant encouragement. Also, I would like to thank Drs. J. E. Kinsey and T. Djemil for many useful discussions and providing of data. In addition, I am grateful to Junli Zhang, my wife, for her enduring patience and continuing love.

This work was supported by the United States Department of Energy, under contract No. DE-FG02-88ER53269.

Contents

Chapter 1

Introduction

Mathematical modeling has been widely applied in engineering, physics, biology and social science. It is a systematic process to effectively model real world systems. Although detailed processes vary in modeling different systems, a general methodology could be used to guide the building of mathematical model. This includes system identification/characterization, mathematical model formulation, analysis of mathematical formulation, parameter estimation and model validation. An iterative procedure will be used in most situations to obtain a satisfactory model.

Thermonuclear fusion has been known as a great potential renewable energy resource for many decades. However, the self-sustained thermonuclear fusion has not yet been achieved except for the first explosive thermonuclear reactions in hydrogen bombs. A number of concepts and experimental devices related to controlled (non-explosive) fusion have been proposed and tested. The tokamak is the most promising candidate device among these to achieve controlled thermonuclear reactions. This is because this device, in principle, can provide a closed magnetic field to confine the plasma inside the container, in contrast of the open magnetic field in the device like magnetic mirror. The closed magnetic field helps to avoid the open end loss of electrons and ions. A schematic diagram of tokamak is shown in Fig. 1.1 [1]. It is characterized by a large toroidal vacuum field, generated by external coils, and a

smaller poloidal magnetic field generated by the toroidal plasma current. The torodial field helps to stabilize the plasma, and the poloidal field helps to confine the plasma in the tokamak.

To achieve a controlled self-sustained thermonuclear fusion, i.e., ignition, plasma with sufficient density needs to be heated for high enough temperature and confined for a long enough time. However, this is restricted by outward transport of plasma which results in substantial energy and particle losses to the wall, and cools the plasma before it reaches ignition. A successful model of plasma transport in tokamak will provide a good understanding of energy and particle loss processes in tokamak plasmas. This also provides an instructive guide for future machine design.

Studies of plasma transport inside tokamak have been done following three directions to account for the inherent complexity of plasma transport phenomena. Empirical study based on experimental data has used "scaling laws" to study the energy confinement time of plasma inside tokamaks [2, 3, 4, 5, 6, 7, 8, 9, 10, 11]. The energy confinement time is expressed as function of the plasma discharge parameters with a priori uncertain constants. These constants are determined by calibrating against experimental data. The empirical scaling law provides a direct relationship between operation parameters and plasma parameters. It is helpful to use such scaling law to study the tokamak discharge with the similar condition to the machine against which the empirical law is calibrated. Various scaling laws based on the different tokamak experimental data have been obtained [12, 13, 14, 15, 16]. As tokamak confinement conditions vary among different discharges, these empirical laws are usually divided into Ohmic heating, L mode (low confinement) and H mode (high confinement) scaling laws [17, 18, 19, 20]. It is risky to extrapolate these scaling laws beyond the respective experimental operational regime to predict the performance of larger machine like ITER (international thermonuclear experimental reactor) without a proper understanding of the fundamental physics of plasma transport.

Semi-empirical studies have tried to understand plasma transport in the tokamaks using general physical considerations and experiment data. Semi-empirical transport models are constructed from the dimensionless parameters with appropriate dimensional constraints. This methodology has applied to transport study and

achieved some modest results [21, 22, 23, 24, 25, 26, 27]. Unfortunately, it is still questionable to extrapolate these results to the larger machine design since there is no high-field tokamak with geometry which can be scaled to a machine like ITER with all relevent dimensional parameters fixed [28]. It is therefore important to identify the underlying transport mechanism of the tokamak plasma to make a better extrapolation.

Theoretical studies based on a more detailed physical background, such as kinetic theory and fluid model, have been done to gain better understanding of plasma transport in tokamaks. These models are also called theory-based transport models or predictive transport models. Neoclassical transport theory considering non-turbulent particle interations in the toroidal geometry was first used to study plasma transport in tokamaks [29, 30, 31, 32]. Experimental observations showed that radial electron energy and particle transport inside tokamak can be much larger than the prediction from that theory [33]. These differences are believed to be due to the so-called anomalous transport caused by the turbulent instabilities in the tokamak plasma. The sources of free energy to drive such instability can be expansion free energy, which arises from the plasma pressure gradient, velocity space free energy, which arises from the non-Maxwellian distribution in velocity space, and magnetic free energy, which arises from non-uniformity of magnetic field energy density [34]. A number of instability-driven transport models have been studied to account for anomalous transport. In these theory-based transport models trapped electron mode, ion temperature gradient mode (η_i), resistive ballooning mode, kinetic ballooning mode, rippling mode, tearing mode have been proposed to account for anomalous transport [35, 36, 37, 38, 39, 40, 41, 42, 43]. (Here $\eta_i = d\log T_i/d\log n_i$ where T_i and n_i are the ion temperature and density respectively.) So far, no single one of these theory-based transport models can reproduce the whole experimental database [44, 45, 46, 47]. One approach to dealing with this problem is to generalize the theories, e.g. by including self-consistent calculation of particle and thermal transport for both hydrogen and impurity species and using nonlinear simulation results from gyro-kinetic or gyro-Landau simulation [48, 49, 50, 51, 52, 53, 54, 55].

A complementary approach is to include more than one turbulent-driven

transport mechanism in the transport model [56, 57, 58]. A common component of such an approach is a drift wave model which includes effects from trapped electron, ion temperature gradient and circulating electrons. This model by itself gives a poor current scaling for the global energy confinement and a reduced transport at the plasma edge, both of which contrast with experiment data [45]. Ballooning modes reproduced some experimental data from ISX-B [103], but recasting this model solely in terms of local plasma parameters later led to a significantly poorer fit to the data [44]. This model also has a strong scaling with toroidal field, a scaling which is not apparent in global energy confinement data. Generally, at low β (β = thermal energy/magnetic energy), the drift wave branch seems to dominate anomalous transport, while at high β, ballooning branch instability may dominate the anomalous transport [60].

The multi-mode tokamak transport model including both drift wave and ballooning instabilities was suggested in Ross et al.'s report [45] and further worked out by Singer [61]. In the previous work, Ghanem used a multi-mode transport model including drift wave and resistive ballooning modes to study the saturation of energy confinement time at high density for Ohmic phase plasma, and to obtain a scaling law for the energy confinement time with various plasma parameters [62, 63]. Bateman applied a similar model to simulate L-mode temperature profiles and the so-called supershot discharges in TFTR [60, 64]. Redi used a similar transport model to study a current scaling experiment on TFTR[65, 66]. Park studied statistical methods for parameter estimation and designed an analytic "code emulator" for energy confinement time based on prediction from the transport model [67]. Djemil tested essentially the same transport model against L-mode energy confinement time data [68]. Kinsey developed this transport model for simulating the time-dependent H-mode discharge in tokamak [69]. He also tested a more complete multi-mode model which includes additional kinetic ballooning and neoclassical MHD modes in the ballooning branch, determined a group of transport coefficients using a maximum likelihood method, simulated a series of dimensionally similar experiments and compared a new drift wave mode and kinetic mode with the model used in this study [70, 71, 72, 73].

The previous works laid a good foundation for systematically studying the

multi-mode transport models. In the present work, we apply the methodology of mathematical modeling to the study of plasma transport in several tokamaks using a theory-based multi-mode transport model. This model is derived from Kinsey's nominal multi-mode study [70]. A Bayesian parameter estimation method is used including experimental calibration error/model offsets and error bar rescaling factors to determine the two saturation levels in the multi-mode transport model with quantitative confidence level estimates for the calibrated parameters [74]. A trial application to the calibration of a gyroBohm multi-mode transport model with testing on a pair of DIII-D discharges shows the effectiveness of the Bayesian estimation method [75]. This method is then applied to calibrating the nominal transport model used by Kinsey et al. against a broad database using twelve discharges from seven different tokamaks [76]. The calibrated transport model is then tested on five discharges from JT-60 with no adjustable constants. The results showed a good agreement with experimental data [77]. Finally, the resulting class of multi-mode tokamak plasma transport models is applied to the transport analysis of the ignition probability in a next generation machine, ITER [78]. A reference simulation of basic ITER engineering design activity (EDA) parameters shows that a self-sustained thermonuclear burn with 1.5 GW output power can be achieved provided that impurity control makes radiative losses sufficiently small at an average plasma density of $1.2 \times 10^{20}/m^3$ with 50 MW auxiliary heating. The ignition probability of ITER for the EDA parameters can be formally as high as 99.9% in the present context. The same probability for concept design activity (CDA) parameters of ITER, which has smaller size and lower current, is only 62.6%. These results are qualitatie in agreement with the other ITER physical study and support the conclusion from ITER expert team [79, 80, 81], except the results from a Texas/PPPL study, which used a somewhat different methodology [82].

In the following chapters, the methodology of mathematical modeling is discussed in Chapter 2; the theoretical plasma transport modes in the multi-mode model are introduced in Chapter 3; the numerical method used for the solution of transport equation is described in Chapter 4; the methods of parameter estimation are introduced in Chapter 5; a gyro-Bohm multi-mode transport model is tested in Chapter 6; a nominal muti-mode transport model is calibrated against a wide

range of tokamak database in Chapter 7; the calibrated multi-mode transport mode is verified using the JT-60 discharges in Chapter 8; an application of the calibrated multi-mode tokamak transport model is done in Chapter 9; and conclusions are drawn in Chapter 10.

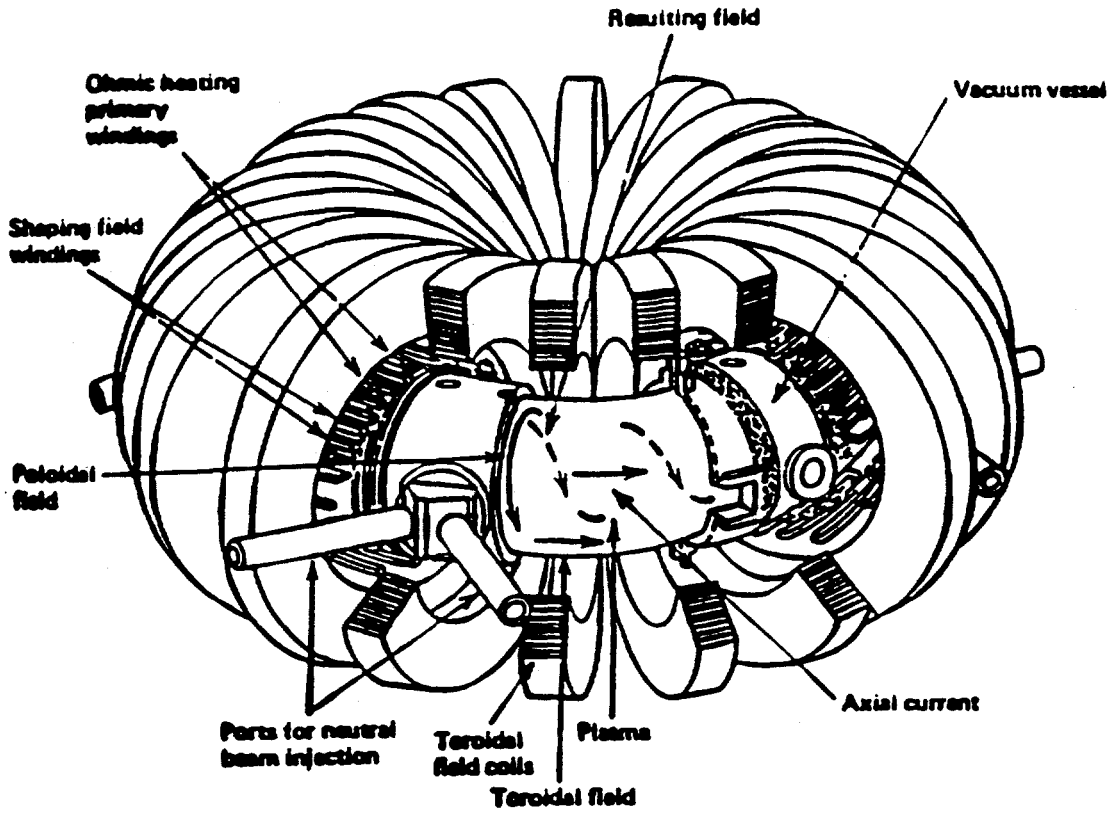

Fig. 1.1: **Tokamak schematic.**

Chapter 2

Methodology of Mathematical Modeling

Mathematical modeling is an art as well as a science. It involves not only the use of various types of techniques for problem solving, but also the use of personal experience and intuition. A good modeller needs to have a good knowledge of mathematical techniques for solving the well-defined mathematical equations. He also needs to have good experience and creative intuition in grasping the heart of problem, selecting an appropriate solution method and an correctly applying a model. A successful mathematical model is ideally the masterpiece of a competent modeller.

There is no single complete theory of mathematical modeling to treat all problems encountered in physics, chemical, biology and socio-economics. Each system has its own features of problem definition, validity of a quantitative model and procedure for making inferences. However, this does not imply that there is not a general procedure to guide the process of mathematical modeling. A systematic procedure has been suggested by Rodin et al. [83] and is shown in Figure 2.1. Some similar procedures have been used by other authors [84, 85, 86, 87, 88, 89, 90, 91]. In this work, we define a relatively simple procedure based on the procedure given in Figure 2.1. This procedure is system identification/characterization, mathematical modeling formulation, analysis of the mathematical formulation, parameter estimation and model validation.

In the following sections, we will discuss system identification/characterization in Section 1, mathematical modeling in Section 2, analysis of the mathematical formulation in Section 3, parameter estimation in Section 4, and model validation in Section 5. A summary is given in Section 6.

2.1 System Identification and Characterization

System identification/characterization is a process associated with the real world problem. Here, the real world is viewed as a system. System identification includes setting a realistic goal and understanding the qualitative behavior of system. System characterization will simplify or idealize the system so that the unimportant information is eliminated and important characteristics of a system are retained in the model. System identification/characterization lays a foundation for model building.

The goal of modeling may be set before the start of mathematical modeling. However, a realistic goal of system modeling has often to be reconsidered or reset during the building of a model. To set a goal, one needs to define the problems to be solved for a particular system, to decide upon the objects or aspects in the system to be studied and to limit the range of system under study. In the nomenclature used here, an object is a physical entity with specific characteristics or attributes. An aspect is an attribute of an object in a system. A system is composed of a large number of objects with many aspects. Any real world system is also connected to the outside world. The outside world of a system is called the environment of the system under study. The range of the system is the boundary which separates the system from its environment.

Some qualitative behaviors of a system can be understood by observations or preliminary experiments. The characteristic behaviors are called the properties of the system. These properties can be static or dynamic, deterministic or stochastic etc.. Qualitative study of system behavior will give some understanding of the properties of system and the relations in the system. This study gives not only a good direction for setting a modeling goal, but also serves as a basis for quantitative mathematical formulation and validation. The deeper the understanding of a real system, the better

the model will be.

A static system is a time-independent system. The state of system at different time points is only concerned with conditions of system at that time. A dynamic system is a time-dependent system in which time plays a significant role. The time enters into cause-effect interactions. The state of system at one time will not only depend on the conditions of system at that time but also on the state of system before. Understanding time scales in the dynamic system is helpful for modeling the system effectively. Time scale analysis is used to indicate the duration for significant changes to occur in the system. In some cases, if the time scale of system is large, the system may be assumed to be a static system.

A system is said to be deterministic if the behavior of system in the future can be determined completely with present or past behavior of system. If the future of system can not be predicted with certainty, we say such a system is a stochastic system. A deterministic system is said to have a strong cause-effect relation. In the real world, there are always some uncertainties. If the uncertainty is insignificant, it can be ignored and the system can be treated as a deterministic system. Otherwise, the uncertainty must be taken into account during system identification.

The "relation" of the system consists of the internal relation and external relation. The internal relation includes all interactions among objects and their attributes in the system. This is governed by the inherent mechanisms of system. These mechanisms may be described by some underlying theories, which lay the foundation of quantitative formulation. The external relation is the interaction between the system and its environment. The system is said to be a closed system if there is no interaction between the system and its environment and an open system if there is. These interactions set up the constraints or boundary conditions for mathematical modeling of the system.

System characterization simplifies and idealizes the real world system. The real system contains a lot of information which is not all needed in mathematical modeling. Data needs to be collected and the necessary data sorted out. To build a practical model, one has to decide what material is needed in order to successfully model the system. If all the detailed parts of system are taken into account in the

model, it can become too powerful and complicated to be solvable using practical facilities. On the other hand, if it is too simple, then some important aspects of system may be lost in the model. The key point is to grasp the heart of system, that is, the salient features of system. These features include the dominant objects and attributes, and dominant relationships and mechanisms. One conventional way is to start from a simple model and generalize to more detailed and powerful mathematical modeling of system. There are several alternative methods, such as schematic or graph-theoretic or matrix, for system characterization representations [83]. These methods are compact and elegant representations because they present the problem in a form that is easier to comprehend, and they can facilitate the first conceptual step towards mathematical model building.

2.2 Mathematical Modeling Formulation

Mathematical modeling formulation is a process for translating a qualitative description derived from system identification/characterization into quantitative mathematical expressions. The objects or the attributes of objects studied are related to variables in mathematical formulas. The theory governing the interactions among the objects and attributes is expressed in abstract mathematical expressions. The relationship between the system and the environment is turned into boundary conditions or constraint conditions in the mathematical formulation. Depending on the qualitative behavior of the system, the formulation of mathematical model can be classified as a deterministic and stochastic formulation, as noted above. Each of these two categories can be sub-divided into static and dynamic formulations. There may be several useful mathematical formulations of model for the same real situation.

A static formulation for a deterministic system is a time independent formulation which involves either a function or function equation with one or more variables. The function formulation has the form

$$\Omega(F(x,\theta)) \tag{2.1}$$

where Ω is an operator on a function F, such as maximizing or integration. The

function equation formulation has a form

$$F(x, y, \theta) = 0 \tag{2.2}$$

where, x represents the input variables, y represents the output variables, θ is a set of parameters and F is a mathematical function. The variables in the formulation can be vector or scalar, continuous or discrete, and constrained or unconstrained. For continuous variables, the function F can be a function of time-independent differential operators. This gives time-independent differential equations. Boundary conditions are required to obtain the solution of this type of function equation. If variables x and y appear linearly in F, the equation is said to be linear, otherwise it is nonlinear.

The dynamic formulation of a deterministic system is a time dependent formulation. It has similar functional form to the static formulation except that $F \sim F(t, x, y, \theta)$, where t is the time. When the variable is continuous, F can be a function of a time-dependent differential operator. Such a function form is called the partial differential equation. Initial and boundary conditions are needed to solve this type of function equation.

In a stochastic system, the uncertainty is significant. Random variables are used to model the uncertainties in the system. A random variable is defined as a function which map a random event to a real number. It is characterized through a distribution function. In the static formulation, the distribution function has the form

$$F(x, \theta) = prob\{X(\omega) \leq x\} \tag{2.3}$$

In the dynamic formulation, the distribution function has the form

$$F(t, x, \theta) = prob\{X(t) \leq x\} \tag{2.4}$$

In above expressions, X is a random variable, x is the real number corresponding to that random variable and θ is the parameter. The random variable in the distribution function can be either a scalar or a vector, either continuous or discrete, and either constrained or unconstrained. The formulation can be analyzed mathematically by analysis of variance and regression.

2.3 Analysis of Mathematical Formulations

Once the mathematical model formulations have been constructed, the next step is to analyze and solve these mathematical formulations. This process is a pure mathematical process. A large variety of mathematical techniques can be used to solve such problems. However, before one starts the quantitative solution process explicitly, some qualitative analyses of the underlying structure of the mathematical formulation is instructive. These analyses can help to identify some qualitative properties of solutions like existence, uniqueness, symmetry and periodity. In some cases, the range of solution may be narrowed, and the limiting trend of a solution can be obtained.

As mathematical formulations in deterministic and stochastic systems differ, there exist different techniques for analyzing each. For a deterministic system, one typical analytical method is dimensional analysis [92, 93]. The basic idea underlying this method is to non-dimensionalize the origin formulation by replacing the original variables and parameters in the formulation using a set of new dimensionless variables and parameters. The resulting formulation may be simpler and easier to solve. When an exact solution is not obtainable, a perturbation method may be used [94]. The idea of a perturbation method is to approximate the true solution by power series expansion using parameters in the formulation. Computational methods provide another approximate solution for complicated formulations. In the computational method, all continuous variables are approximated by the finite discrete numbers on a computer. Mathematical functions are decomposed into simple operations on numbers using a computer language. If the function forms in the mathematical formulation are complicated, then the corresponding concrete numerical algorithms are also complicated. However, most of these numerical algorithms will eventually reduce into solving the groups of algebraic equations, which can be done very effectively using computers.

For a stochastic system, the primary aim is to get the probability distribution function of random variables in the formulation. In the analytical approach, the distribution function is obtained by solving the mathematical formulation for random variables using analytical techniques. This can be done only for a small class of formulations. In such cases, moment analysis or Laplace transformation may be

useful [83]. When it is difficult to obtain exact analytical solutions, one can resort to obtaining analytical expressions for lower and upper bounds to the variables of interest. This usually requires less effort than for the exact solution. Computational method can also be employed in stochastic systems. A direct computation simulation is can be useful for such systems. Here the stochastic process is simulated by generating random events at different time point of process on the computer. Repeating this simulation a large number of times one can give adequate statistical information about the random process. The probability distribution function can be estimated from these information. This method provides an alternative way to simulate a real world system [95, 96].

2.4 Parameter Estimation

In the above discussion, we saw that a parameter here called, θ, was often used in the mathematical modeling formulations. To solve such formulations using computational method, the parameter needs to be set to definite value. Parameter estimation is a process of finding the most appropriate value in the mathematical formulations. Once the parameter is set, the model behavior is defined.

To obtain an estimator of a parameter in the formulation, outcomes from the real world system are required. These outcomes serve as the data base for the parameter estimation. When the amount of data increases, the estimators change. Ideally, the estimate should tend to the true value of parameter θ with increasing amount of data. More precisely, when the estimate converges in probability to the true value as number of data approaches infinity, the estimate is said to be a consistent estimate and the estimator a consistent estimator. Another sufficient condition for the estimator to be consistent is that the mean of the estimator tends to the true value and the variance of estimator tends to zero as the number of data sets approaches infinity [97]. An estimator is said to be unbiased if the mean of of estimator is equal to the true value. The smaller its variance is, the more efficient an unbiased estimator is.

There are a variety of methods for parameter estimation, such as least

squares, maximum likelihood and maximizing a posterior function [98, 99]. The least squares method is an estimate method which minimizes the sum of the square deviation between the model output and system outcome. The maximum likelihood estimation is a method which maximizes the likelihood function given a particular set of data. The maximum posterior function estimation maximizes a posterior distribution function of a parameter with given data.

2.5 Model Validation

After analysis of mathematical model formulations, model results are interpreted and compared with real system outcomes. Model validation is required to test the adequacy of a given mathematical model. It involves the definition of a testing criterion to judge whether a model is adequate or not. The test criterion illustrates the degree of agreement between the model and the system behavior. If a model passes the test, it can be taken as an adequate model for the goal of modeling. This mathematical model can be further implemented to solve the original problem or help future planning of system with confidence. Otherwise, one has to back-track check and start a new iteration in the modeling process. However, the definition of test criterion is a hard task. If the criterion is too stringent, more iterations of modeling will be needed to pass the test. This generally results in a more complicated mathematical model and more cost for modeling. On the other hand, if the criterion is not stringent enough, any model may pass the test. This results in the over-simple representation of system features and application of models with poor confidence. Therefore, the degree of stingency of test criterion must be a trade-off between the complexity of a model and the agreement between the model and real world system based on modeller's experience and intuition.

Conventionally, three approaches to model validation have been used. These are testing the model assumptions, testing the model behavior, and a combination of these two approaches. Testing model assumptions is used to determine the degree of inadequacy of a model by critically examining the basic assumptions made during the modeling. It is justified according to the logic that if the assumptions are invalid

then the agreement between the model and real system is doubtful. Testing the model behavior is used to check the adequacy of model by comparing the model output with the real system outcome. The logic of this method is that if results are correct then the premises should be adequate at least from an empirical point of view. This provides a indirect test of assumptions. Rigorous statistical method is used to test the hypothesis from model by comparing with real world data [100]. This gives the critical region of allowed hypothesis at given significance level.

2.6 Summary

In the above discussion, the procedure of mathematical modeling is stated in a linear sequential order. However, in the practice, these steps are not isolated but are interconnected during the mathematical modeling. The solution of a mathematical formulation is checked using the results from the system identification/characterization; validation is tested during the mathematical formulation; and nominal parameter estimation is done before the mathematical analysis. An optimum mode of mathematical modeling is to focus on one step but consider the implications, possibilities and limitations arising in other preceding and succeeding steps of modeling. A systematic methodology for mathematical modeling is critical for successful model building.

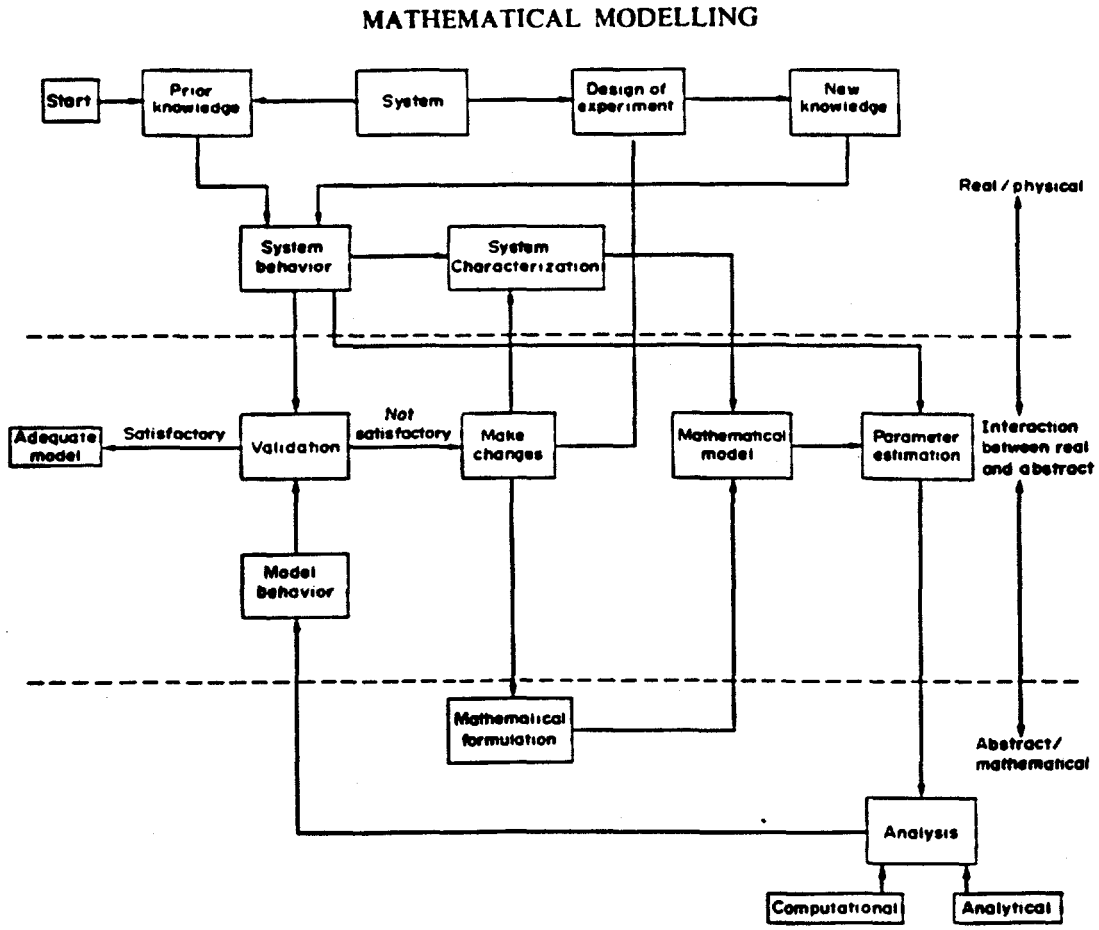

Fig. 2.1: The model building process (detailed).

Chapter 3

Theoretical Plasma Turbulence Modes in the Multi-mode Model

In the multi-mode model, anomalous transport fluxes from two branches of the linear dispersion relation are linearly combined with a priori uncertain multipliers. One is the ballooning branch, and the other is the drift branch. This chapter will qualitatively discuss the physics behind these two branches. In the following sections, the ballooning branch is discussed in Section 1, and the drift wave branch in Section 2.

3.1 Ballooning Branch

The ballooning branch transport fluxes used here are composed of contributions from resistive ballooning modes, kinetic ballooning modes and neoclassical MHD modes. The resistive ballooning and neoclassical MHD modes were derived using nonlinear turbulent saturation level estimates by balancing the driving force against dissipation. The kinetic ballooning modes used here are most relevant to the high β regime and require the inclusion of a quasilinear estimate of kinetic effects.

3.1.1 Resistive Ballooning Mode

Ballooning instability is driven by a pressure gradient localized in the region of unfavorable magnetic field line curvature. Magnetic field line curvature is said to be favorable where magnetic field lines are convex to the plasma. The perturbation is then stabilized by the tension of field lines. Where the field lines are concave toward the plasma, their tension tends to make them shorten and collapse inward. The plasma pressure, on the other hand, has a tendency to expand outward. Perturbations interchanging flux tubes at different radii can lead to lowering the plasma potential energy and cause instability. In such a case, the field line curvature is said to be unfavorable. In the region of bad field line curvature, the stabilizing energy from field line tension is weakest, and a perturbation can be amplified by the pressure gradient. In a torus, a given field line passes through unfavorable curvature in the outer side of torus and favorable curvature in the inner side of torus. Thus, a perturbation is not constant along the magnetic field lines. It can concentrate in the unfavorable curvature region and lead to a ballooning instability, which is called a ballooning mode. Such an instability has long wavelength along the magnetic field and short wave length perpendicular to the field. Ballooning mode makes the plasma bulge out most where both the pressure gradient and field line curvature are strongest. Hence, instability is usually strongest in the outer edge of plasma. In a tokamak with average favorable curvature, ballooning instability is the results of driving pressure gradient and unfavorable curvature overwhelming the stabilizing of favorable curvature. In ideal MHD analysis, the plasma is assumed to be a perfect conductor along magnetic field lines, and the magnetic force acting on the plasma is infinite. Magnetic field lines are frozen in the plasma and the magnetic fluxes are preserved. Radial diffusion across the magnetic field requires a large pressure gradient to break the strong restoring force from field line bending, which sets an upper limit on β, where β is the ratio of plasma pressure to magnetic pressure. Instability will not be excited if β is less than β_c, which is approximately a/Rq^2[34]. In this expression a is minor radius, R is major radius and q is safety factor. The exact stability limit on β depends not only on geometric

parameters, e.g., the aspect ratio and cross-section shape, but also on internal plasma parameters, e.g., the pressure profile and the q profile.

In reality, plasma has a nonzero resistivity. Particles can move across the field lines and ballooning modes may be excited even if β is less than β_c. The presence of resistivity can result in the formation of magnetic islands. Magnetic field lines are broken and reconnected around these regions. The particles move along these open field lines rapidly and cause a great loss of energy. In past decades, the resistive ballooning mode has been studied extensively using an energy principle, eigenfunction analysis and nonlinear simulations [39, 43, 40, 101, 102]. For this mode used in the present study, we employed the flux formulas given by Carreras and Diamond [103].

Carreras' mode is based on a group of reduced linearized resistive MHD equations in cylindric geometry.

$$\frac{\partial \psi}{\partial t} = -R_0 \nabla_{\|} \phi + R_0 \eta J_z \tag{3.1}$$

$$\frac{\partial U}{\partial t} = \frac{1}{\rho_m}(-\nabla_{\|} J_z + Z \cdot (\nabla \Omega \times \nabla \tilde{p})) + \mu \nabla_{\perp}^2 U \tag{3.2}$$

$$\frac{\partial \tilde{p}}{\partial t} = \chi_{\perp} \nabla_{\perp}^2 \tilde{p} - V_r \frac{\partial p_0}{\partial r} \tag{3.3}$$

Here ψ is the poloidal flux, ϕ the velocity stream function, and $p = p_0 + \tilde{p}$, where p_0 is the time-averaged pressure and $\tilde{p}$ the fluctuating part. $U = \nabla_{\perp}^2 \phi$ is the vorticity, and $J_z = \nabla_{\perp}^2 \psi / (\mu_0 R_0)$ is the current parallel to the z-axis of the cylinder. The constant μ_0 is the vacuum permeability. The convective derivative is

$$\frac{d}{dt} = \frac{\partial}{\partial t} + V \cdot \nabla \tag{3.4}$$

with the velocity given in terms of the stream by $V = \nabla \phi \times Z$, and the derivative along the magnetic field lines is $\nabla_{\|}$, where

$$\nabla_{\|} f = \frac{1}{R_0}(Z \times \nabla \psi) \cdot \nabla f + B_0 \frac{\partial f}{\partial z} \tag{3.5}$$

and B_0 is the magnetic field along the z-direction, which we assume to be constant. The coefficients η, μ and $\chi_{\perp}$ are the collisional resistivity, viscosity, and cross-field thermal transport coefficients, respectively. They multiply the corresponding dissipative terms in Eqs. (1) - (3). Finally, ρ_m is the constant mass density. The first

equation was derived from the Ohm's law, the second equation comes from the momentum equation with viscosity and resistive dissipation, and the third equation comes from the equation of state with incompressible assumption. Equations (1) - (3) constitute the basic equations for a resistive ballooning mode study. A saturation condition is imposed by setting all time derivatives equal to zero. This condition requires the turbulence level to be high enough so that energy outflow from fluid viscosity and pressure diffusivity is sufficient to stabilize the mode. The fluctuation level can be evaluated from balancing the nonlinear diffusion with the driving term. After some involved calculations, the particle and thermal diffusivities from $E \times B$ drift can be obtained as

$$D_a^{EB} = \chi_e^{EB} = v_e \gamma_{(m)}^{(0)} (W_{(m)}^{(0)})^2 \lambda^2 \tag{3.6}$$

$$= \Lambda^2 \frac{\beta R_0^2 q^2}{\sqrt{2} L_p R_c \hat{s}} \frac{r^2}{\tau_R} \tag{3.7}$$

where γ is the linear growth rate from the linear stability study, W is the mode width, which can be obtained by balancing the viscosity term with the field line bending term, $< m >$ is the rms poloidal mode number, v_e is the electron thermal velocity, and λ is an enhancement factor over the quasilinear mixing length estimate and the other variables are defined in the Appendix 1. The radial electron thermal transport induced by magnetic field-line stochastization is [104]

$$\tilde{\chi}_e = v_e \sum_{m,n} |(\tilde{b}_r)_{mn}|^2 L_m \tag{3.8}$$

$$= \Lambda^{4/3} (\beta \frac{R_0}{L_p} q^2)^{4/3} \frac{v_e r^2}{R_0} \frac{1}{2^{13/6} < n >^{2/3} S^{2/3} \hat{s}} \tag{3.9}$$

Here, $(\tilde{b}_r)_{mn}$ is the (m, n) Fourier component of the fluctuating radial magnetic field normalized to the toroidal magnetic field B_0, and L_m is the field line correlation length and the other variables are defined in the Appendix 1. Considering the effects of diamagnetic drift stabilization and plasma elongation, the total electron radial thermal transport coefficient is

$$\chi_e^{rb} = (\tilde{\chi}_e + \chi_e^{EB}) f_{dia} f_\kappa \tag{3.10}$$

Here, $f_{dia} = (1 + f_*)^{-1/6}$, where f_* is the electron diamagnetic frequency. A factor of $f_\kappa = \kappa^{-4}$, where κ is the elongation, is included to represent a theoretically expected elongation stabilization calibrated empirically for the entire anomalous transport together [71]. Since no explicit expression was derived for the ion thermal diffusivity, an adjustable fraction of the particle diffusivity was assumed.

3.1.2 Kinetic Ballooning Mode

As discussed in the preceding subsection, the theoretical study of magnetohydrodynamics (MHD) sets an upper β limit for stability in tokamaks. However, experimental results from the ISX-B tokamak did not give clear evidence of a sharp transport-driven β limit caused by ballooning instabilities [105]. Kinetic effects on ballooning instability are included here to account for the possibility of increased transport at higher β. This gives the so-called kinetic ballooning mode. Kinetic instability gives large quasilinear transport fluxes roughly between the first ideal stability limit described above, β_{c1}, and the second stability limit, β_{c2} [41]. For a model of circular equilibrium with small Shafranov shift, the second stability limit is given approximately by $4s/(q^2 R_0)$ [106], where s is the magnetic shear, and R_0 is the major radius. The kinetic ballooning instability was studied using the ballooning representation

$$\phi(\psi, \chi, \zeta) = \sum_{p=-\infty}^{\infty} \overline{\phi}(\psi, \chi - 2\pi p, \zeta) \tag{3.11}$$

to treat high-mode-number perturbations in toroidal systems [107, 108] since these perturbations are characterized by short wavelengths perpendicular to the magnetic field and long parallel wavelengths. The ballooning representation can satisfy the requirements in tokamaks of poloidal periodicity and of small effective parallel wavenumber along the equilibrium magnetic field lines, in the presence of finite magnetic shear, and apply to the various types of drift modes in axisymmetric geometry in the kinetic regime. This representation maps the familiar poloidal angle-like variable onto an infinite domain where periodicity is not required. Using the linearized perturbed distribution function from a reduced gyrokinetic equation, together with the quasi-

neutrality condition and the parallel and perpendicular components of Ampere's law leads to a complicated set of coupled one-dimensional integrodifferential equations. From these equations, the dependence of linear mode growth rate on various parameters can be obtained. The transport fluxes are estimated as [61]

$$\Gamma_a = D\frac{n_a}{L_n}F_\kappa \tag{3.12}$$

$$Q_e = 2.5D\frac{n_eT_e}{L_{T_e}}F_\kappa \tag{3.13}$$

$$Q_i = 2.5D\frac{n_iT_i}{L_{T_i}}F_\kappa \tag{3.14}$$

where [109]

$$D = \omega_e^*\rho_i^2 f_{\beta th}(1+\frac{\beta'}{\beta_{c1}})[(1-\frac{\beta'}{\beta_{c2}}),0]_{max} \tag{3.15}$$

and the remained variables are defined in the Appendix 1.

For short-wavelength instabilities, trapped-electron drift modes are the most significant class of such instabilities at low β [41], while the kinetic ballooning mode appears to be dominant type at higher β [110].

3.1.3 Neoclassical MHD Mode

Neoclassical MHD modes are also called neoclassical pressure-gradient-driven mode [111]. In tokamaks, there exist three neoclassical transport regimes distinguished by collision frequency. These are the banana, plateau and Pfirsch-Schluter regimes. The original treatment of resistive-interchange ballooning instabilities, which have been successful in explaining some experimentally observed anomalous heat transport, were only valid in Pfirsch-Schluter regime, where the collision mean free path is much shorter than the parallel scale length [112]. The neoclassical MHD mode was used to account for anomalous transport in the banana-plateau collision regime by using a group of neoclassical MHD equations, which is valid in the long mean free path regime. This mode typically fills in the gap between the drift wave that dominates in the plasma center, and the resistive ballooning mode, which is localized near the plasma edge [113].

The first of the neoclassical MHD equations is from flux-surface-averaged neoclassical parallel Ohm's law, giving,

$$\begin{aligned} E_{\|} &= \frac{1}{c}\frac{\partial \psi}{\partial t} - \mathbf{b}\cdot\nabla\phi \\ &= \eta_{sp}(1+\frac{mu_e}{\alpha_e \nu_e})J_{\|} + \eta_{sp}\frac{\mu_e}{\alpha_e\nu_e}\frac{c}{B_\theta}\frac{dP}{dr} \end{aligned} \tag{3.16}$$

Here, $E_{\|}$ is the parallel electric field, $\mathbf{b} = \mathbf{B}/|\mathbf{B_0}|$, ψ is the parallel component of the magnetic potential, ϕ is the electrostatic potential, $J_{\|}$ is the parallel current, and η_{sp} is the classical Spitzer resistivity. Assuming $Z_{eff} \sim 1$, $\alpha_e \sim 0.51$ and

$$\mu_e = 2.3\sqrt{\epsilon}\nu_e/(1+1.02\nu_{*e}^{1/2}+1.07\nu_{*e}) \tag{3.17}$$

Here ϵ is the inverse aspect ratio, ν_e is the electron collision rate, and $\nu_{*e} = \nu_e/\epsilon^{3/2}\omega_{be}$, ω_{be} being an electron bounce frequency.

The second of the neoclassical MHD equation is the vorticity evolution equation derived from the charge neutrality condition, ie,

$$\begin{aligned} \frac{d}{dt}(1+\frac{B^2}{B_\theta^2})\nabla_\perp^2\tilde{\phi} &= \frac{B^2}{c^2\rho}\nabla_{\|}\tilde{J}_{\|} + \frac{B}{c\rho}\frac{B}{B_\theta}\frac{d}{dr}\nabla_{\|}\tilde{p} \\ &\quad + \frac{B}{c\rho}\mathbf{b}\times\mathbf{K}\cdot\nabla(2\tilde{P}+\tilde{P}_{\|,h}+\tilde{P}_{\perp,h}) \end{aligned} \tag{3.18}$$

where $\mathbf{K} = \mathbf{b}\cdot\nabla\mathbf{b}$ is the magnetic curvature, the subscript "h" denotes the hot particle component, and $d/dt = \partial/\partial t + (c/B)\mathbf{b}\times\nabla\phi\cdot\nabla$ is the total convective derivative.

The last of the neoclassical MHD equations describes the convective response to $E\times B$ flow;

$$\frac{d\tilde{P}}{dt} \simeq \frac{\partial\tilde{P}}{\partial t} + \frac{c}{B}\mathbf{b}\times\nabla\tilde{\phi}\cdot\nabla P = 0 \tag{3.19}$$

These three equations constitute the basic equations for the study of neoclassical MHD instabilities. In neoclassical transport [31], the parallel viscous drag on the equilibrium poloidal flow carried by the untrapped particles, which is caused by collisions with the immobile toroidally trapped particles, results in a "bootstrap" current. This current will create a modification to the parallel Ohm's law in the long mean free path regime and interacts with viscous damping to drive the instability. Linear instability was studied by employing the ballooning representation to obtain the growth

rate. Nonlinear saturation occurs when the nonlinear energy cascade from linearly unstable, long-wavelength modes to the short-wavelength dissipation range balancing the linear source. This can also be viewed as a radial diffusion balancing the driving forces. From nonlinear saturation conditions, the turbulent pressure diffusivity is determined as an eigenvalue of the renormalized equation. Fluctuation level and radial scales are determined from the pressure diffusivity. The estimated particle transport coefficient from the neoclassical MHD mode is

$$\chi_i = \chi_e = D_a = \frac{\eta q \beta L_s}{2\mu_0 \epsilon L_p} \delta_e \Lambda_N^2 \tag{3.20}$$

where the definition of variables is given in the Appendix 1. The electron heat diffusivity resulting from stochastic magnetic field in saturated neoclassical MHD mode is

$$\tilde{\chi}_e = f_{dia} f_\kappa 0.046 (4\pi)^{2/3} \frac{v_e L_s}{(nS)^{2/3}} (\frac{q\beta R}{L_p})^{4/3} \delta_e^{5/3} \Lambda_N^{7/3} f_\Lambda f_\gamma \tag{3.21}$$

where the definition of variables is given in the Appendix 1. In the stochastic thermal electron transport, the magnetic fluctuations are coupled to electrostatic mode through the parallel Ohm's and Ampere's laws.

3.2 Drift Wave Branch

The drift wave mode is a low frequency microinstability. It is driven in tokamaks by the expansion free energy associated with the radially non-uniform distribution of density and temperature in the plasma. In a low β tokamak plasma, the drift wave instability results from destabilizing electrostatic waves, i.e. drift waves. In a plasma with a magnetic field, ions and electrons will circulate around their guiding centers in opposite directions. The influence of density and temperature gradients causes ion and electron drift in opposite directions. Electrostatic potentials will arise due to charge separation. By the quasi-neutral condition, drift fluxes of electrons and ions are equal. Without destabilizing factors, electrostatic waves will propagate perpendicular to the magnetic field and pressure gradient with the drift speed. The

corresponding wave is called a drift wave. The particles influenced by drift waves will move in an oscillatory manner with a characteristic frequency called the diamagnetic drift frequency defined in the last section. However, when the electrons and ions are driven out of phase by dissipative process, such as collisions and wave-particle resonances, the electron fluxes and ion fluxes will not be equal. Any imbalance between ion and electron fluxes will be compensated by the growth of the drift wave in order to maintain quasineutrality. One type of particle gives energy to wave and makes it grow. The other type of particle will damp the growing of the wave. The resulting unstable modes are the dissipative and collisionless drift instabilities for electrons or ions. In the nominal multi-mode, we use the trapped electron mode (TEM), circulating electron mode (CE) and the ion temperature gradient mode (ITG). The physical mechanism for these will be discussed in the following subsections.

3.2.1 Trapped Electron Mode

The trapped electron instability is driven by free energy from the trapped electrons in tokamaks. In tokamaks, there exists a strong toroidal magnetic field produced by external coils and a weak poloidal field produced by the current in the plasma. The toroidal field is not uniform in radial direction but varies approximately as $B \cong B_0(1 - \epsilon \cos\theta)$, where B_0 is the toroidal field at magnetic axis, ϵ is the inverse aspect ratio, θ is the poloidal angle. This results in a maximum field at the inner edge of torus and weakest field at the outer edge of the torus. All particles gyrate in small circles about a field line and have guiding center flow along the helical field. Since the magnetic field strength is stronger on the inside of the torus than on the outside, some particles with small parallel velocity will be reflected, approximately conserving magnetic moment and kinetic energy. Thus, these particles bounce back and forth and become trapped. The fraction of trapped particles can be roughly estimated as $(r/R)^{0.5}$, where r is the mid-plane halfwidth. Meanwhile, the trapped particles are also subject to the drift arising from the inhomogeneity of the magnetic field. The result of this component of drift is that the elevation projection of the guiding center

orbit has a banana shape. The width of the banana orbit is given by

$$\Delta_b \sim v_D(qR/v_{\|}) \sim (r/R)^{1/2}\rho_p \tag{3.22}$$

where v_D is the drift speed with magnitude $mcv^2/(eB_pR)$, and $\rho_p = mv/(eB_p)$ is the gyroradius in the poloidal field, B_p. The average bounce frequency can be approximated by $\omega_b = \epsilon^{1/2}v_T/(qR)$. Trapped particles can be detrapped by Coulomb collisions. The effective collision frequency ν_{eff} for scattering out of the trapping region is $(R/r)\nu$. In the case of $\nu_{eff} \ll \omega_{be}$ and $\omega \gg \omega_{bi}$, trapping has an important driving effect on instability for elections but not for ions. Magnetic trapping constrains the motion of some electrons along the magnetic field and prevents them from reaching a state of thermal equilibrium. This results in an imbalance of ions and electron flux, which excites the electrostatic drift wave. For different collisional frequencies, electrostatic waves can be driven by inverse Landau damping mechanism or by collisional dissipation of trapped electrons. The corresponding mode is called the collisionless trapped mode or dissipative trapped election mode. Generally, it is believed that the collisionless trapped mode can dominate the anomalous transport near the plasma core in tokamaks, where the collision rate is low, and the trapped collisional electron mode and ion temperature gradient mode can dominate the region between the plasma edge and the central region [114].

The trapped electron instability was studied using Boltzman-Valsov equation

$$\frac{\partial f}{\partial t} + \mathbf{v}\cdot\nabla f + \frac{q}{m}(-\nabla\phi + \mathbf{v}\times\mathbf{B})\nabla_{\mathbf{v}} f = C(f,f) \tag{3.23}$$

where f is the electron distribution function, ϕ is the potential and $C(f,f)$ is the collision operator. For the plasma near the thermal equilibrium, the distribution function is written as

$$f = f_0 + \tilde{f} \tag{3.24}$$

where f_0 is the unperturbed Maxewillian distribution at potential ϕ, and the $\tilde{f}$ is the perturbed distribution function. Substituting this ansatz for the distribution function into equation (3.23) gives the linearized Boltzman-Valsov equation for the perturbed distribution function $\tilde{f}$, which is generally solved for using an approximated collision

operator [35, 36, 37, 115]. From the distribution function, the perturbed electron density is determined by integrating distribution function in velocity space. Using the quasi-neutrality condition yields the dispersion relation for the trapped electron mode, from which the linear growth rate is obtained. The particle and thermal diffusivities are estimated from a quasilinear approximation, and the mixing length rules and are modified to account for finite β effects [56, 61]. The resulting nominal diffusivities,

$$D_a = (1 - \frac{f_{ith}}{1.0 + \nu_e^*}) D_{TEM} F_\beta \tag{3.25}$$

$$\chi_e = (1.0 - 0.6 f_{ith}) D_{TEM} F_\beta \tag{3.26}$$

$$\chi_i = D_{TEM} F_\beta \tag{3.27}$$

where D_{TEM} are

$$D_{TEM} = \epsilon^{1/2} \frac{\omega_e^*}{k_\perp^2} f_{coll} \tag{3.28}$$

The definitions of F_β, ω_e^*, $k_\perp$ and f_{coll} are given in Appendix 1.

3.2.2 Circulating Electron Mode

The circulating electron instability is a type of microinstability arising from the untrapped electrons in tokamak. In a non-uniform magnetic field, some electrons with small parallel velocity are trapped in the banana region to form the source of trapped electron instability discussed above. The other particles with large parallel velocity can move around the torus. These latter electrons are called circulating electrons. Driven by the pressure gradient, the circulating electron can drift across the magnetic field. If $\omega_e > kv_e$, the mode is primarily destabilized by electron-Coulomb-type collisions. The resulting mode is called the collisional circulating drift mode. If $\omega_e < kv_e$, the principal destabilizing process for drift waves is inverse electron-Landau damping. This mode is called the collisionless ("universal") circulating electron mode [37].

The circulating electron mode was studied using a method similar to that for the trapped electron mode [116]. The growth rate is obtained from the perturbed distribution function and quasi-neutrality condition. The estimated transport coefficients are [56, 61]

$$\chi_e = \chi_i = D_a = F_\kappa F_\tau \frac{\nu_{ei}\omega_e^*}{\omega_{te}^2}(1 + c_{80} f_{ith}\eta_e \epsilon_n)\frac{\omega_e^*}{k_\perp^2} \tag{3.29}$$

Here the definitions of variables are given in Appendix 1.

3.2.3 Ion Temperature Gradient Mode

The ion temperature gradient mode is a type of low frequency electrostatic drift wave mode driven by the ion temperature gradient. It is also known as the mixing mode or η_i mode, and propagates in the ion diamagnetic direction. It involves a coupling of ion sound waves with ion diamagnetic drift waves. Even without a radial pressure gradient, when non-negligible motion of ions along the magnetic field causes plasma compression, which produces a perturbed ion pressure and an ambipolar electric field to maintain quasi-neutrality. The effect of the electrical field and the ion pressure perturbation is to oppose the compression, and the resulting oscillation is an ion sound wave. In the presence of a perpendicular pressure gradient, the perturbed ion pressure changes due to the $E \times B$ diamagnetic drift. That is, the convection of ions across the field induces an additional perturbation of the ion pressure. When the ion sound wave propagates in the ion diamagnetic drift direction, the sufficiently large pressure gradient, (which is larger than the parallel compression so that the convective perturbation of the ion pressure could overcome the compressional perturbation and the ambipolar electric field), generates a "negative compressibility," and the wave is amplified. Thus, instability arises. The source of the instability is the ion temperature gradient contribution to the pressure gradient, since the convection associated with the presence of the density gradient always leads to a positive contribution to the positive compressibility. A finite ion temperature gradient destabilize modes rotating in the ion diamagnetic drift direction. The critical gradient can be expressed in terms of the ratio $\eta_i = L_n/L_{T_i}$, where $L_n = -n_i/\nabla n_i$ and $L_{T_i} = -T_i/\nabla T_i$.

For a simple fluid with the ratio of specific heat $\gamma = 5/3$, the required η_i is $> 2/3$. The turbulence evolving from the ion temperature gradient modes saturates through ion pressure "mixing"[38], i.e. $\tilde{p}/p_i \simeq \tilde{T}_i/T_i + \tilde{n}/n \sim (k_r L_{p_i})^{-1} > \delta n/n$, where k_r is the radial wave vector and $L_{p_i} = -(d \ln p_i/dr)^{-1}$ is the ion pressure scale length. The transport saturation level is estimated from the quasi-linear theory or nonlinear calculations [117, 118, 119, 120].

The ion temperature gradient mode has been studied using kinetic theory and fluid models [121, 122, 123, 124, 125]. In the collisionless limit, when the temperature gradient is steep enough, that is when $\eta_i \geq 1$, the instability can be driven by inverse ion Landau damping [126]. Kinetic theory is used to study the turbulence. In the collisional limit, a fluid model can be used. The following gives a consideration of a fluid approximation for the ions, with the electrons taken to be adiabatic in the plane slab [127].

The ions are governed by the equations of continuity, parallel momentum balance, and adiabatic compression:

$$(\omega_0 + \omega_*)\frac{e\tilde{\phi}}{T_e} = k_z \tilde{u}_i \tag{3.30}$$

$$(\omega_0 + \frac{6}{5} i\gamma) k_{\|} \tilde{u}_i = \frac{T_i k_{\|}^2}{m_i}(\frac{e\tilde{\phi}}{T_i} + \frac{\tilde{p}}{p_0}) \tag{3.31}$$

$$\frac{3}{2}\omega_0 \frac{\tilde{p}}{p_0} + \frac{3}{2}\omega_*(1+\eta_i)\frac{e\tilde{\phi}}{T_e} - \frac{5}{2} k_{\|}\tilde{u}_i = 2i\gamma(\frac{e\tilde{\phi}}{T_e} - \frac{\tilde{p}}{p_0}) \tag{3.32}$$

where

$$\omega_0 = \omega - k_\perp (\partial p_0/\partial x)(m_i \Omega_i)^{-1} \tag{3.33}$$

$$\omega_* = cT_e k_\perp/(eBL_n) \tag{3.34}$$

$$\gamma = \nu_{ii} k_\perp^2 T_i/(m_i \Omega_i^2) \tag{3.35}$$

and ω is the electrostatic wave frequency, ν_{ii} is the ion-ion collision frequency, Ω_i is ion gyro-frequency, and $\tilde{p}_i$, $\tilde{u}_i$, $\tilde{\phi}$ are the perturbed ion pressure, velocity along the magnetic field and potential. From the above three equations, using the quasi-neutrality condition, a dispersion relation for electrostatic waves is obtained. The linear growth rate of the ion temperature gradient mode is derived from the dispersion equation.

The idealized fluid picture must be modified to account for realistic tokamak conditions and geometry. In toroidal geometry, the ion temperature gradient mode is driven predominantly by ion curvature drifts [128]. The transport coefficients are estimated in a quasi-linear approximation following the work of Dominguez and Waltz [56], including the finite β effects [61], as

$$\chi_i = f_{ith} f_\kappa^t f_\tau f_\beta (2\eta_i \epsilon/\tau)^{1/2} \frac{\omega_e^*}{k_\perp^2} \tag{3.36}$$

where the definitions of variables are given in Appendix 1.

Chapter 4

Numerical Method of Solving the Transport Equation

The theoretical transport equation described in the last chapter is a group of nonlinear parabolic equations which can only be solved numerically. Many methods, including finite difference, finite element, Monte Carlo and nodal methods, have been applied to the solution of transport equations [129, 130, 131, 132]. Among them, finite difference method provides an efficient and reliable numerical solution to the transport equation and is widely used in the plasma transport simulation community [133, 134, 135, 136, 137]. In this chapter, we will give an introduction of the finite difference method solution of differential equation in Section 1, the numerical algorithm used to solve the transport equations in the transport code BALDUR [138] is described in Section 2, and numerical solution of a simplified transport equation is illustrated in Section 3.

4.1 Finite Difference Method

The finite difference method is based upon the discretization of continuous domain into finite discrete points. The derivatives of functions in the governing differential equation are approximated by finite difference value among "stencil points." The continuous differential equation is replaced by a recursive finite difference equa-

tion. Consider a first-order system of ordinary differential equation which has the general form

$$\frac{\partial u}{\partial t} = F(t, u) \tag{4.1}$$

where t is the independent variable, u is a vector valued function of t, and $F(t, u)$ is a vector equation function. Discretizing the domain in t into n points, the derivative $\partial u/\partial t$ at point $i, 1 \leq i \leq n$, can be approximated as

$$(\frac{\partial u}{\partial t})_i = \frac{u(t_{i+1}) - u(t_i)}{\delta t} \tag{4.2}$$

using the Taylor series expansion. This turns the differential equation (4.1) into a difference equation

$$\frac{u(t_{i+1}) - u(t_i)}{\delta t} = F_i(t_i, u(t_i)) \tag{4.3}$$

where $\delta t = t_{i+1} - t_i$, and $F_i(t_i, u(t_i))$ is the vector equation function value calculated at the point i. The approximation for the derivative used here is called the Euler's forward method. The equation (4.3) can be rewritten as

$$u(t_{i+1}) = u(t_i) + \delta t \; F_i(t_i, u(t_i)) \tag{4.4}$$

We see that the value of the function u from the approximate solution at the step t_{i+1} is determined by explicit formulas involving solution values only at the previous time. Such a method is called an explicit method. The explicit method is intuitively attractive due to the simplicity of the recursive expression. But this method is numerically unfavorable, as numerical instability will restrict the explicit method to an impractically small time step size or otherwise causes the artificial numerical instability. Here, numerical instability means that numerical approximation error will keep on increasing through successive time steps, and the numerical solution loses its precision. This difficulty can be overcome by using an alternative approximation for the derivative, that is,

$$(\frac{\partial u}{\partial t})_i = \frac{u(t_i) - u(t_{i-1})}{\delta t} \tag{4.5}$$

This approximation has the same accuracy as the first approximation and is called the backward Euler method. Now the difference equation becomes

$$u(t_{i+1}) = u(t_i) + \delta t \; F_{i+1}(t_{i+1}, u(t_{i+1})) \tag{4.6}$$

The value of $u(t_{i+1})$ at the step t_{i+1} can not be directly obtained from the value at previous time step since the value of function F_{i+1} is not known before we know the value of $u(t_{i+1})$. Equation (4.6) constitutes a group of algebraic equations to be solved for $u(t_{i+1})$. The complexity of these equations depends on the form of the function $F(t,u)$. If $F(t,u)$ is a linear function of u, a linear equation solver is enough; if $F(t,u)$ is a non-linear function of u, a nonlinear equation solver has to be used, which generally requires an iterative procedure. This numerical method solving the differential equation is called an implicit method because we must evaluate $F(t,u)$ with argument u_{i+1} before we know its value. This method is more computationally complex and more expensive per time step, but it has a larger range of time steps which allow numerical stability [139].

In the forward and backward Euler methods described above, only information at one previous step is used to evaluate the value at the next time step. This gives a lower accuracy with only the first order approximation precision of δt. To obtain higher order accuracy, the information at more than one previous step is used to estimate the solution at the next point. Such method is called the multi-step method. A linear multi-step method has the form

$$u_{i+1} = \sum_{k=1}^{n} \alpha_k u_{i+1-k} + h \sum_{k=0}^{n} \beta_k F(t_{i+1-k}, u_{i+1-k}) \tag{4.7}$$

the parameters α_i and β_i are determined by polynomial interpolation [140]. If $\beta_0 = 0$, the method is explicit, while if $\beta_0 \neq 0$, the method is implicit. The implicit method is usually more accurate and stable, but requires a starting guess for the solution of nonlinear algebraic equation. This is most conveniently supplied by an explicit formulae, so the two are used as a predictor-corrector pair. One could use the correction repeatedly until some convergence tolerance is met, but it may not be worth the expense. So a fixed number of corrector steps, often only one, may be used instead, giving a prediction-evaluation-correction-evaluation (PECE) scheme. Although it has no effect on the value of $u(t_{i+1})$, the second evaluation of u in a PECE scheme yields an improved value of $u'(t_{i+1})$ for the use of next step.

The above discussions was limited to the ordinary differential equations. Similar concepts can be applied to the parabolic partial differential equation, with

the both temporal and spatial variables being discretized.

4.2 Numerical Algorithm

For the transport model studied in this work, above implicit method with predictor-corrector algorithm has been employed to solve the group of transport equations.

The transport equation solved in the BALDUR has the form

$$\frac{\partial y}{\partial t} = \frac{1}{r}\frac{\partial}{\partial r} r(A'\frac{\partial y}{\partial r} + B'y) + Cy + D \tag{4.8}$$

where y is a vector of dependent variables, e.g. density n_i, temperature T_i, T_e etc, and A', B' and C are matrices of nonlinear coefficients, and D is a source vector. This equation is discretized using the Crank-Niclson method as

$$\frac{y^{i+1} - y^i}{\delta t} = \theta_{CN} G(y^{i+1}) + (1 - \theta_{CN}) G(y^i) \tag{4.9}$$

where y^{i+1} is the value of variables at the new time t^{i+1}, y^i is the value of variables at the old time t^i, G is the difference form of the right hand side of equation (4.8), and θ_{CN} is a factor controlling the degree of implicitness. For $\theta_{CN} = 0$, above scheme reduces to the explicit forward Euler's method. For $\theta_{CN} = 1$, this method is the backward implicit Euler method. The value of θ_{CN} has traditionally been set between one half and one to guarantee the unconditional stability of numerical equation. Putting equation (4.9) into equation (4.8) and taking the discretization of space, equation (4.8) can be rewritten as

$$A(y)y_{j+1}^{i+1} + B(y)y_j^{i+1} + C(y)y_{j-1}^{i+1} + D(y) = 0 \tag{4.10}$$

where subscript j specifies the spatial discrete point. Above equation is a nonlinear implicit algebraic equation. Above equation is solved using a two-step predictor-corrector scheme. First, a trial solution y_0^{i+1} is computed as predictor with the A, B, C, D evaluated at the old time step t_i. Next, a linear combination $y^{i+\theta_p} = (1 - \theta_p)y^i + \theta_p y_0^{i+1}$ is computed as a corrector, where θ_p is a parameter between zero

and one. The final solution y^{i+1} is computed using the θ_p time centered A, B, C, D using $y^{i+\theta_p}$ rather than y^i. Then y^{i+1} is stored for use in the next time step. The typical problem are run with θ_{CN} equal to one to make the problem as stable as possible.

From above analysis, we see that θ_{CN} acts as an implicit control variable. Its value will affect the numerical stability of numerical solution. In convention, $\theta_{CN} = 1$ is called the full implicit method. Bateman suggested that a better stability could be obtained with $\theta_{CN} = 4$ rather than one based on the study of a simplified temperature diffusion equation [60]. This is due to the discontinuous change of transport coefficients in the flux formulae in the η_i mode. In the next section, we will illustrate the above numerical algorithm and study the effects of θ_{CN} by solving a simplified transport equation numerically with the flux switch discussed in Bateman's paper.

4.3 Solving a Simplified Transport Equation

The simplified transport equation is examined here

$$\frac{\partial T}{\partial t} = \frac{\partial}{\partial x}(\chi \frac{\partial T}{\partial x}) \tag{4.11}$$

where the diffusivity χ has a sharp turn-on as a function of $(\partial T/\partial x)$

$$\chi = \chi_0 + \chi_1 \quad \text{for } -\tfrac{\partial T}{\partial x} \geq c_0 \tag{4.12}$$

$$\chi = \chi_0 \quad \text{otherwise} \tag{4.13}$$

The boundary conditions are

$$T = T_0 \quad x = 0 \tag{4.14}$$

$$T = T_c \quad x = a \tag{4.15}$$

and the initial condition is

$$T(x) = (T_0 - T_c)(1 - (x/a)^2) + T_c \tag{4.16}$$

This equation is nondimensionlized using the time scale τ, spatial scale a and temperature scale T_0. The χ_0 and χ_1 are assumed to be a^2/τ, c_0 to be T_0/a, and the

T_c is set as $0.01T_0$. Applying the implicit Crank-Niclson finite difference scheme, we obtain

$$-\theta_{CN}k\chi_{j+1}^{i+1}T_{j+1}^{i+1} + (\theta_{CN}k\chi_{j+1}^{i+1} + \theta_{CN}k\chi_j^{i+1} + 1)T_j^{i+1} - \theta_{CN}k\chi_j^{i+1}T_{j-1}^{i+1} =$$
$$(1-\theta_{CN})k\chi_{j+1}^{i}T_{j+1}^{i} - ((1-\theta_{CN})k\chi_{j+1}^{i} + (1-\theta_{CN})k\chi_j^{i} - 1)T_j^{i} + (1-\theta_{CN})k\chi_j^{i}T_{j-1}^{i} \quad (4.17)$$

where $k = \delta t/(\delta x)^2$, and χ_j^i is the diffusivity at time step i at spatial point j, which is obtained using a centered difference approximation scheme of the derivative of temperature T, ie,

$$\chi_j = \chi_0 + \chi_1 \qquad \text{for } \frac{T_{j-1}-T_{j+1}}{2\delta x} \geq c_0 \quad (4.18)$$

$$\chi_j = \chi_0 \qquad \text{otherwise} \quad (4.19)$$

A two-step predictor-corrector scheme is employed to solve above implicit equation following the procedure described in the last section. The dimensionless temperature profile at $t = 10.0$ is shown in Figs 4.1-3 with the implicit parameter $\theta_{CN} = 0.0, 0.5, 0.7, 1.0, 2.0$ and 4.0, $\theta_p = 0.5$ $\delta t = 0.01$ and $\delta x = 0.02$. Numerical instabilities are observed in Fig 4.1 for $\theta_{CN} = 0.0$, and 0.5. The $\theta_{CN} = 0.5$ is the marginal stable condition in the linear diffusion equation. For the nonlinear diffusion equation, the marginal stable point is not stable any more. In the Figs 4.2-3, we see that, for $\theta_{CN} = 0.7$, the solution tends to be stable but with small ripple. For $\theta_{CN} = 1.0, 2.0$ and 4.0, This is no practical difference for our purposes in the quality of solution for these values of θ_{CN}. Fig 4.4 gives the dimensionless temperature at $t = 10.0$ for a smaller spatial step size with $\theta_{CN} = 0.7$. We can see that the profile is smoother for smaller spatial step size. These results suggest that the larger value of θ_{CN}, e.g. 4.0, may not be necessary for the better numerical stability of above simplified transport equation solution. On the other hand, it appears that the smaller spatial step size will improve the quality of numerical solution.

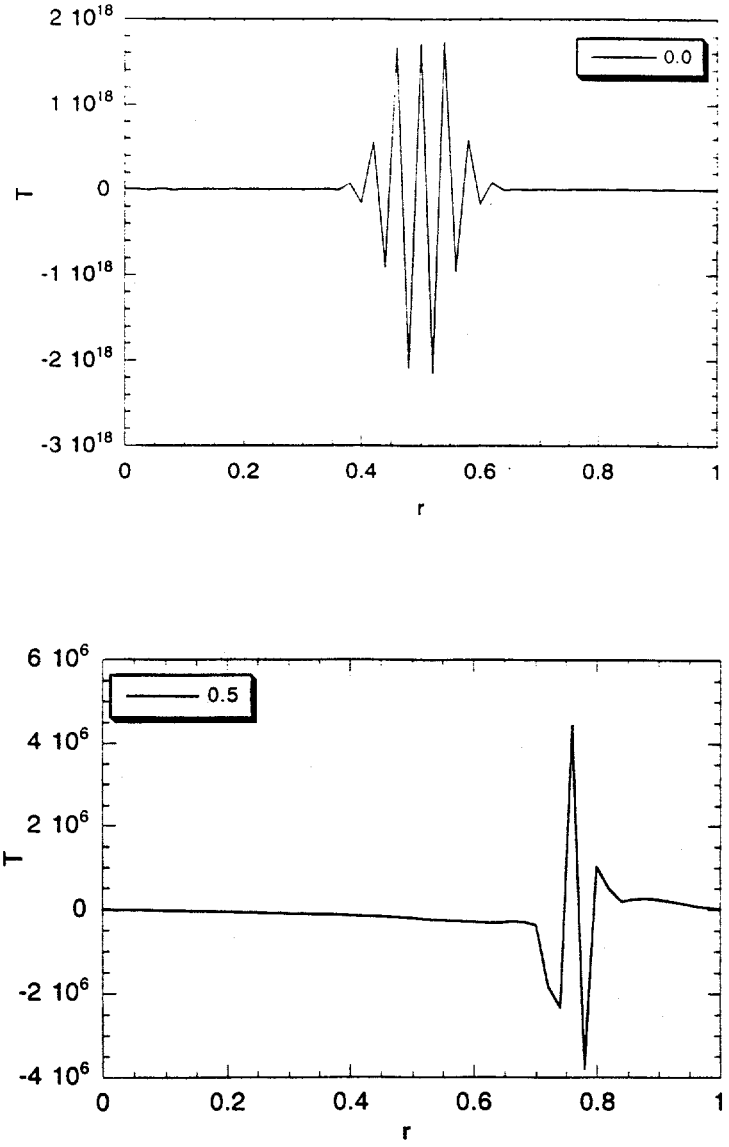

Fig. 4.1: Dimensionless temperature profiles at $t = 10$ for $dt = 0.01$, $dx = 0.02$, $\theta_{CN} = 0$ and 0.5.

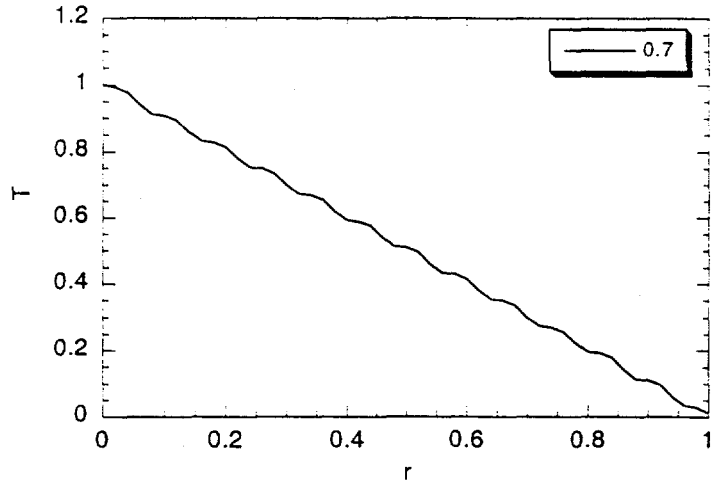

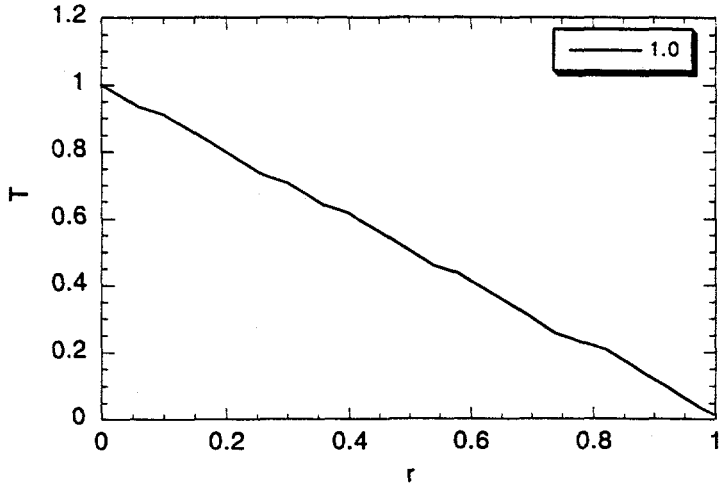

Fig. 4.2: Dimensionless temperature profiles at $t = 10$ for $dt = 0.01$, $dx = 0.02$, $\theta_{CN} = 0.7$ and 1.0.

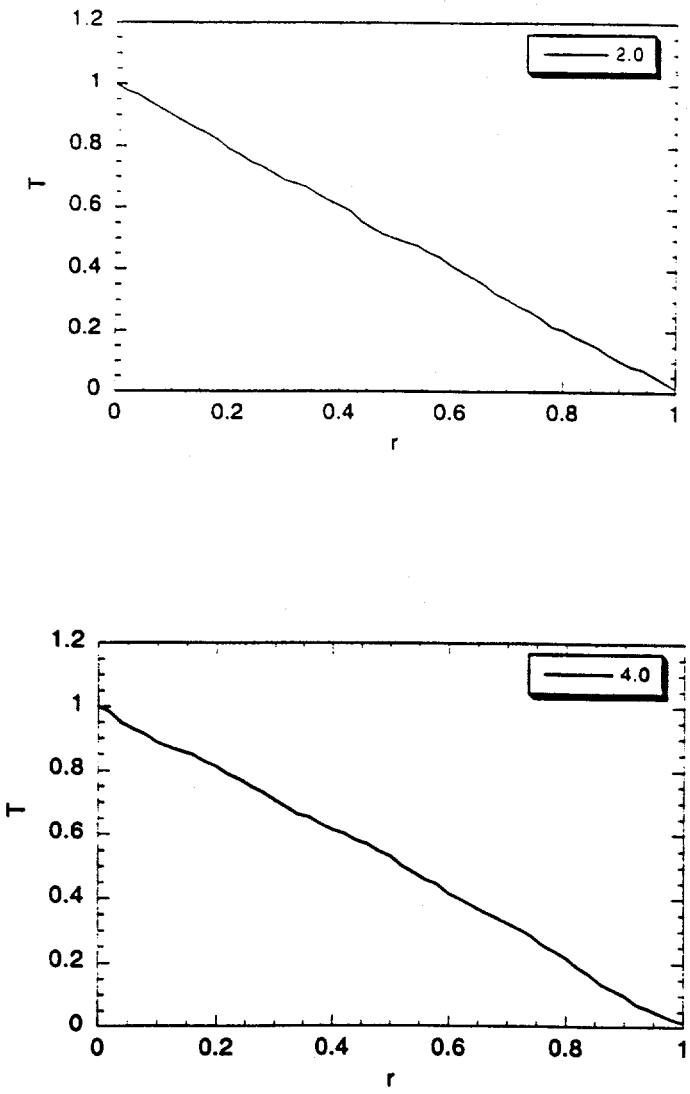

Fig. 4.3: Dimensionless temperature profiles at $t = 10$ for $dt = 0.01$, $dx = 0.02$, $\theta_{CN} = 2.0$ and 4.0.

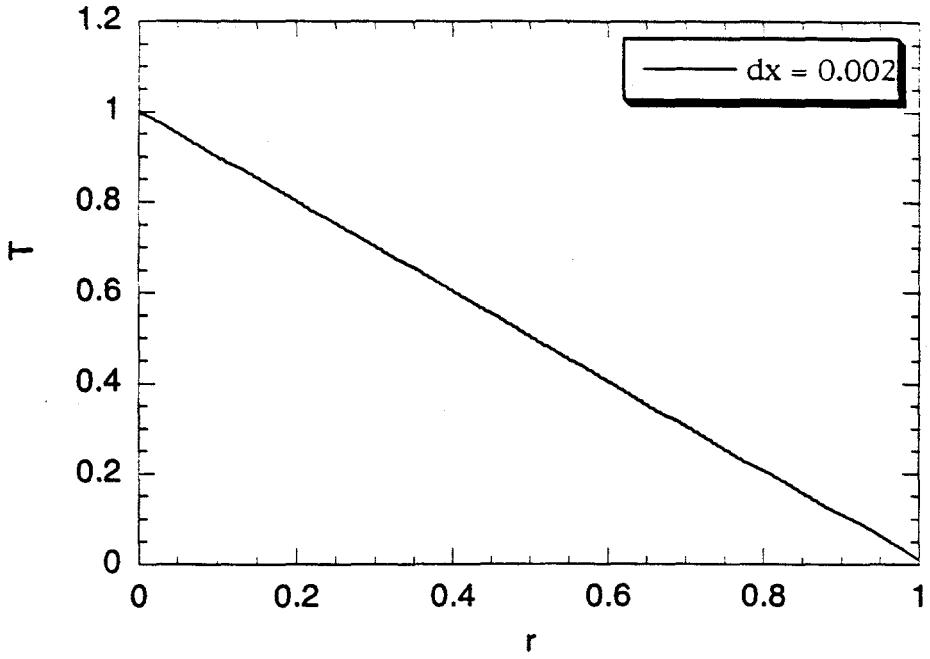

Fig. 4.4: Dimensionless temperature profiles at $t = 10$ for $dt = 0.01$, $dx = 0.002$, $\theta_{CN} = 0.7$.

Chapter 5

Methods of Parameter Estimation

Parameter estimation is an important part of a mathematical modeling procedure. It provides an important way to fill the gap between pure theoretical expressions and experimental observations. The problem of estimating parameters from observational data can trace back to about 300 B. C., when the Babylonian astronomers inferred the planetary motion parameters from the measurement data. Many great mathematicians have made contributions to the theory of parameter estimation. Daniel Bernouli developed an estimation procedure which is referred to as the maximum likelihood method in the present literature. Leonhard Euler commented on Bernouli's method and attempted to offer another principle [141]. Thomas Bayes introduced the concept of posterior distribution in his posthumous publication of "An Essay Towards Solving a Problem in the Doctrine of Chances" [142]. This concept provides a unifying framework for most of the basic approaches to estimation theory. Legendre published the first account of the method of least-squares in 1806 in his book *Nouvelles Methods pour La Determination des Cometes.* Gauss studied this method independently in 1809 for use on the astronomical observations [143]. He considered the problem from a probabilistic point of view and attempted to define the best estimate as the most probable value of the parameters. He assumed that the mean value had a uniform distribution and argued that the measurement errors were independent and had a normal distribution with a mean zero and constant variance σ^2. Laplace restudied least-squares between 1812 and 1820, and put this

method on a sound theoretical basis [144]. In 1925, Fisher introduced the concepts of sufficient statistics, efficient and consistent estimates to evaluate the estimators and investigated the maximum likelihood method in the framework provided by these ideas [145].

In this chapter, we will give an introduction to least-squares estimation in Section 1, maximum likelihood estimation in Section 2 and maximum a posteriori estimation closely related to the work in the rest of the present thesis in Section 3, numerical methods for optimization in Section 4, and summary in Section 5.

5.1 Least-Squares Estimation

Least-squares estimation is the most commonly used method because of its simplicity. This method minimizes the summation of the squares of a set of deviations between the theoretical model output and experimental data with respect to the uncertain parameters in the theoretical model. Suppose that there are m parameters $(\theta_1, \theta_2, \cdots, \theta_m)$ in the theoretical model and n measurements $(y_1, y_2, \cdots, y_n)$, these uncertain parameters of model are related to the measurement data according to

$$y_i = f_i(\theta_1, \theta_2, \cdots, \theta_m) + v_i \qquad \text{for } 1 \leq i \leq n \tag{5.1}$$

where y_i is the ith measurement, f_i is the theoretical model response corresponding to the ith measurement and v_i is the deviation between measurement and model results. The least-squares estimator of Θ is defined as a value Θ_{LS} to minimize

$$l_{LS} = (Y - F(\Theta))^T (Y - F(\Theta)) \tag{5.2}$$

where $Y = y_1, y_2, \cdots, y_n$ stands for the measurement vector, $\Theta = \theta_1, \theta_2, \cdots, \theta_m$ the parameter vector, $F = f_1, f_2, \cdots, f_m$ for the model output vector, and superscript T for the transpose of vector.

The model response function F could be a linear or nonlinear function of the parameter vector Θ. In a linear system, the model function F is a linear function of Θ and the l_{LS} can be represented in matrix form as

$$l_{LS} = (Y - H\Theta)^T (Y - H\Theta) \tag{5.3}$$

where H is model response matrix. Sufficient conditions that Θ minimizes l_{LS} are that

$$\frac{\partial l_{LS}}{\partial \theta_i} = 0 \qquad \text{for } 1 \leq i \leq m \tag{5.4}$$

and that the Hessian matrix $\partial^2 l_{LS}/\partial\theta_i\partial\theta_j, 1 \leq i \leq m, 1 \leq j \leq m$ is positive definite. It follows from equation (5.2) that we obtain

$$H^T H\Theta = H^T Y \tag{5.5}$$

Note that the Hessian matrix of l_{LS} is

$$He = 2H^T H \tag{5.6}$$

This matrix is positive-definite as long as H has maximum rank.Then the solution of equation (5.5) is unique and minimize l_{LS}. This equation is also referred to as the normal equation. Since H has been assumed to have maximum rank, the inverse of $(H^T H)$ exists and the least-squares estimator is found to be

$$\Theta_{LS} = (H^T H)^{-1} H^T Y \tag{5.7}$$

here Θ_{LS} is a linear function of the data Y.

So far, the least-squares estimation is shown as a deterministic approach to the parameter estimation problem. Its justifications are generally based on the probabilistic arguments concerning the measurement error v_i. In the least-squares estimation, v_i is assumed to be normally distributed with zero mean and constant variance σ^2. The error in the estimator Θ_{LS} is a linear function of the measurement errors V, since

$$\tilde{\Theta}_{LS} = \Theta - \Theta_{LS} = \Theta - (H^T H)^{-1} H^T (H\Theta + V) = -(H^T H)^{-1} H^T V \tag{5.8}$$

The mean value of $\tilde{\Theta}_{LS}$ is

$$E(\tilde{\Theta}_{LS}) = E(\Theta - \Theta_{LS}) = -(H^T H)^{-1} H^T E(V) \tag{5.9}$$

From above assumption of V, we have

$$E(\tilde{\Theta}_{LS}) = 0 \tag{5.10}$$

This shows that least-squares estimator is an unbiased estimator. The covariance of the error in the estimator is given by

$$E(\tilde{\Theta}_{LS}\tilde{\Theta}_{LS}^T) = P = \sigma^2(H^T H)^{-1} \tag{5.11}$$

It should be noted that error covariance matrix P does not depend on the measurements Y. This suggests that the performance of the estimator can be evaluated before receiving any measurement data [98].

Although the linear least-squares estimator can be obtained directly from equation (5.7), it is rarely done in this way due to the computational inefficiency in the direct calculation of the inverse of a matrix. Instead, normal equation (5.5) is solved using Cholesky factorization by setting

$$H^T H = LL^T \tag{5.12}$$

where L is a lower triangular matrix. The substitution of this relation into the normal equation yields

$$LL^T\Theta = H^T Y \tag{5.13}$$

Letting $L^T\Theta = Z$, we have

$$LZ = H^T Y \tag{5.14}$$

This equation can be solved by forward substitution. Then $L^T\Theta = Z$ is solved by backward substitution.

Cholesky factorization provides an useful way to solve linear least-squares problem, but it also has shortcomings. Information can be lost in forming the normal equation matrix and the right hand side vector when elements in matrix H are very small. One alternative method is to use orthogonal transformation such that the equation $H\Theta = Y$ is reduced into

$$\begin{bmatrix} R \\ 0 \end{bmatrix} \Theta = \begin{bmatrix} Y_1 \\ Y_2 \end{bmatrix} \tag{5.15}$$

where R is a $m \times m$ square upper triangular matrix [147]. This equation is further simplified as

$$R\Theta = Y_1 \tag{5.16}$$

which can be solved by backward substitution.

The solution method required for nonlinear least-squares problem is more involved. This generally requires a numerical search for the minimum point of equation 5.2. Relevant numerical methods will be discussed in section 4.

5.2 Maximum Likelihood Estimation

In the least-squares method, the measurement y_i is assumed as normally distributed with mean f_i and constant variance σ^2. In the more general situation where this simple assumption does not apply, the probability density distribution function of Y with given parameter Θ is $l(Y/\Theta)$. This function is called the likelihood function. It is reasonable to choose an estimator of Θ such that value Θ_{ML} will maximize $l(Y/\Theta)$. This estimator can be interpreted as providing the value of Θ that makes the measurement most likely. The estimator Θ_{ML} is called the maximum likelihood estimator. To obtain the maximum likelihood estimator, we can use a multi-dimensional search in Θ space to maximize the likelihood function or solve a group nonlinear algebraic equations from a necessary condition for the estimator. The necessary condition that Θ maximizes the likelihood function is

$$\frac{\partial l(Y/\Theta)}{\partial \theta_i} = 0 \qquad \text{for } 1 \leq i \leq m \tag{5.17}$$

Because of the exponential character of many probability density functions, e.g. normal distributions, it is convenient to treat the log likelihood function and rewrite equation 5.17 (equivalently for nonzero l) as

$$\frac{\partial \ln l(Y/\Theta)}{\partial \theta_i} = 0 \qquad \text{for } 1 \leq i \leq m \tag{5.18}$$

This equation is also called likelihood equation.

The maximum likelihood estimator is intuitively appealing. It has a number of attractive properties in the limit of large number of samples [146]. The probability distribution of the estimator is asymptotically normal with mean Θ and covariance matrix $(mJ)^{-1}$, where J is the Fisher information matrix, which is defined as

$$J_{ij} = -E\left(\frac{\partial^2 \ln l(Y/\Theta)}{\partial \theta_i \partial \theta_j}\right) \qquad \text{for } 1 \leq i,j \leq m \tag{5.19}$$

5.3 Maximum a Posteriori Estimation

The maximum likelihood estimator is based on the probability density function $l(Y/\Theta)$ and does not utilize any a priori information about the parameter Θ. The Θ is treated as an unknown but nonrandom parameter. Bayes' rule provides a mechanism for allowing us to include a priori probabilistic information about Θ. Maximum a posteriori estimation is based on Bayes' conditional probability theorem. Bayes theorem states that the a posteriori density function $p(\Theta/Y)$ is related to a priori density function $p(\Theta)$ according to

$$p(\Theta/Y) = l(Y/\Theta)[p(\Theta)/p(Y)] \tag{5.20}$$

In this equation, the likelihood function $l(Y/\Theta)$ is multiplied by the a priori information $p(\Theta)$ and the normalization $p(Y)$. A maximum a posteriori estimator is chosen to maximize the a posteriori density function given the measurement Y. This estimator can be obtained using the direct numerical search algorithm discussed below in section 4 or by solving a group of algebraic equations from the necessary condition for the estimator. The necessary condition that Θ maximizes the a posteriori density function is

$$\frac{\partial p(\Theta/Y)}{\partial \theta_i} = 0 \qquad \text{for } 1 \leq i \leq m \tag{5.21}$$

Again, it is often more convenient to maximize a log a posteriori density function and rewrite this equation as

$$\frac{\partial \ln l(Y/\Theta)}{\partial \theta_i} + \frac{\partial \ln p(\Theta)}{\partial \theta_i} = 0 \qquad \text{for } 1 \leq i \leq m \tag{5.22}$$

The first term in this equation is the same as the term in the likelihood function. The second term represents the effect from the prior information about the parameters. If the prior density distribution is uniform over the range of values of Θ for which $p(Y/\Theta)$ is significantly greater than zero, then to a good approximation, equation (5.22) will be

$$\frac{\partial \ln l(Y/\Theta)}{\partial \theta_i} = 0 \qquad \text{for } 1 \leq i \leq m \tag{5.23}$$

which is just the likelihood equation (5.18). In this case, maximizing the a posteriori density function $p(\Theta/Y)$ is reduced into maximizing the likelihood function $l(Y/\Theta)$,

which is the maximum likelihood estimation. This case arises when there is no a priori information about Θ available. Such a prior density function of Θ is called an uninformative prior distribution. The a priori density function $p(\Theta)$ must be established by some "estimation" procedure. Such estimation may come from the previous experience and/or theoretical considerations. Suppose, for example, that a sequence of data $y_1, y_2, \cdots, y_n$ is available. Let Y^n denote the complete data vector and note that

$$p(\Theta/Y^n) = p(\Theta/y_1, y_2, \cdots, y_n) = l(Y^n/\Theta)p(\Theta)/p(Y^n) \tag{5.24}$$

From Bayes' rule , this equation can be rewritten as

$$p(\Theta/Y^n) = p(y_n/Y^{n-1}, \Theta)p(Y^{n-1}/\Theta)p(\Theta)/p(Y^n) \tag{5.25}$$

Assuming that the measurements are independent, given Θ,

$$p(y_n/Y^{n-1}, \Theta) = p(y_n/\Theta) \tag{5.26}$$

equation (5.20) reduces into

$$p(\Theta/Y^n) = p(y_n/\Theta)[p(\Theta/Y^{n-1})/p(y_n/Y^{n-1})] \tag{5.27}$$

where

$$p(y_n/Y^{n-1}) = \int p(y_n, \Theta/Y^{n-1})d\Theta = \int p(y_n/\Theta)p(\Theta/Y^{n-1})d\Theta \tag{5.28}$$

comparing with the equation (5.24), we see that the previous measurement information $p(\Theta/Y^{n-1})/p(y_n/Y^{n-1})$ severs as a priori information relative to the measurement y_n.

From a statistical point of view, the a posteriori density function $p(\Theta/Y)$ contains all the information about random parameters Θ that the measurement Y provides. The maximum a posteriori estimation differs from the maximum likelihood estimation when a priori information concerning Θ is available. In the limit of a large number of measurements, the prior information has negligible effect and the maximum a posteriori estimator tends to the maximum likelihood estimator. When

a priori information is not available, the maximum a posterior estimator is just the maximum likelihood estimator. Moreover, in the discussion of least-squares estimation, we assume the uniform distribution of Θ and the measurements Y have a normal distribution and constant variance. This gives us the a posteriori density function of Θ given the measurements Y

$$p(\Theta/Y) = \frac{1}{\sqrt{(2\pi\sigma^2)^m}} \exp\{-\frac{1}{2\sigma^2}\sum_{i=1}^{m}(y_i - f_i(\Theta))^2\} \tag{5.29}$$

From equation (5.23), it gives

$$\frac{\partial l}{\partial \theta_i} = 0 \qquad \text{for } 1 \leq i \leq m \tag{5.30}$$

where

$$l = \sum_{i=1}^{m}(y_i - f_i(\Theta))^2 = (Y - F(\Theta))^T(Y - F(\Theta)) \tag{5.31}$$

which is the same as the least-squares estimation equation (5.4).

These analyses show that Bayesian posterior density function provides a unifying probabilistic framework for least-squares estimation, maximum likelihood estimation and maximum a posteriori estimation. Hence, maximum a posteriori estimation is also called Bayesian parameter estimation. When approaching a mathematical modeling problem, it is sometimes not initially clear whether prior information can be neglected much less whether the simplifying assumptions needed for least squares estimation are appropriate. Thus, it can be useful to start with a Bayesian framework in mind moving toward the more restricted frameworks if and when it becomes clear that they are appropriate.

5.4 Numerical Methods of Multi-dimensional Parameter Optimization

In the Section 5.1, we noted that a least-squares estimator can be obtained by solving a group of linear algebraic equations if the system model function is a linear function of parameter Θ. However, in many situations, the model function is

not linear. We then have to solve a group of nonlinear algebraic equations to obtain the estimator or seek the minimum directly in Θ space. This can then be done using an iterative search procedure, which involves four basic steps:

1. Specify an initial point Θ_0.
2. Select a search direction.
3. Determine the step size along that direction.
4. Compare with the criterion for terminating the search.

In the following, we will introduce several algorithms for multi-dimensional function optimization in Θ space. That is, the value of m variables $\Theta^T = (\theta_1, \theta_2, \cdots, \theta_m)$ are to be chosen to minimize a function $g(\Theta)$.

The method of steepest decent is one of the oldest methods for multi-dimensional optimization. This method takes advantage of the fact that the negative gradient of a function $g(\Theta)$ is locally the direction of the most rapid decreasing of the function value. Starting from an initial guess Θ_0, the successive approximate solution is given by

$$\Theta_{k+1} = \Theta_k - s_k \nabla g_k \tag{5.32}$$

where s_k is the step size along the steepest descent direction at each iteration, which is determined by minimizing $g(\Theta_k - s_k \nabla g_k)$ with respect to s_k. This is a one-dimensional minimization problem that can be solved using gold-section, successive parabolic interpolation or Newton's method [148].

The method of steepest descent is very reliable for reaching a minimum point, but it converges very slowly. In multi-dimensional optimization, we seek zeros of the gradient of function. Thus, the general Newton's method can be used. The iterative scheme has the form

$$\Theta_{k+1} = \Theta_k - H^{-1}(\Theta_k) \nabla g_k \tag{5.33}$$

where H is the Hessian matrix of second partial derivatives of $g(\Theta)$.

$$H_{ij} = \frac{\partial^2 g(\Theta)}{\partial \theta_i \partial \theta_j} \qquad \text{for } 1 \leq i \leq m \tag{5.34}$$

Newton's method is usually very rapidly convergent once it gets close to a solution, but it requires substantial amount of work per iteration to compute the Hessian matrix. Quasi-Newton methods have been developed to reduce its overhead and improve its reliability. The quasi-Newton's methods have the form

$$\Theta_{k+1} = \Theta_k - s_k B_k^{-1} \nabla g_k \tag{5.35}$$

where B_k is some approximation to the Hessian matrix obtained in any of a number of ways, including conjugate gradient search, secant updating, finite difference, periodic reevaluation, or neglecting some terms in the true objective function [148].

The conjugate gradient method provides an alternative to Newton's method, and does not require the explicit calculation of second derivatives. The new search direction will not spoil the miminization obtained along the old direction. A sequence of conjugate search directions, beginning with the negatively gradient initially, modify subsequent gradients so as to accumulate information implicitly about the Hessian matrix as iterations proceed. The algorithm has the form

$$s_0 = -\nabla g(\Theta_0) \tag{5.36}$$

$$\Theta_{k+1} = \Theta_k + s_k x_k \tag{5.37}$$

$$g_{k+1} = \nabla g(\Theta_{k+1}) \tag{5.38}$$

$$\beta_k = \frac{g_{k+1}^T g_{k+1}}{g_k^T g_k} \tag{5.39}$$

$$s_{k+1} = -g_{k+1} + \beta_k s_k \tag{5.40}$$

This algorithm is also called Fletcher and Reeves method [149].

In the preceding discussion, we have assumed that a formula for the gradient of function g is available. In some situations, where the gradient of function is not available or is computational expensive, we may consider using the only function value itself in the optimization algorithm. Powell's method provides an efficient way in multi-dimensional optimization using function values only. This algorithm uses a direction set which does produce m mutually conjugate directions. The algorithm starts by initializing a set of directions $\mathbf{u_i}$ to the basis vectors,

$$\mathbf{u_i} = \mathbf{e_i} \qquad \text{for } 1 \leq i \leq m \tag{5.41}$$

It then repeats the following steps until function converges to the minimum:

1. Save the starting position as P_0.
2. For $i = 1, \cdots, m$, move P_{i-1} to the minimum along direction u_i, and call this point P_i.
3. For $i = 1, \cdots, m-1$, set $\mathbf{u_i} \leftarrow \mathbf{u_{i+1}}$.
4. Set $\mathbf{u_m} \leftarrow P_m - P_0$.
5. Move P_m to the minimum along direction $\mathbf{u_m}$ and call this point P_0.

Powell's method converges quadratically to the minimum point. However, it is possible that the set of directions is linearly dependent. In that case, we have to modify the algorithm. This can be done by discarding the old direction along which the function g made its largest decrease or not adding a new direction at all [150].

The above algorithm can be implemented using an object-oriented programming model. Object-oriented programming is a method of implementation in which programs are organized as cooperative collections of objects, where an object is an entity encapsulating both attributes and behaviors [151]. In an object-oriented statistical parameter estimation model, we can define three levels of object class:

1. Element Classes:
   - Vector class: Define an arbitrary vector array.
   - Dmatrix class: Define a real type (double precision) matrix, its LU decomposition, and determinant.
   - SPDmatrix class: Define a real type (double precision) symmetric positive definite matrix, its Cholesky decomposition and determinant.
   - Func class: Define a real (double precision) single variable function, its derivative, and multivariable function.
2. Tool Classes:

- Min1d class: Define a one-dimension optimization.
- Minmd class: Define a multi-dimension space optimization.

3. Application Classes:

- Likelifunc class: Define a likelihood function including correlation factor.
- MLEstat class: Define a maximum likelihood estimation.

The element class objects are basic objects which are problem independent. This level of classes can be reused in many different computational models without any modification. The tool class objects are a set of collections of numerical algorithms to realize some given functions. This level of classes is general function dependent. It provides a bridge between the element classes and application classes. The application class object is problem dependent object. It depends on the statistical estimation method and the analytical function that we are using here. Through the definition of three levels of class object, the classes in each level keep relatively independent and easy to be reused and extended without affecting the integrity of entire code. New numerical optimization algorithm and new statistical parameters estimation method can be included in the code through local implementation. This also improves the maintenance of code.

5.5 Summary

In the preceding sections, we have introduced least squares, maximum likelihood estimation, and maximum a posteriori estimation methods for parameter estiamtion. We also discussed the numerical algorithms to realize these estimation methods for complex nonlinear function. Least squares method requires a normal distributed likelihood function with identical variance, which is not satisfied for most present tokamak experimental database used in this thesis. Hence, this method is likely not to be useful for the problem studied in this thesis. Maximum likelihood estimation is an appropriate method in the limit of a large number of experimental database. For the limited tokamak database, this method may not be useful, but

may likely to be useful when more experimental database is available. Maximum a posteriori estimation (also called Bayesian estimation) uses both prior information and the information from experimental measurements. It can deal with limited tokamak experimental database used in this thesis. Hence, this method is employed in the following chapters of this thesis to obtain the estimators of adjustable constants in the anomalous tokamak transport model with the database from seven different tokamaks.

Chapter 6

Parameter Estimation in a Gyro-Bohm Transport Model

In the preceding chapter, methods of parameter estimation were introduced. In this chapter, a systematic parameter estimation procedure has been established and applied to estimating a priori uncertain multipliers of flux formulas in a "gyro-Bohm" tokamak transport model. Results from simulating two tokamak discharge profiles with the model calibrated here are shown. This simple example will set the stage for work reported in subsequent chapters of this thesis but without the complexity of a large database. The method used here can deal with limited and relatively uncertain experimental data by using estimates of prior knowledge concerning the accuracy of the data. Confidence regions are given to assess the accuracy of estimators. The estimated multipliers are much larger than in a similar study using non-gyroBohm transport model[71] suggesting either that mechanisms in addition to those included in this particular "gyro-Bohm" model need to to included, as in subsequent chapters of this thesis.

In the following sections, a brief introduction is given in Section 1. The Bayesian estimation method is redescribed in Section 2. The transport model used is revisited in Section 3. Estimation results are presented in Section 4. In Section 5, the transport model are used to simulate two additional discharges. Summary from this work is given in Section 6.

6.1 Introduction

Various combinations of semi-empirical and theory-based transport flux formulas have been used to simulate the radial transport of plasma in tokamaks [22, 56, 61, 62, 152, 65, 60, 27, 47, 58, 153, 71, 64]. A priori uncertain constants in these flux formulas are set either by a nominal assumption or calibrated against experimental data with a simple statistical approach, such as a least squares or maximum likelihood method. The usual least squares method requires experimental data with a simple independent and identical normal distribution around the expectation value. In the Chapter 5, we see that Bayesian method (Maximum a posteriori method) provides a unifying framework of statistical parameter estimation. A simple common maximum likelihood method can be derived as a particular asymptotic approximation of the more general Bayesian method as discussed below, which is appropriate with large amount of experimental data. However, these conditions are not always satisfied in fusion studies. Hence, in this case, we turn back to a direct Bayesian method for parameter estimation. A Bayesian method has been used to study the energy confinement scaling and test an earlier transport model [68, 67]. It takes advantage of both previous experience and on-hand experimental data. The previous experience is quantified in prior distributions which influence the Bayesian posterior probability distribution function, thereby determining confidence limits imposed on a priori uncertain modeling parameters in light of the on-hand experimental data. A proper prior distribution and resultant likelihood function are important for obtaining a good estimation of model accuracy.

In this chapter, a rescaling parameter is used for uncertain variance in normal distributions for residuals between theory predictions and experimental data. Prior distributions of parameters are chosen on the basis of interviews with experimentalists and theorists. The transport model applied here is a gyro-Bohm multi-mode transport model. The only departure from gyrobohm behavior is the finite Larmor radius correction to kinetic ballooning driven fluxes near the ideal magnetohydodynamic (MHD) ballooning stability limit, which is not encountered in the present study. The

experimental data used for model calibration is from ISX-B discharge 41119 [154]. This is an intermediate β (β = kinetic pressure/magnetic pressure), small machine size discharge. The database from this single discharge is used here for an illustrative model calibration for three reasons. First, a single discharge is chosen to simplify the notation and facilitate reproduction of results of this test case by other researchers (as compared to the more complicated database including this discharge used by Kinsey for a statistically more elementary point estimation procedure) [71]. Second, this data set most clearly illustrates the need to allow for a recalibration of reported experimental "error bars", as discussed in more detail below. Third, simulations of this discharge are the most sensitive to ballooning branch transport effects of all the discharges used by Kinsey, and thus should give the smallest confidence intervals from any single discharge for the ballooning branch transport flux multiplier, as also discussed below. The reported data from Thomson scattering electron density and temperature profiles are shown as points with "error bars" in Fig. 6.1. We can see that reported errors systematically exceed the differences between pairs of repeated measurement points. In addition to explaining how we dealt with this problem, we will also show here that estimated transport flux formulae multipliers have relatively large confidence regions, but are relatively insensitive to changes in prior distributions.

6.2 Bayesian Estimation Method

Bayesian estimation is based on Bayes' theorem. Assume that $Y(y_1, y_2, \cdots, y_n)$ is a vector of n observations, its probability distribution with given k parameters $C(c_1, c_2, \cdots, c_k)$ is $p(Y \backslash C)$. Suppose that the probability distribution of C is $p(C)$. Bayes' theorem states that the probability distribution of parameter C after n observations is [155]

$$p(C \backslash Y) = \frac{p(Y \backslash C)p(C)}{p(Y)} \tag{6.1}$$

where

$$p(Y) = \begin{cases} \int p(Y\backslash C)p(C)dC & \text{if C is continuous} \\ \sum p(Y\backslash C)p(C) & \text{if C is discrete} \end{cases} \tag{6.2}$$

In above equation, $p(C\backslash Y)$ is the posterior/conditional distribution of parameter C, $p(C)$ is the prior distribution of C, and $p(Y\backslash C)$ is called likelihood function of C, which is usually denoted as $l(C)$.

Prior distributions represent our initial knowledge about a priori uncertain parameters. Whether or not the distribution is based on a quantitative underlying physical model, there are always some intuitive content in it. This comes from our previous observation experience or our theoretical knowledge about certain parameters. A posterior probability distribution can be regarded as a modification of the assumed prior probability distribution. The modification results from the influence of the likelihood function, which contains information coming from the experimental data set, here called Y.

In our transport model, we let $Y(y_1, y_2, \cdots, y_n)$ denote the experimental output vector with dimension n, and $Y'(y_1, y_2, \cdots, y_n\backslash C)$ denote the system model output vector. For generality, we assume that the "residual" differences between theory predictions and experimental data may include a calibration/model offset and will distribute normally at the j^{th} measurement point. The corresponding likelihood function is

$$l_j(C, f, s) = \frac{1}{(2\pi s\sigma_j^2)^{-1/2}} \exp\left[-0.5\frac{(\epsilon_j(C) - f)^2}{s\sigma_j^2}\right] \tag{6.3}$$

where the vector $\epsilon_j(C) = Y - Y'(C)$. This normal distribution has variance $s\sigma_j^2$, with $s > 0$. Two new parameters, s and f are introduced here into the likelihood function. These two parameters are nuisance parameters with respect to parameters in the theoretical transport model, but they are important in construction of a good likelihood function to connect the experimental data to the statistical model. The parameter f has been introduced elsewhere [71] to account for experimental calibration error or model systematic offset. This may arise from limited instrumental calibration precision or inaccurate modeling methods. Simplification of realistic physical process in the transport model may cause this offset as well. (In the present case with a

single discharge, f is indeterminable and nothing is lost by setting $f = 0.0$. It is discussed only to prepare the reader for extension of the method to a multi-tokamak database, as in subsequent chapters of this thesis.) σ_j is the reported "error bar" of j^{th} experimental data. It represents the dispersion of repeated measurements at the same observation point. The reported error bar may overestimate or underestimate the expected variance for particular measurements. This can be seen from the experimental data shown in Fig. 6.1. Hence, we introduce s as a rescaling factor to deal with such a difficulty. With the assumption that each observation is independent, the total likelihood function for C, f and s is

$$L(C, f, s) = \prod_j l_j(C, f, s) \tag{6.4}$$

From the Bayes' theorem, the posterior probability function of parameters C, f and s after the measurement is

$$p(c, f, s\backslash Y) = p(C)p(f)p(s)L(C, f, s) \tag{6.5}$$

Here $p(C), p(f)$ and $p(s)$ are the prior distribution of C, f and s respectively. As we are only interested here in the parameters in model, the nuisance parameters f and s can be integrated out. The resultant marginal posterior probability function for parameter C is

$$p(C\backslash Y) = p(C) \int \int p(f)p(s)p(Y\backslash C, f, s)dfds \tag{6.6}$$

From the marginal posterior probability function, the estimator of parameter C can be obtained by finding the parameter vector C^* which maximizes the posterior probability function. This is a so-called Bayesian estimation method.

Bayesian estimation provides a method for utilizing to utilize both previous experience and observation data. In the presence of a large amount of previous experience, the chosen prior distribution is close to the true probability distribution, and even a small number of measurements can give an accurate estimation of parameters. If the available knowledge about prior probability is limited, however, we need more observations to make a good estimation.

A common approach is to omit $p(C)$ and set $p(f) = \delta(0)$, and $p(s) = \delta(1)$, with δ the delta function. Then the posterior probability function will be

$$p(C\backslash Y) = \prod_j \frac{1}{(2\pi\sigma_j^2)^{-1/2}} \exp(-0.5\epsilon_j^2/\sigma_j^2) \tag{6.7}$$

Maximizing this $p(C\backslash Y)$ is what conventional maximum likelihood estimation (M.L.E) does. Omitting $p(C)$ is equivalent to taking the uninformative limit for the prior distribution for the modeling parameters. This represents a state of nominal prior ignorance. This may underestimate prior knowledge of theory model parameters. $p(f) = \delta(0), p(s) = \delta(1)$ corresponds to fully informative prior distribution of nuisance parameters with expectation value 0 and 1. This will generally overestimate prior knowledge of these parameters. This is because in tokamak studies, the inherent complexity of plasma behavior and limited diagnostic accuracy may result in potential uncertainties in experimental data other than known variances for each measurement. Therefore, in this work, we will illustrate results which include our best present estimates concerning prior distribution parameters. This leads to the use of semi-informative prior distribution in constructing the posterior distributions. For those used to least squares, we note that, if in Eq. (6.7) we also assume that each measurement has the same variance, we obtain the simple least squares estimation method.

6.3 The Gyro-Bohm Multi-mode Transport Model

The study of plasma transport is an important field concerned with confinement in controlled fusion devices. However, studying this process is both complicated and challenging. A number of theoretical modes have been proposed to explain energy transport in tokamaks. At present, no formulas connected to a single branch of the linear dispersion relation have been clearly shown to reproduce a major portion of available experimental data. One reason is that transport from different branches may dominate to different extents in different regions of a plasma. Therefore, an

appropriate combination of these modes can be expected to give a better fit to available data [45]. This motivates the "multi-mode" transport model, which has been extensively studied by a number of authors [61, 62, 65, 60, 69]. A "multi-mode" transport model includes a linear combination of the drift wave branch and ballooning branch in anomalous particle and energy fluxes formulas. The drift wave branch consists of a contribution from trapped electron mode (TEM), ion temperature gradient (η_i) and circulating electron effects (CE). It accounts for anomalous transport due to small scale fluctuations. The ballooning branch here accounts for resistive ballooning, kinetic ballooning and neoclassical MHD effects. In the model used by Kinsey et al. [71], the radial electron energy transport due to motion along stochastic magnetic field lines is included in resistive ballooning and neoclassical MHD mode. This results from applying a test particle theory in a stochastic magnetic field with nonlinear saturation level estimated from ballooning and neoclassical MHD calculations [103, 104, 111]. However, at present, no clearly relevant experimental evidence supports the existence of strong radial transport due to electron motion along stochastic magnetic fields [156]. Also, there are some questions about the validity of the test particle theory used [157]. The amplitude and correlation lengths for stochastic magnetic fields and their effects on plasma transport are still an active research field. Hence, in this chapter, we will omit electron thermal transport along stochastic magnetic fields in flux formulas. This also simplifies the underlying transport mechanism since the remaining model forms a gyro-Bohm scaling transport model [158, 159, 160]. The detailed transport flux formulas are given in Appendix 1. The resulting fluxes are added to neoclassical transport and incorporated into a set of time-dependent particle and energy conservation equations. This set of equations is solved by finite difference method in BALDUR[138]. The general forms of fluxes used here are

$$Q_e = e^{c_1} Q_e^D + e^{c_2} Q_e^B \tag{6.8}$$

$$Q_i = e^{c_1} Q_i^D + e^{c_2} Q_i^B \tag{6.9}$$

$$\Gamma_a = e^{c_1} \Gamma_a^D + e^{c_2} \Gamma_a^B \tag{6.10}$$

Here, the Q_j for $j = e, i$ are the flux-surface-averaged radial fluxes of electron and ion energy and Γ_a of particle species type a. The multipliers e^{c_1} and e^{c_2} correspond to

the contributions from drift wave and ballooning branch respectively. In this work, we will give an estimation of multipliers from experimental data using a Bayesian method.

6.4 Parameter Estimation in the Gyro-Bohm Multimode Model

Our Bayesian estimation method has been discussed above in Section 2. The experimental data is from ISX-B discharge #41119. All experimental data points are assumed independent. The prior distributions used for the parameters c_1, c_2, s and f are

$$p(c_1) = \frac{1}{\sqrt{2\pi\sigma_{c_1}^2}} \exp(-0.5\frac{c_1^2}{\sigma_{c_1}^2}) \tag{6.11}$$

$$p(c_2) = \frac{1}{\sqrt{2\pi\sigma_{c_2}^2}} \exp(-0.5\frac{c_2^2}{\sigma_{c_2}^2}) \tag{6.12}$$

$$p(f) = \frac{1}{\sqrt{(2\pi\sigma_f^2)}} \exp(-0.5\frac{f^2}{\sigma_f^2}) \tag{6.13}$$

$$p(s) = \frac{\alpha^\alpha}{\Gamma(\alpha)} s^{\alpha-1} \exp(-\alpha s) \tag{6.14}$$

where $\sigma_{c_1}, \sigma_{c_2}, \sigma_f$ and α are adjustable constants. They represent a range of uncertainties in our previous knowledge. In the case of local uninformative prior distributions, $\sigma_{c_1}, \sigma_{c_2}$ and σ_f tend to ∞ and α to 0. As noted above, these assumptions may neglect useful prior knowledge. In the case of fully informative prior distributions, $\sigma_{c_1}, \sigma_{c_2}, \sigma_f \to 0$ and $\alpha \to \infty$. The prior probability distributions then go to $\delta(0)$ and $\delta(1)$ for these two types of limit. As we only use one discharge in this study, f is not needed and we set the prior distribution for f to $\delta(0)$. Interviewing those who provide the data suggested that using $\alpha = 1$ to represent a factor of c. two uncertainty in "error bar" sizes is reasonable.

A number of nonlinear simulations using gyrofluid and gyrokinetic approaches [161, 53, 162], have been done for drift wave branch, producing results within order of mag-

nitude accuracy of each other and of the quasilinear results upon which our formulas for this branch are based. Relatively less work has been done to study the accuracy of ballooning branch formulas used here. Thus, we assume an order magnitude of more uncertainty at the 2σ level for the leading multipliers in the ballooning branch than in drift wave branch. For a nominal study, we thus assume that $\sigma_{c_1} \sim 1, \sigma_{c_2} \sim 2$ in the prior distributions is an appropriate prior state of information about model parameters. From these prior distribution functions, employing the likelihood function defined above in Eq. (6.3), we can obtain the posterior probability function.

One hundred eighty two points in c_1, c_2 space have been sampled to calculate the posterior probability value. The posterior distribution function is obtained by fitting the sampled values using a quadratic function through a least squares method. The resultant posterior distribution is locally equivalent to a Gaussian function. Maximizing the approximated posterior distribution with respect to (c_1, c_2) yields Bayesian estimation parameters. The obtained multiplier for the drift wave branch is $e^{c_1^*} = 3.14$ and for the ballooning branch is $e^{c_2^*} = 4.24$.

Confidence regions are then used to evaluate the accuracy of estimators. As the posterior distribution is approximately Gaussian in this case, the covariance matrix is the negative inverse Hessian matrix of the logarithm of the posterior distribution [163]:

$$V = -H^{-1} = -\begin{vmatrix} \frac{\partial^2 log(p(c_1,c_2/Y))}{\partial^2 c_1} & \frac{\partial^2 log(p(c_1,c_2/Y))}{\partial c_1 \partial c_2} \\ \frac{\partial^2 log(p(c_1,c_2/Y))}{\partial c_1 \partial c_2} & \frac{\partial^2 log(p(c_1,c_2/Y))}{\partial^2 c_2} \end{vmatrix}^{-1} \tag{6.15}$$

The corresponding $100(1-\alpha)\%$ confidence region for the estimators is

$$Pr[(C - C^*)^t V^{-1} (C - C^*) \leq \chi^2_{2,1-\alpha}] = 1 - \alpha \tag{6.16}$$

where $\chi^2_{2,1-\alpha}$ is the upper $100(1-\alpha)$ of percentage of a Chi-square distribution with two degrees of freedom. Eq. (6.15) gives the boundary of confidence region for the estimators. The corresponding $50\%, 90\%$ and 95% confidence levels for estimators from our semi-informative Bayesian estimation are shown in Fig. 6.2. The relatively large confidence regions come from the uncertainties in the small number of experimental data points used here and for our limited prior knowledge.

The change of estimators with respect to the parameter α has been computed and is shown in Fig. 6.3. We can see that the estimator c_1 stays almost constant and c_2 has a weak variation when the α goes up. The 95% confidence area shown in the figure decreases smoothly with increasing α. This insensitivity suggests that a range of uncertainty about our prior knowledge for experimental accuracy is not critical, in the present context, for the results of the analysis.

6.5 Test of the Calibrated Transport Model

The estimated multiplying coefficients $e^{c_1^*}$ and $e^{c_2^*}$ of saturation levels from drift wave and ballooning branches are around $3-4$ times the nominal theoretical unit multipliers. As an indication of whether it is worth pursuing theoretically why such a remarkable model is demanded by this data, we have simulated a "low confinement" (L-mode) and "high confinement" (H-mode) discharge from one large tokamak as an indication of how well it functions experimentally. One discharge is a L-mode shot from Dlll-D (#57342), the other is a H-mode shot from DIII-D (#56511) [164]. These two shots represent a reasonably well matched set in two different confinement regimes. The tokamak parameters, together with those of ISX-B #41119 discharge, are listed in Table 6.1. These include the major radius R_0, outermost closed flux surface half-width a, plasma elongation κ, toroidal magnetic field B_T at R_0, toroidal current I_p, mean atomic number of hydrogen isotope A_i, effective charge Z_{eff} ($Z_{eff} = \sum n_a Z_a^2/n_e$), neutral beam injection power P_{NB}, sawtooth period τ, and diagnostic time.

The simulation results versus experimental data are given in Figs 6.1 and 6.4-5. The electron density and temperature data were obtained by Thomson scattering. The ion temperature data were measured using charge exchange recombination spectroscopy. We can see that the transport model qualitatively reproduces the experimental profiles data. The density and temperature profiles of the H-mode shot fit very well with reported data. However, there exists a noticeable difference between the simulated temperature profile of the L-mode shot and reported data. The

source of additional enhanced transport required in the L-mode discharges is under investigation elsewhere [165, 166].

6.6 Summary

In the above analysis, we employed Bayesian estimation with proper prior distributions and a likelihood function to deal with a case where the experimental observations are limited in number and have relatively large uncertainty. Bayesian estimation gives us the possibility of making optimal use of our previous knowledge. The estimators using data from small size machine and limited data points were applied to the simulation of one larger size machine discharges. The obtained results fit well with experimental data for the DIII-D H-mode case, but give a poor reproduction of the temperature profile for the L-mode case. Without including the radial energy transport of electron motion along stochastic magnetic fields, the gyro-Bohm scaling model has comparatively high turbulence saturation level parameters. These are much larger than in a similar study using non-gyrobohm transport model[71], suggesting that mechanisms in addition to early estimates of $E \times B$ driven fluxes from resistive ballooning and quasilinear drift/η_i turbulence are needed for a complete theoretical model of flux surface averaged transport in tokamaks.

These results illustrate the critical importance of careful nonlinear theoretical studies of underlying transport mechanism. At present, there is a very limited multi-tokamak collection of complete sets of waveforms and sawtooth-phased profiles generally available [72]. If the results shown here are a reasonable guide, some useful a priori constraints on the a priori uncertain parameters in theory-based transport models will be essential for discriminating between various gyro-Bohm and non-gyro-Bohm transport models, even ones with functional dependence of transport flux formulas on other dimensionless parameters as highly constrained as those we used here and by authors such as Kinsey et al [71].

Table 6.1 Tokamak Discharge Parameters

Tokamak	ISXB	DIII-D	DIII-D
Shot #	41119	56511	57342
Type	L	H	L
$R_0(m)$	0.94	1.70	1.70
$a\ (m)$	0.26	0.7	0.636
κ	1.19	1.83	1.67
$B_T(T)$	0.93	2.1	2.12
$I_p(MA)$	0.135	1.25	1.23
A_i	1.22	1.53	1.53
Z_{eff}	1.30	1.40	1.3
$P_{NB}(MW)$	2.00	6.68	7.21
$\tau_{saw}^{OH}(secs)$	0.005	0.013	0.014
$\tau_{saw}^{NB}(secs)$	0.01	0.014	0.0385
Diagnostic Time $(secs)$	0.22	2.09	2.40

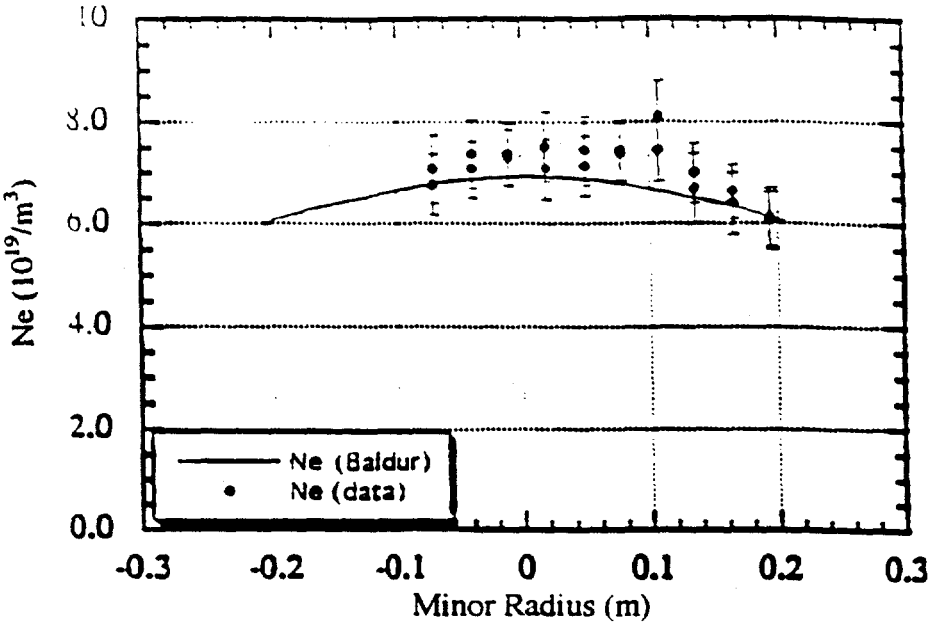

(a)

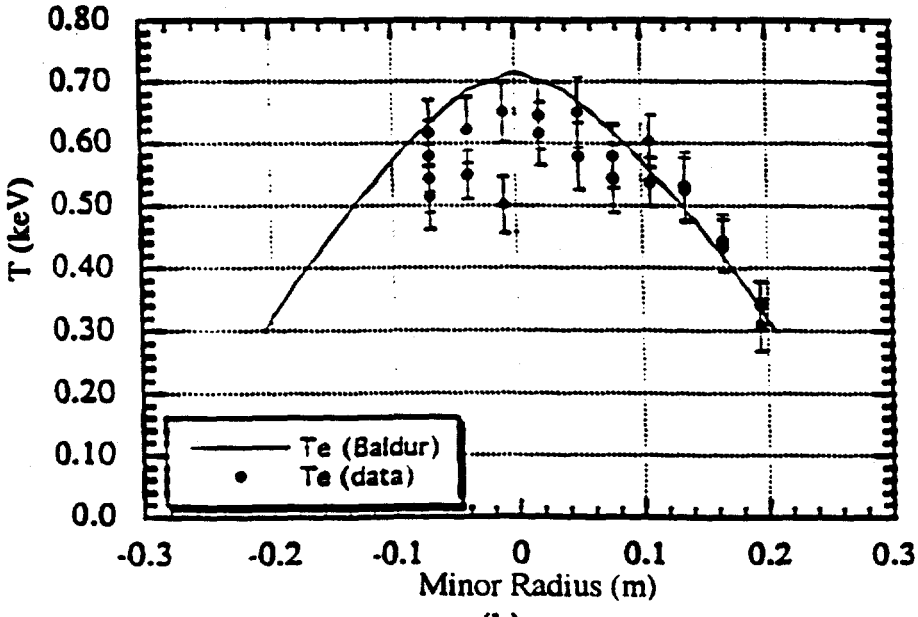

(b)

Fig. 6.1: (a) Electron density profile, (b) electron temperature profile as a function of minor radius compared with experimental data from L-mode ISX-B shot 41119.

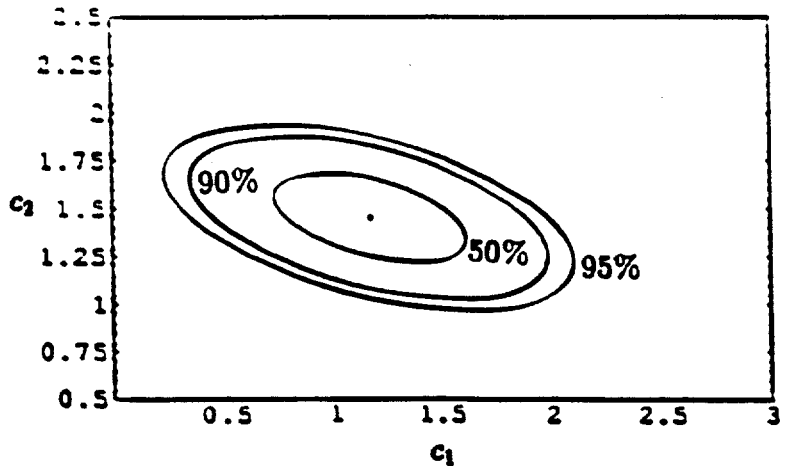

Fig. 6.2: The 95%, 90% and 50% confidence regions of c_1^* and c_2^*.

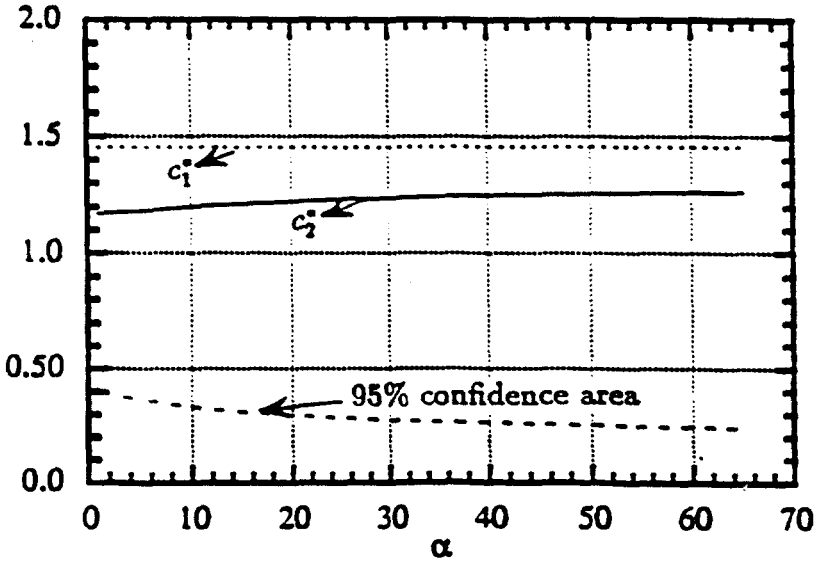

Fig. 6.3: C_1^*, c_2^* and 95% confidence area versus α in the prior distribution of s.

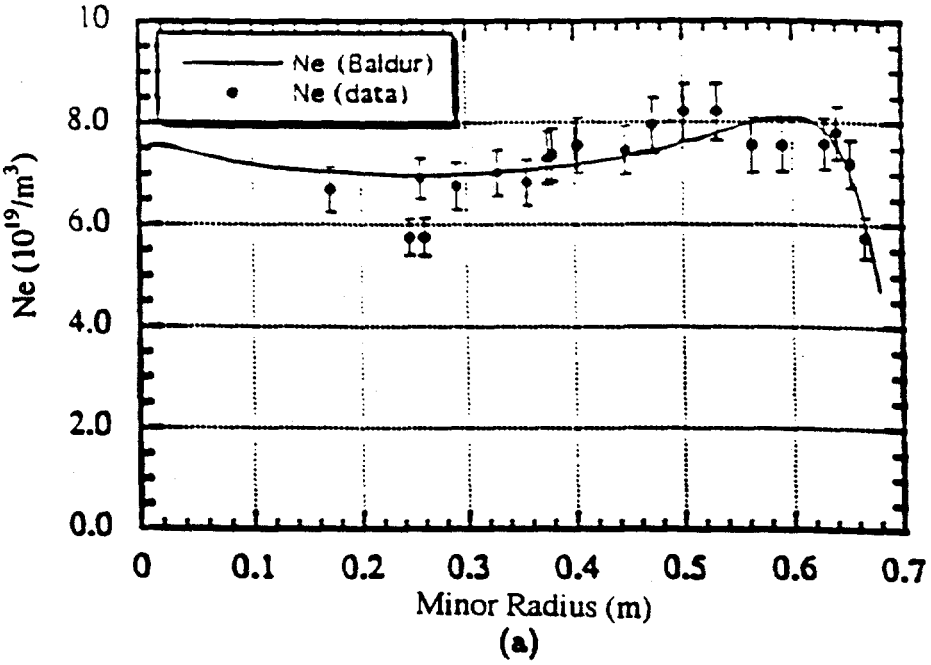

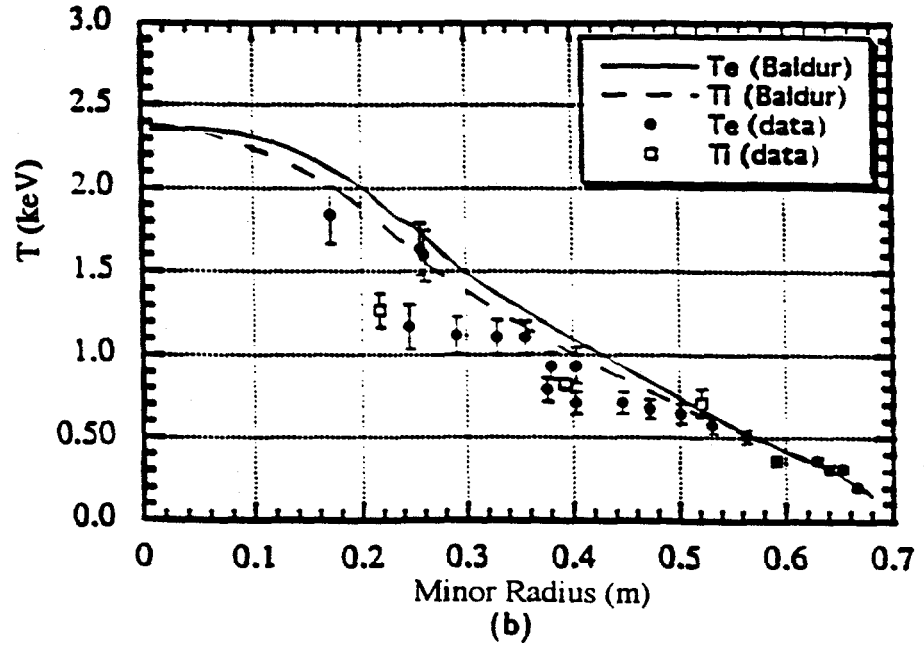

Fig. 6.4: (a) Electron density profile, (b) electron and ion temperature profiles as a function of minor radius compared with experimental data from H-mode DIII-D shot 56511.

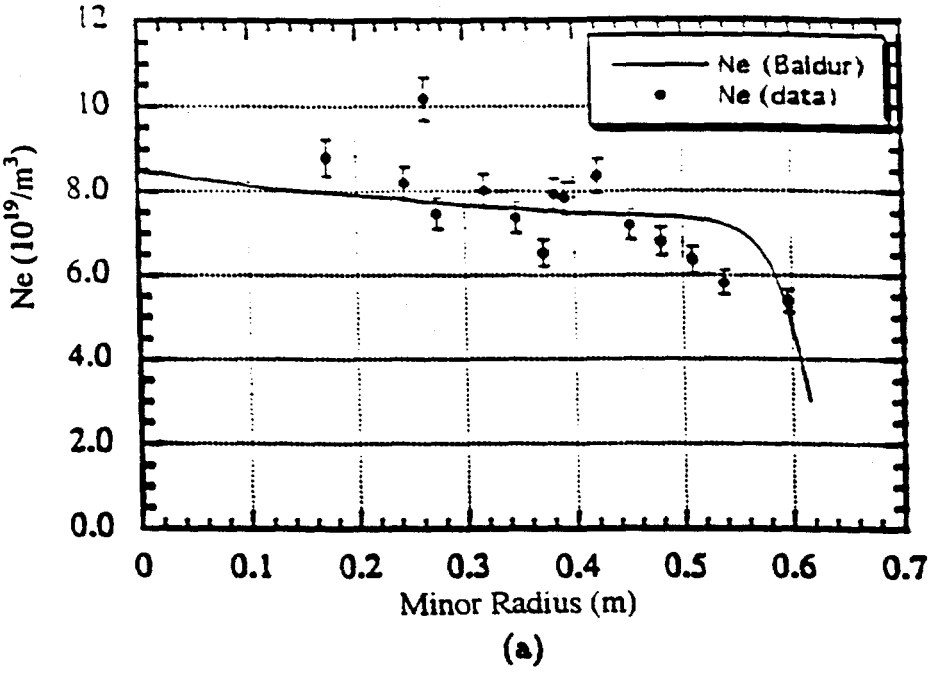

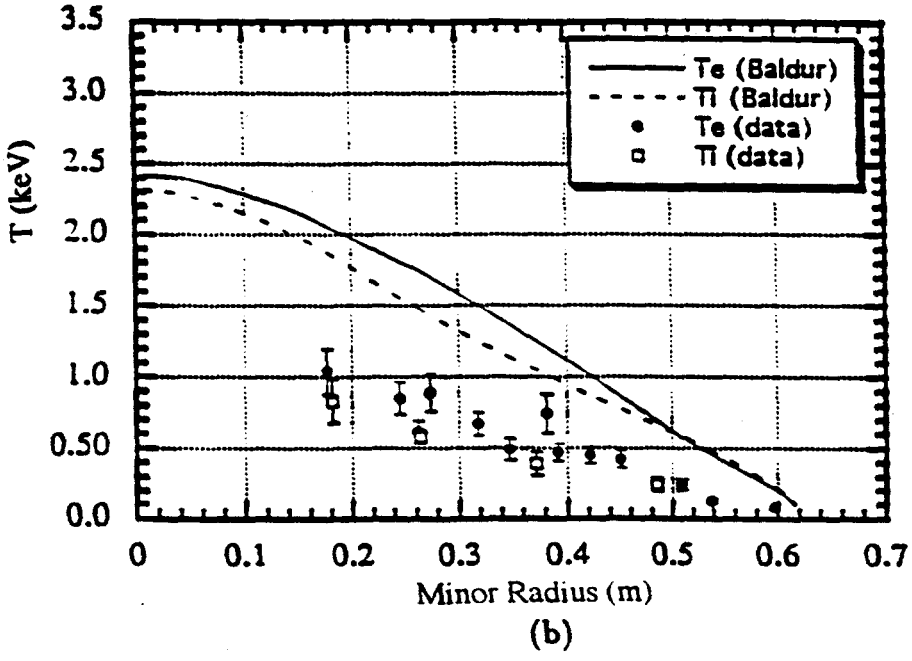

Fig. 6.5: (a) Electron density profile, (b) electron and ion temperature profiles as a function of minor radius compared with experimental data from L-mode DIII-D shot 57342.

summarized in Section 4. Results and their implications are discussed in Section 5. Finally, we summarize this work in Section 6.

7.1 Introduction

A theory-based transport model has been proposed and tested against a wide range of experimental data [61, 62, 60, 64, 71, 72]. This model includes a linear combination of two primary turbulent radial fluxes from the drift wave and ballooning branches of the dispersion relation describing linear instabilities for tokamak plasmas. In previous studies, turbulence saturation coefficients were nominally set to unity or calibrated from limited experimental data using a simple least squares or maximum likelihood approach [62, 60, 71]. From the study described in the previous chapter, we saw that a Bayesian method provides an effective method for parameter estimation. In this chapter, we employ this method to estimate turbulenct transport flux coefficients using a database reflecting a wide variety of tokamak operational conditions.

The Bayesian method generalizes conventional least squares or maximum likelihood methods by taking full advantage of both previous experience and experimental evidence when making inferences about priori uncertain parameters. Use of such prior knowledge is important when the experimental observations come with relatively large uncertainty and incompletely characterized accuracy. A good utilization of prior knowledge optimizes point estimation and the determination of confidence contour, which indicates the probability the true value of a parameter being in given regions of parameter space; otherwise the amount of data required to obtain a desired accuracy may be over-estimated [163].

In this chapter, we base our prior knowledge on extensive studies of present theoretical models and interviews with experimental teams. A systematic calibration or model offset error is allowed for. Reported measurement variance is also allowed to be rescaled, as reported experimental variance occasionally overestimates or underestimates the measurement variance.

The experimental data used here includes twelve discharges from seven toka-

maks. The data covers three major operational regimes: Ohmic heating (OH), low confinement (L-mode) and high confinement (H-mode). These discharges span a wide tokamak parameter space. Confidence contours are given to describe the expected accuracy of the estimation. These confidence contours show a larger uncertainty in ballooning than in drift wave branch fluxes. (This is also coincidentally the case with present purely theoretical nonlinear studies from gyrofluid and gyrokinetic models [53, 161, 162].) The turbulence saturation coefficients are computed here for various values of parameters describing a priori uncertainties in prior distributions. The results show that the point estimators, i.e. calibrated turbulence saturation coefficients, obtained are not sensitive to the variation of prior distributions. However, the confidence regions obtained are relatively sensitive to change of a parameter α, which accounts for the prior knowledge of the accuracy of reported data "error bars", but are insensitive to the change of a parameter δ_f, which accounts for prior knowledge about systematic calibration/modeling offsets. The insensitivity of point estimators to variation of these parameters implies that some uncertainties in our prior subjective knowledge will not dramatically affect "point simulation modeling" using the calibrated transport model. However, those interested in the range of possible extrapolations which can be obtained would be advised to pay careful attention to a priori assumptions used in estimating the accuracy of their models.

The transport model calibrated here is further implemented to predict plasma profiles from an additional Tokamak Fusion Test Reactor (TFTR) discharge 50904 [159]. The predicted temperature profiles agree well with experimental data.

7.2 Multi-mode Transport Model

The transport model used here is referred to as a "multi-mode" model. It linearly combines turbulence saturation estimates of fluxes from drift wave and ballooning branches. This approach originated from the observation that no single theoretical mode or branch at present can well reproduce a large variety of experimental data [45, 46, 58]. Several older "multi-mode" model versions had previously

been used for testing against experimental data [62, 60, 65, 66]. In this chapter, we calibrate the turbulence saturation coefficients of two branches in a recent published nominal model [71]. In the nominal "multi-mode" transport model, the drift wave branch includes effects of trapped electron, ion temperature gradient and circulating electron modes. The ballooning branch includes effects from resistive ballooning, kinetic ballooning and neoclassical MHD theories. The resulting fluxes are added to neoclassical transport and incorporated into a set of time-dependent, flux-surface-averaged particle and energy conservation equations. This set of equations is solved using finite difference methods in the transport code BALDUR [138]. The general form of fluxes used here can be written as

$$Q_e = e^{c_1} Q_e^D + e^{c_2} Q_e^B \tag{7.1}$$

$$Q_i = e^{c_1} Q_i^D + e^{c_2} Q_i^B \tag{7.2}$$

$$\Gamma_a = e^{c_1} \Gamma_a^D + e^{c_2} \Gamma_a^B \tag{7.3}$$

Here Q_e and Q_i are the flux-surface-averaged radial fluxes of electron and ion energy, and Γ_a denotes the particle fluxes of particle species type a. The multipliers c_1 and c_2 define a priori uncertain turbulence saturation coefficients subject to calibration against experimental data.

7.3 Systematic Calibration Method

A Bayesian estimation method is employed to calibrate the a priori uncertain parameters in the multi-mode model against experimental data. It is based on Bayes' conditional probability theorem [155]. For any given data, the theorem describes the probability distribution of parameters as

$$p(C/Y) = \frac{p(Y/C)p(C)}{\int p(Y/C)p(C)dC} \tag{7.4}$$

Here, $p(C/Y)$ is the posterior/conditional distribution of parameters C with given data Y, $p(C)$ is the prior distribution of C, and the function $p(Y/C)$ is called likelihood function of C, which is the probability distribution of Y given parameters C,

conventionally written as $l(C)$. In the above expression, C is the vector form of a priori uncertain parameters c_1, c_2, and Y is a vector of experimental data.

The prior distribution $p(C)$ comes from previous experience. The likelihood function depends on the statistical model used for the measurement residuals between theory predictions and reported experimental data. Here, we assume the likelihood function for the j^{th} measurement in the i^{th} discharge is

$$l_{ij}(C, f_i, s_i) = \frac{1}{(2\pi s_i \sigma_{ij}^2)^{-1/2}} \exp\left[-0.5\frac{(\epsilon_{ij} - f_i)^2}{s_i \sigma_{ij}^2}\right] \tag{7.5}$$

where the vectors $\epsilon_{ij} = \ln(Y_{ij}) - \ln(Y'(C)_{ij})$ [47]. Y'_{ij} is the model simulation results corresponding to data Y_{ij} of j^{th} measurement in the i^{th} discharge. The parameter f_i accounts for systematic calibration error or modeling offset in the i^{th} discharge. This may arise from limited instrumental precision of the diagnostic method and/or incompletely accurate transport simulation methods. σ_{ij}^2 is the reported data variance (inferred from reported "error bars") for the j^{th} measurement of i^{th} shot. The meaning of "error bars" inferred from data available to us is often not precisely reported. In some cases, the reported "error bars" are clearly larger than discrepancies between repeated measurements (c.f. ISXB discharge #41119 [154] below.) In the other cases, only some data points are reported with "error bars," and we estimate the "error bars" for other data points by assuming that they have the same fractional error. Therefore, the resulting σ_{ij} used here may underestimate or overestimate the true data variance. It is convenient to allow for a rescaling factor s_i such that $s_i\sigma_{ij}^2$ is assumed to be the true data variance in the likelihood function. The reasonable extent of such modification allowed can be quantitatively described by a prior probability distribution for s_i. Similar comments apply to the calibration modeling offsets f_i and transport flux multiplier exponents, c_1 and c_2. Prior distributions for all these parameters with appropriate uninformative limits are given as

$$p(c_{1,2}) = \frac{1}{\sqrt{2\pi\sigma_{c_{1,2}}^2}} \exp(-0.5\frac{c_{1,2}^2}{\sigma_{c_{1,2}}^2}) \tag{7.6}$$

$$p(f_i) = \frac{1}{\sqrt{(2\pi\sigma_f^2)}} \exp(-0.5\frac{f_i^2}{\sigma_f^2}) \tag{7.7}$$

$$p(s_i) = \frac{\alpha^\alpha}{\Gamma(\alpha)} s_i^{\alpha-1} \exp(-\alpha s_i) \tag{7.8}$$

where $\sigma_{c_{1,2}}, \sigma_f$ and α are adjustable constants and Γ is the gamma function with $\Gamma(\alpha+1) = \alpha\Gamma(\alpha)$. These functions represent a range of uncertainties in our prior knowledge about calibration and rescaling factors. With the assumption that the measurements are independent, the posterior probability distribution function of parameters C, f_i and s_i with given data is

$$p(C, f_i, s_i) = p(C) \prod_{ij} p(f_i) p(s_i) l_{ij}(C, f_i, s_i) \tag{7.9}$$

As we are only interested in the parameter $C(c_1, c_2)$ in the present work, the nuisance parameters f_i and s_i can be integrated out. The resultant marginal posterior probability distribution function for C is

$$p(C/Y) = p(C) \int \cdots \int p(C, f_i, s_i) df_i \cdots ds_i \tag{7.10}$$

From the marginal posterior probability function, an estimator C can be obtained by finding the parameter vector $C^*(c_1^*, c_2^*)$ which maximizes the posterior probability. One hundreds eighty two points in c_1, c_2 space have been sampled to calculate the posterior probability value. The posterior distribution function is obtained by fitting the logarithm of sampled values using a quadratic function through a least squares method. The resultant posterior distribution is locally approximated here as a Gaussian function. The covariance matrix of estimators is [163]

$$V = -H^{-1} = -\begin{vmatrix} \frac{\partial^2 log(p(c_1,c_2/Y))}{\partial^2 c_1} & \frac{\partial^2 log(p(c_1,c_2/Y))}{\partial c_1 \partial c_2} \\ \frac{\partial^2 log(p(c_1,c_2/Y))}{\partial c_1 \partial c_2} & \frac{\partial^2 log(p(c_1,c_2/Y))}{\partial^2 c_2} \end{vmatrix}^{-1} \tag{7.11}$$

The corresponding $100(1-\alpha)\%$ confidence region for estimators is

$$Pr[(C - C^*)^t V^{-1} (C - C^*) \leq \chi^2_{2,1-\alpha}] = 1 - \alpha \tag{7.12}$$

where $\chi^2_{2,1-\alpha}$ is the upper $100(1-\alpha)\%$ of point of Chi-square distribution with two degrees of freedom, and Pr specifies the probability. Eq. (7.12) gives the boundary of confidence region for estimator c_1, c_2.

7.4 Experimental Database

The experimental data used for our calibration have been published in Kinsey's paper and Ph.D. thesis [70, 71]. This group of data was carefully chosen from twelve discharges from seven different tokamaks to account for a variety of operational conditions without introducing any known bias other than avoiding the regimes inappropriate to the transport simulation method used here [71]. There are four Ohmic heating (OH), five low confinement (L-mode) and three high confinement (H-mode) discharges. VH modes or supershots are not included due to lack of models of poloidal shear flow and hot ion effects in the flux formulas used here. Since the calculated penetration depth for pellet injection will vary with saturation coefficients in our transport model, a different launching speed is required for each case. Therefore, it is inconvenient to scan transport multipliers with pellet injection simulations. No pellet injection discharges are included in this calibration.

The global plasma parameters for the data used here are presented in Tables 7.1 and 7.2. Note that the last discharge is saved for testing the resulting model and is not used for transport model calibration. Parameters listed are the major radius R_0, minor radius a, elongation κ, toroidal field B_t, toroidal plasma current I_p, line-averaged effective charge $\overline{Z}_{eff}$, neutral beam injection power P_{NB}, average atomic number A_i of the hydrogen isotopes, sawtooth periods τ, final sawtooth time prior to the diagnostic time t^*_{saw}, and the diagnostic time. From Table 7.1 and 7.2, we can see that the major radius ranges from half a meter to several meters, magnetic field changes from less than one Tesla to more than eight Tesla, plasma current varies from just over a tenth MA to several MA, line-averaged density changes from several $10^{19}/m^3$ to $20 \times 10^{19}/m^3$, injection power ranges from two MW to fifteen MW. The heating methods include Ohmic heating, neutral beam injection heating and ion cyclotron resonant heating ($ICRH$). The large parameter space should help to randomize the calibration/modeling offset among various tokamak and make the calibration robust. All together, six hundred ninety seven data points are used in this calibration.

7.5 Calibration Results and Implications

Calibration results have been obtained using the posterior probability distribution discussed in Section 3 and experimental data from discharges summarized in Section 4. For the posterior distribution, we assumed a semi-informative prior distribution of parameters f_i and s_i. Interviewing those who provided the data suggested that using $\delta_f = 0.1$ and $\alpha = 1$ in these prior distributions is reasonable. These represent 10% uncertainty for experimental data and modeling accuracy and c. factor of two uncertainties for the reported "error bars". Confidence contours for the two turbulence saturation parameters from experimental data give a measure of uncertainties remaining after calibration to these data.

Figs. 7.1 and 7.2 show two groups of calibrated saturation coefficients and corresponding 50%, 90% and 95% confidence contours. The relatively small confidence contours shown in Figs. 7.1 and 7.2 indicate that reasonably useful estimators may have been obtained. From the range of confidence contours, we can see that the multiplier of the ballooning branch is more uncertain than that for the drift wave branch. Thus, this study refines purely theoretical estimates consistent with gyrofluid and gyrokinetic studies, which produce results within an order of magnitude accuracy of each other and of the quasilinear results upon which the drift wave branch is based [161, 53, 162]. It leaves relatively larger uncertainties in the ballooning branch, as did the theories we started with. The different estimators and confidence contours in Figs. 7.1 and 7.2 report confidence contours using the different prior distributions for s_i and f_i. From these results, readers with different views of the appropriate values of these parameters may use these figures to come to their own conclusions about the accuracy of our estimators. In Fig. 7.1, the α in the s_i prior distribution varies between $1.0, 6.0$ and 12.0, while δ_{f_i} is kept at 0.1 in the prior distribution for f_i. The resultant point estimators vary only slightly in the parameter space. On the other hand, an appreciable reduction of confidence regions can be observed as α increases. In Fig. 7.2, the δ_{f_i} varies between $0.05, 0.1$ and 0.2 in the prior distribution of f_i, while the α stays at 1.0 in the prior distribution of s_i. Here, both

the resulting estimators and confidence contours are nearly unchanged. Thus, from Figs. 7.1 and 7.2, we see that the calibrated saturation coefficients are insensitive to the change of prior distribution. This allows people with different views of prior knowledge about calibration/modeling offset and "error bar" accuracy to obtain very similar estimators. However, as the confidence contours will vary with prior knowledge assumed about s_i, adequate allowance should be made for uncertainty in the meaning of reported error estimates until any such uncertainty is resolved, at least to the extent that high confidence is required in tokamak performance predicted using these models.

The resultant turbulence saturation coefficients obtained with the "nominal" statistical model described above are $e^{c_1} = 1.03$ and $e^{c_2} = 0.50$ for drift wave branch and ballooning branch respectively. The electron density, electron and ion temperature profiles of the discharges used for calibration using this calibrated transport model are shown along with experimental results in Fig. 7.3-14. These plots are included to allow the reader to conclude whether further refinement of the statistical model used here might be desirable.

As an application of the calibrated model, TFTR discharge 50904 is simulated using it. This discharge is chosen with no obvious selection effects other than being representative of the available large machine L-mode discharges data. The electron density, electron and ion temperature profiles are given in Fig. 7.15 and compared with measurement data. These predicted profiles are in good qualitative agreement with experimental data.

7.6 Summary

In the preceding discussion, we presented a detailed statistical model for calibrating the saturation coefficients in a theory-based multi-mode transport model. Confidence contours were employed to evaluate the accuracy of the estimators we obtained. The relatively small confidence regions obtained suggest that these estimators may be useful. To allow for different views of prior knowledge (which influence the posterior distribution), sensitivity tests were done by varying the adjustable constants in the prior distributions of calibration/model offsets (f_i) and "error bar"

rescalings (s_i). The estimators were found to vary little with respect to the change of prior distribution of f_i and s_i. This gives us some flexibility in making use of prior distributions. However, the confidence contours of estimators do change with the adjustable constant α in the prior distribution for s_i. Therefore, one needs to be careful to examine such effects upon various calibrated models when applying them to performance probability studies. Having sufficient understanding of the statistical model underlying these estimators is essential to appreciating the meaning of these results.

The electron density, electron and ion temperature profiles for twelve discharges are given from the calibrated transport model. A test run of the calibrated transport model on TFTR discharge 50904 yields encouraging results.

Table 7.1. Discharge Parameters

Tokamak	Alc-C	ASDEX	ISX-B	TFTR	DIII-D	JET
Shot	80	8475	41119	45980	56511	15894
Type	Ω	Ω	L-	L-	H-	H-
R_o (m)	.64	1.64	.94	2.45	1.70	2.96
a (m)	.165	.40	.26	.80	0.70	1.10
κ	1.00	1.00	1.19	1.00	1.83	1.55
B_T (T)	8.10	2.30	.924	4.76	2.10	3.43
I_p (MA)	.38	.375	.154	2.00	1.25	3.03
$\bar{n}_e(10^{19}/m^3)$	20.0	4.38	6.87	3.44	7.30	5.25
A_H	1.93	1.93	1.22	1.93	1.53	1.93
Z_{eff}	1.25	1.25	1.30	2.20	1.40	3.46
P_{NB} (MW)	0.0	0.0	2.00	11.34	6.68	7.62
τ_{saw}^{OH}	.032	.013	.005	.025	.013	.080
τ_{saw}^{NB}	-	-	.010	.160	.014	.380
t_{saw}^{*}	.299	.986	2.08	3.36	2.08	15.05
Diagnostic Time(secs)	0.30	1.00	0.22	3.47	2.09	16.0

Table 7.2. Discharge Parameters

Tokamak	Alc-C	ASDEX	DIII-D	TFTR	JET	JFT-2M	*TFTR*
Shot	67	18716	41119	45980	27658	73488	50904
Type	Ω	Ω	L-	L-	L-	H-	L-
R_o (m)	.64	1.65	1.69	2.45	2.95	1.31	2.45
a (m)	.165	.40	.624	.80	1.18	0.33	0.798
κ	1.00	1.00	1.85	1.00	1.44	1.30	1.00
B_T (T)	9.00	2.17	2.00	4.77	1.70	1.26	2.86
I_p (MA)	.54	..38	1.00	1.78	2.06	.222	1.19
$\bar{n}_e(10^{19}/m^3)$	23.3	4.70	2.80	5.30	2.70	4.83	2.66
A_H	1.93	1.93	1.93	1.93	1.93	1.93	1.93
Z_{eff}	1.25	1.30	1.40	2.10	3.30	2.00	2.10
P_{NB} (MW)	0.0	0.0	2.00	14.80	4.10	0.61	7.31
τ_{saw}^{OH}	.032	.013	.026	.05	.08	.01	0.05
τ_{saw}^{NB}	-	-	.080	.23	.38	-	0.165
t_{saw}^{*}	.29	1.39	3.86	3.98	54.80	0.64	3.87
Diagnostic Time(secs)	0.30	1.40	3.90	4.03	55.0	0.754	3.95

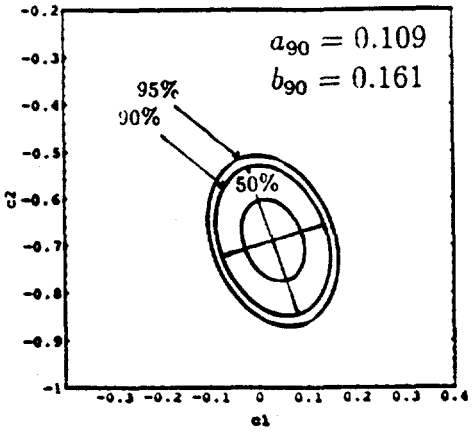

(a)

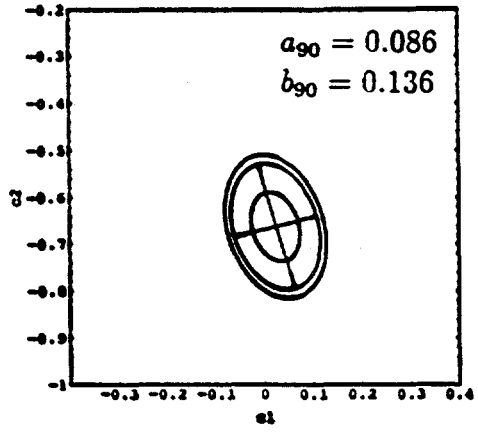

(b)

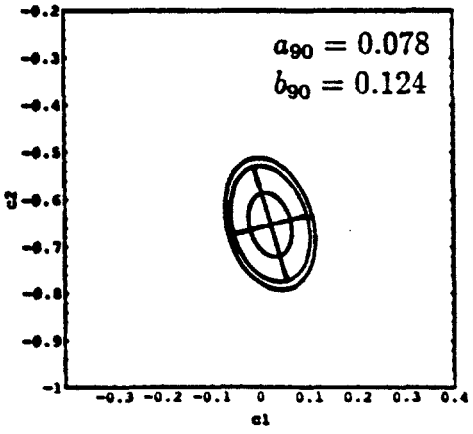

(c)

Fig. 7.1: 50%, 90% and 95% confidence contours for estimators (c_1^*, c_2^*) with (a) $\alpha = 1.0$, (b) $\alpha = 6.0$, (c) $\alpha = 12.0$ and constant δ_{f_i} in prior distributions.

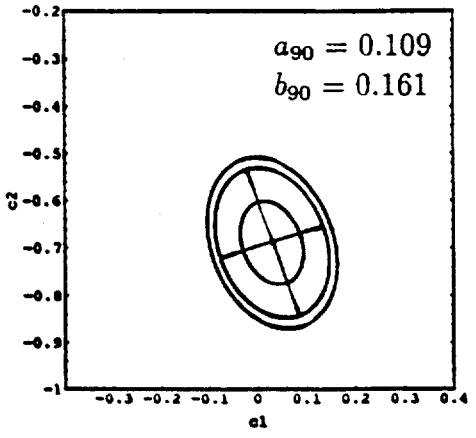

(a)

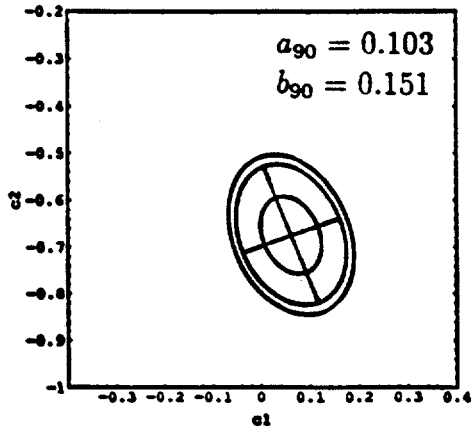

(b)

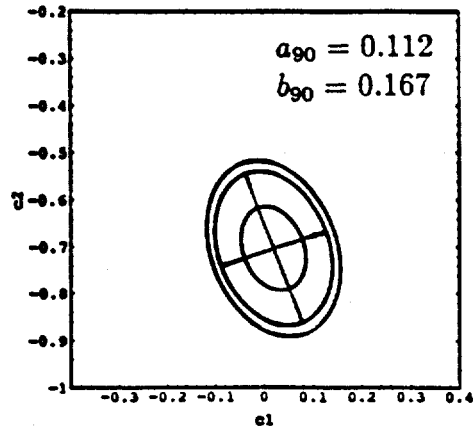

(c)

Fig. 7.2: 50%, 90% and 95% confidence contours for estimators (c_1^*, c_2^*) with (*a*) $\delta_{f_i} = 0.1$, (*b*) $\delta_{f_i} = 0.05$, (*c*) $\delta_{f_i} = 0.2$ and constant α in prior distributions.

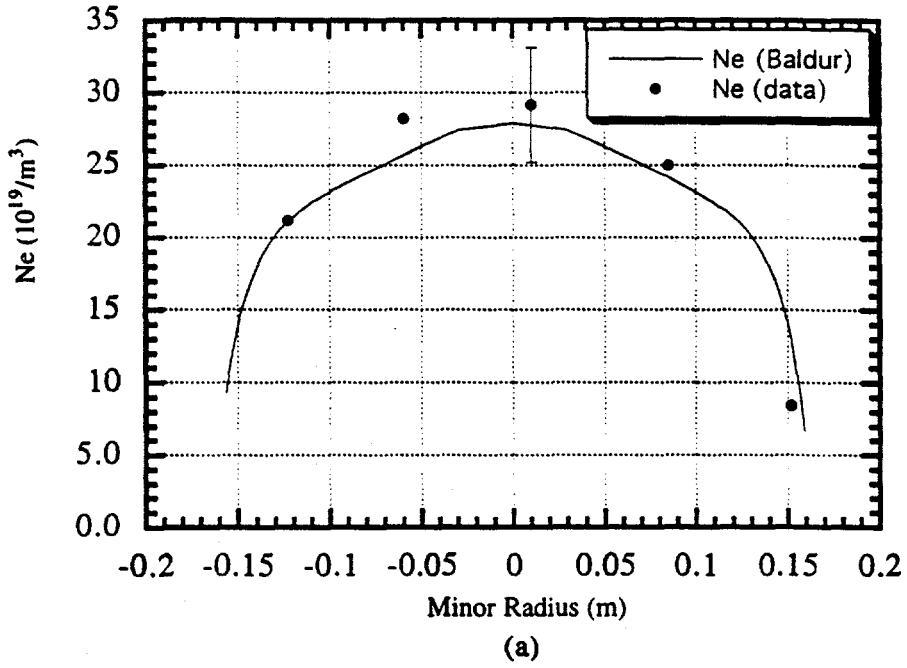

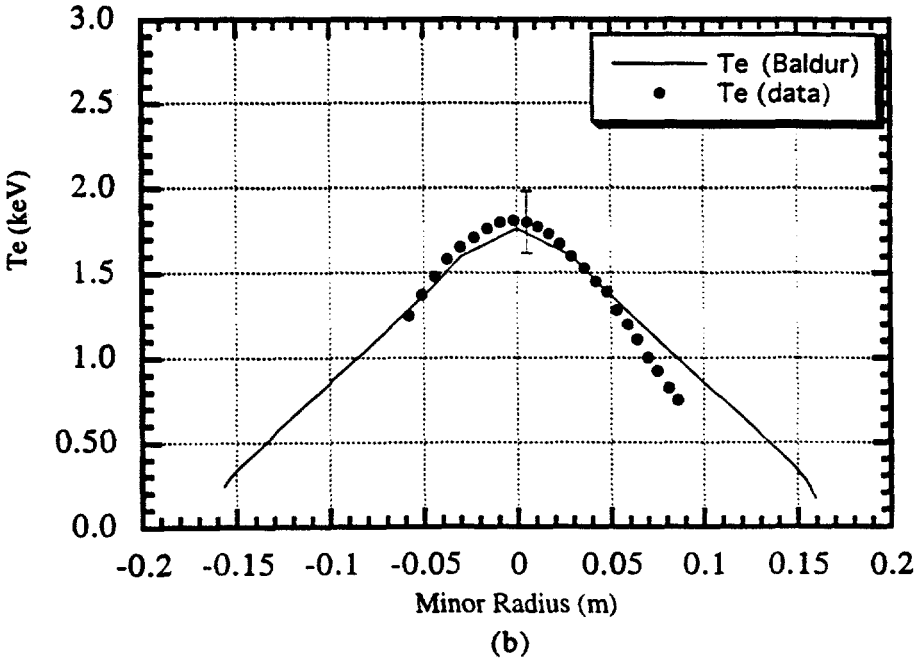

Fig. 7.3: (a) Electron density and (b) electron temperature as functions of minor radius compared with experimental data from Alcator-C, shot 67.

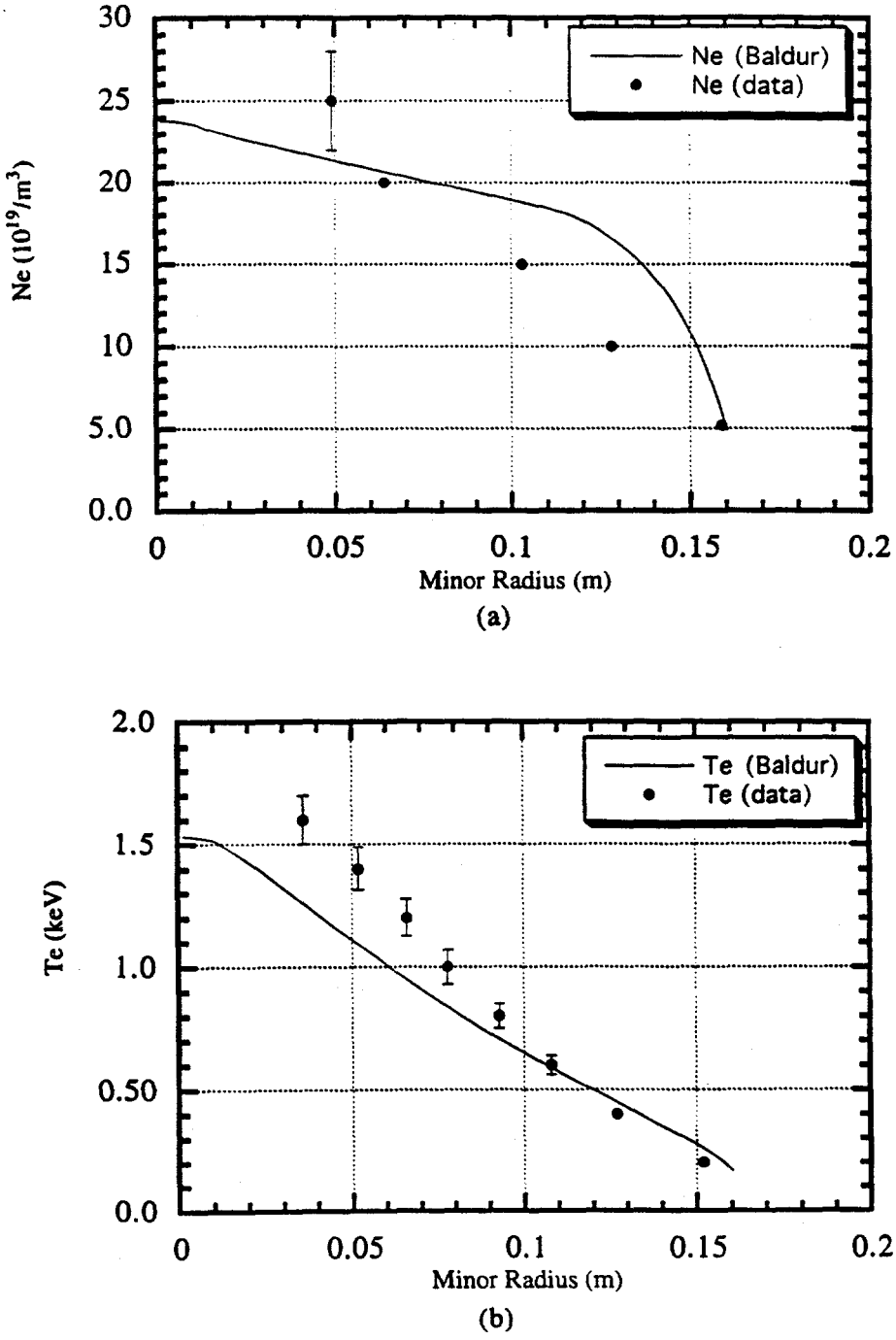

Fig. 7.4: (a) Electron density and (b) electron temperature as functions of minor radius compared with experimental data from Alcator-C, shot 80.

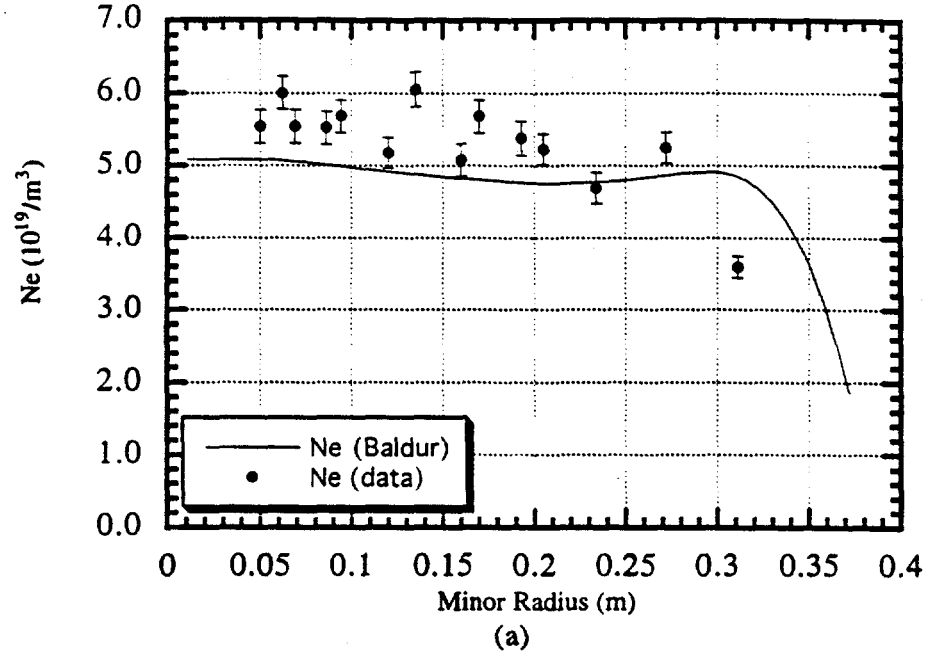

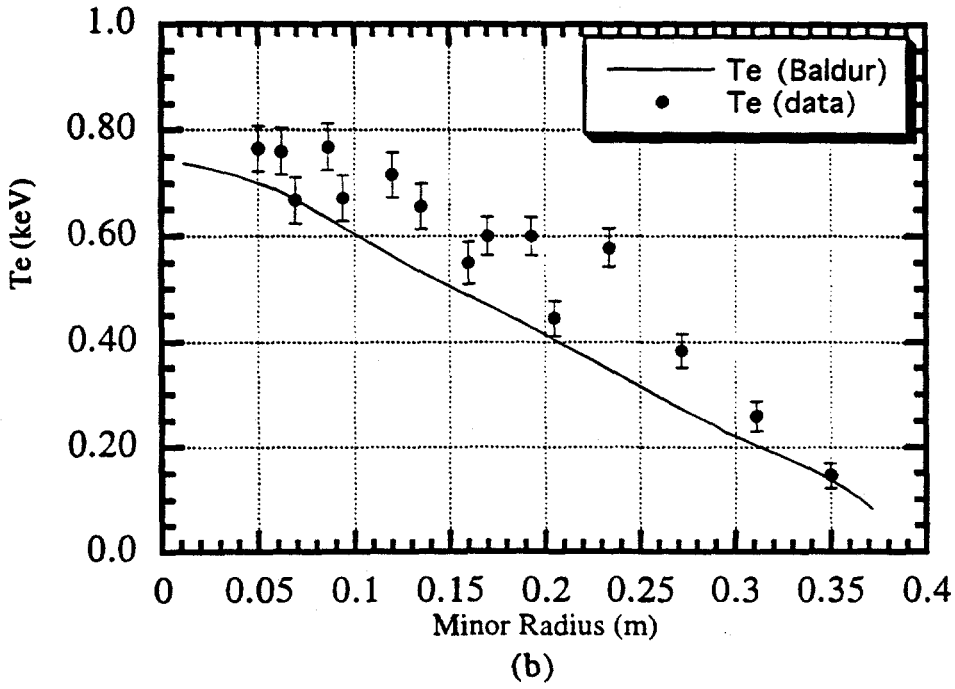

Fig. 7.5: (a) Electron density and (b) electron temperature as functions of minor radius compared with experimental data from ASDEX, shot 18716.

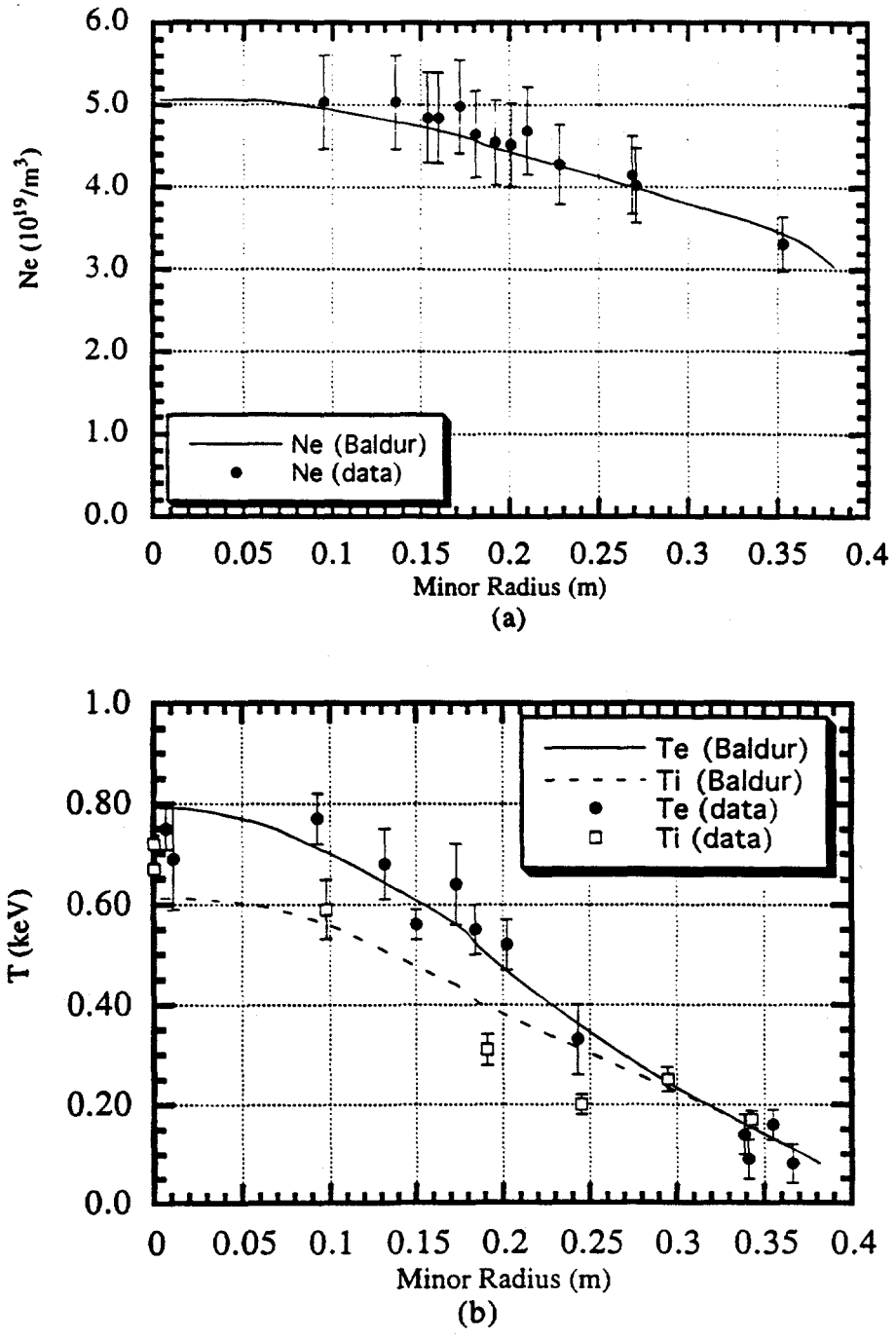

Fig. 7.6: (a) Electron density and (b) electron and ion temperature as functions of minor radius compared with experimental data from ASDEX, shot 8475.

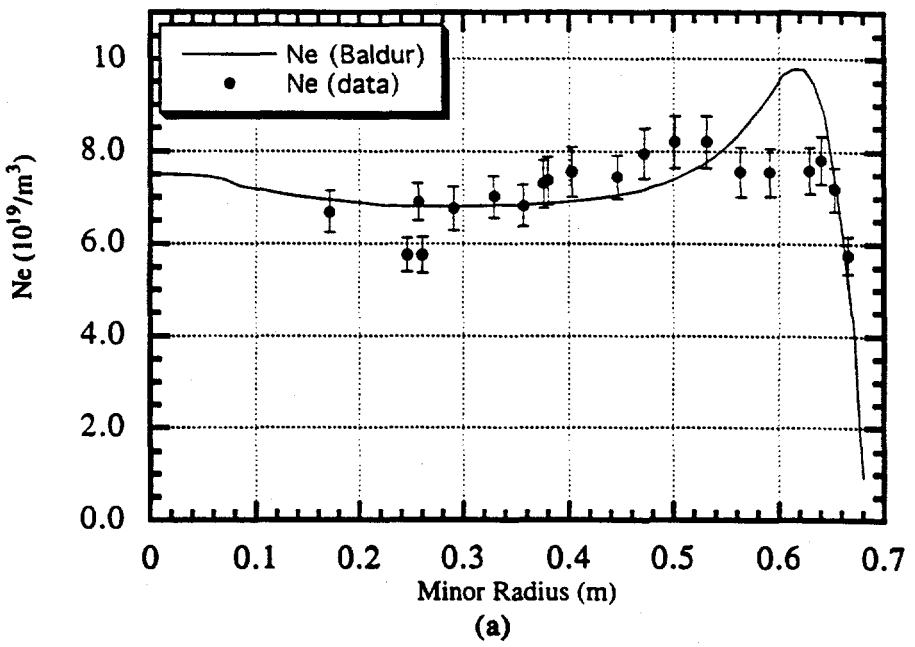

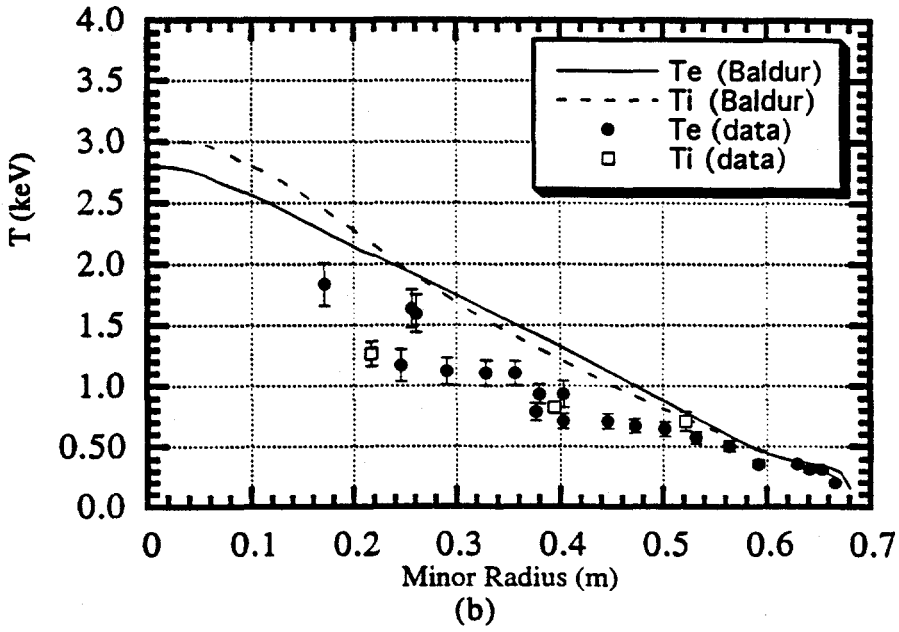

Fig. 7.7: (a) Electron density and (b) electron and ion temperature as functions of minor radius compared with experimental data from DIII-D, shot 56511.

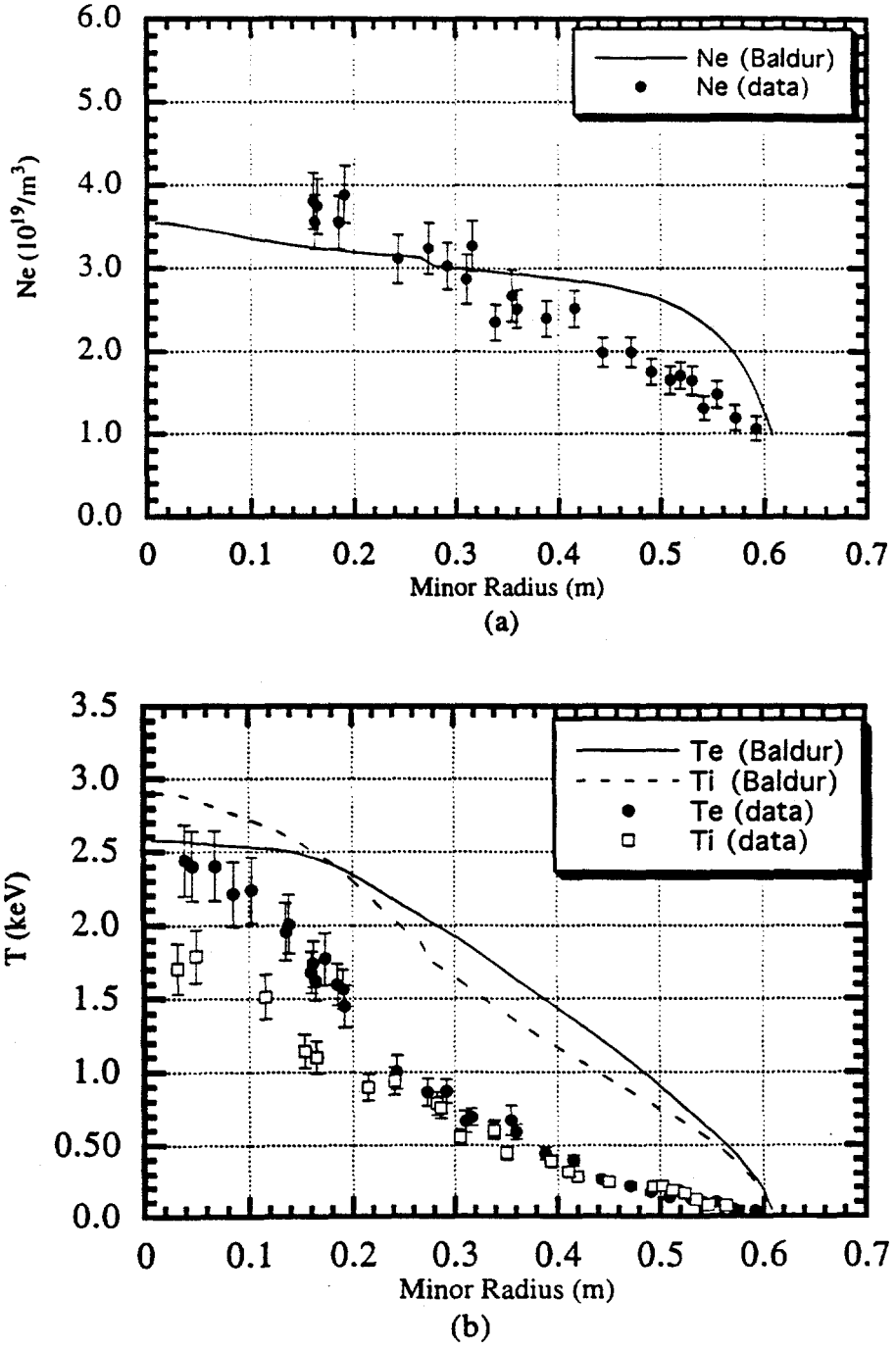

Fig. 7.8: (a) Electron density and (b) electron and ion temperature as functions of minor radius compared with experimental data from DIII-D, shot 78109.

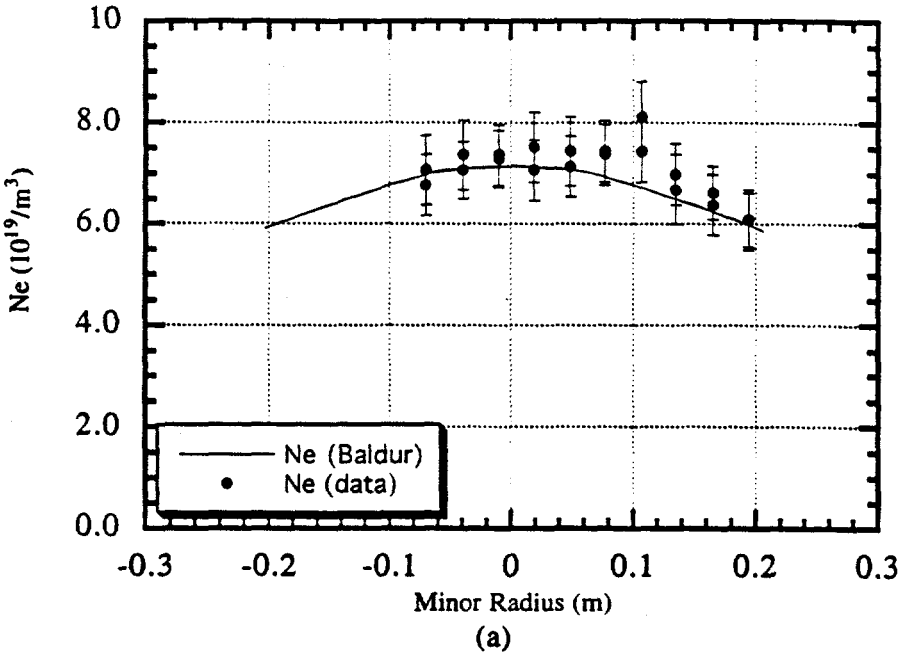

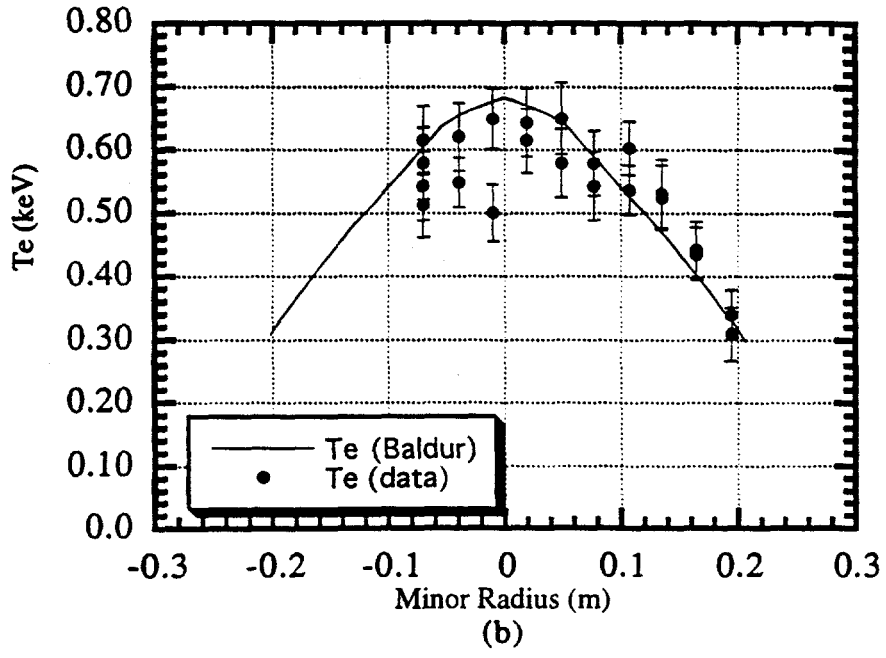

Fig. 7.9: (a) Electron density and (b) electron temperature as functions of minor radius compared with experimental data from ISX-B, shot 41119.

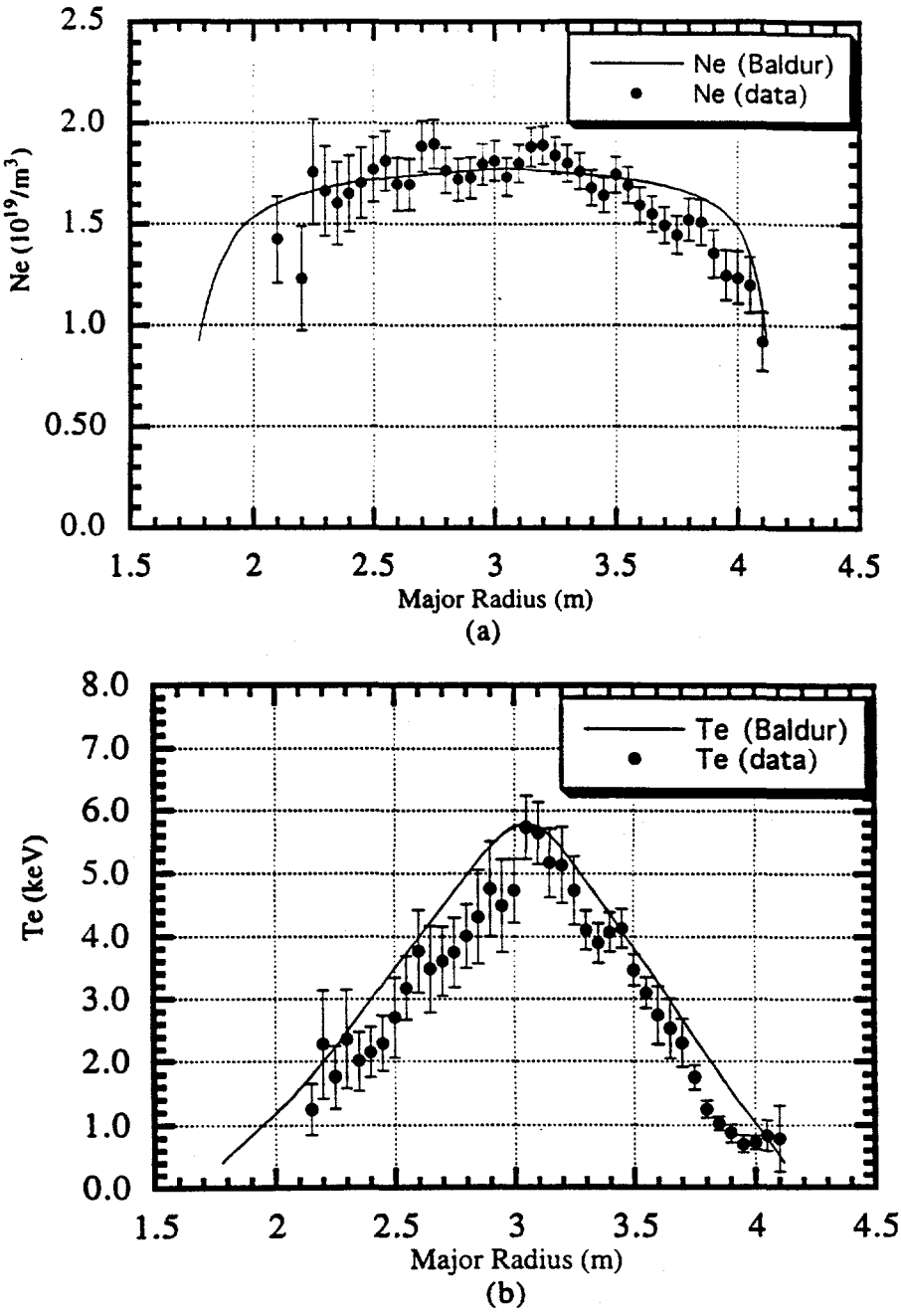

Fig. 7.10: (a) Electron density and (b) electron temperature as functions of minor radius compared with experimental data from JET, shot 27658.

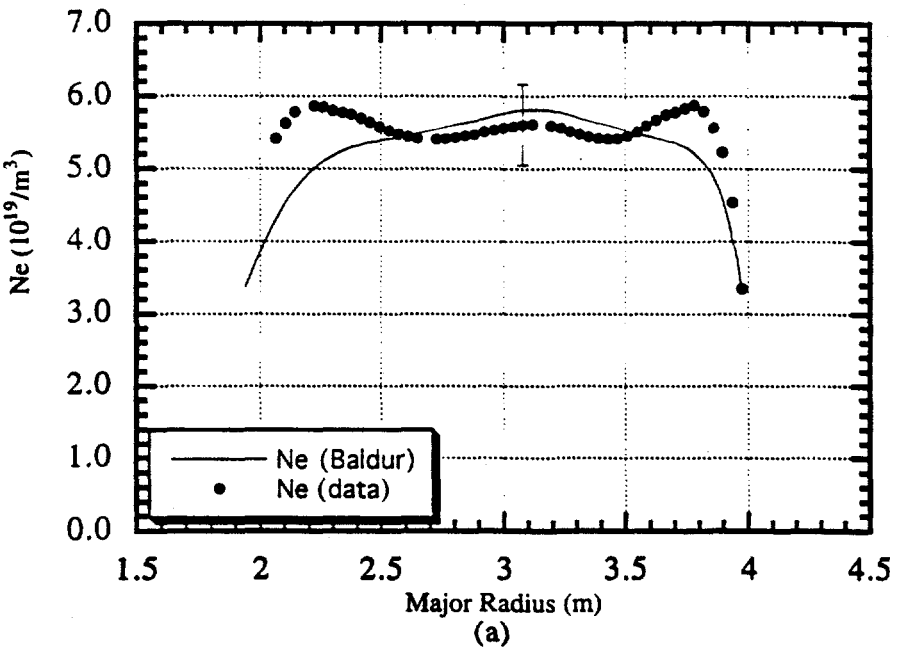

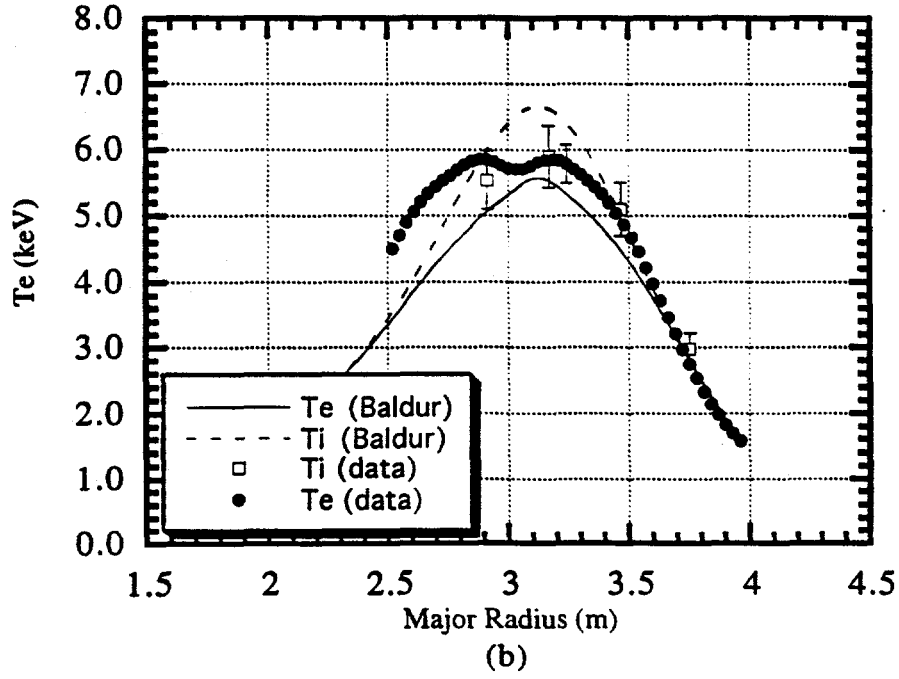

Fig. 7.11: (a) Electron density and (b) electron and ion temperature as functions of minor radius compared with experimental data from JET, shot 15894.

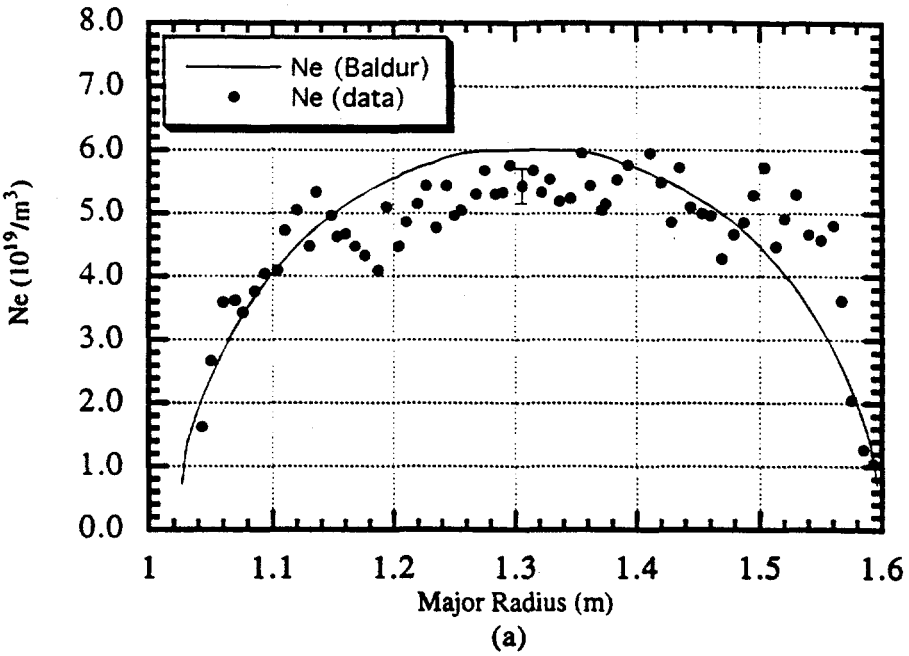

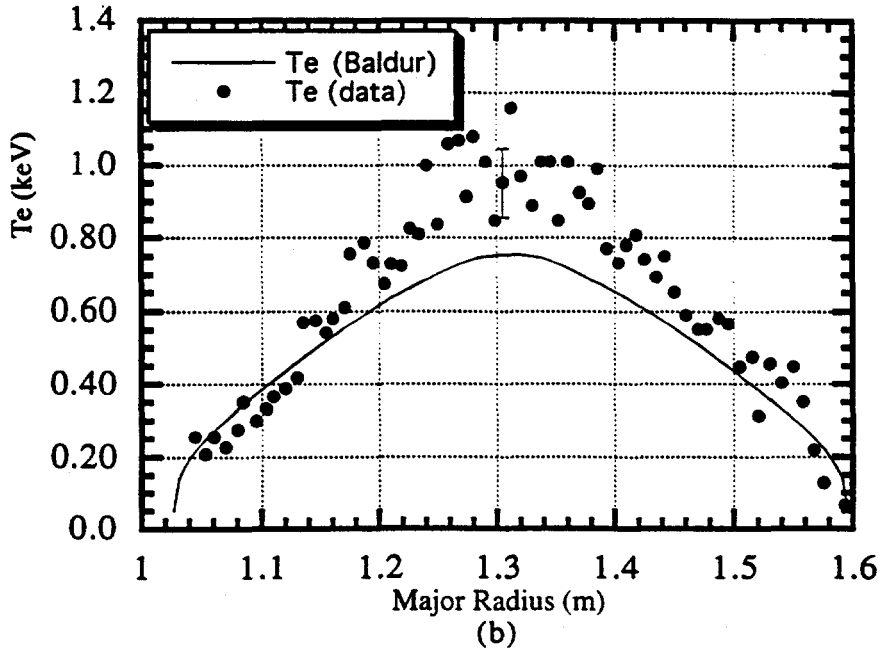

Fig. 7.12: (a) Electron density and (b) electron temperature as functions of minor radius compared with experimental data from JFT-2M, shot 73488.

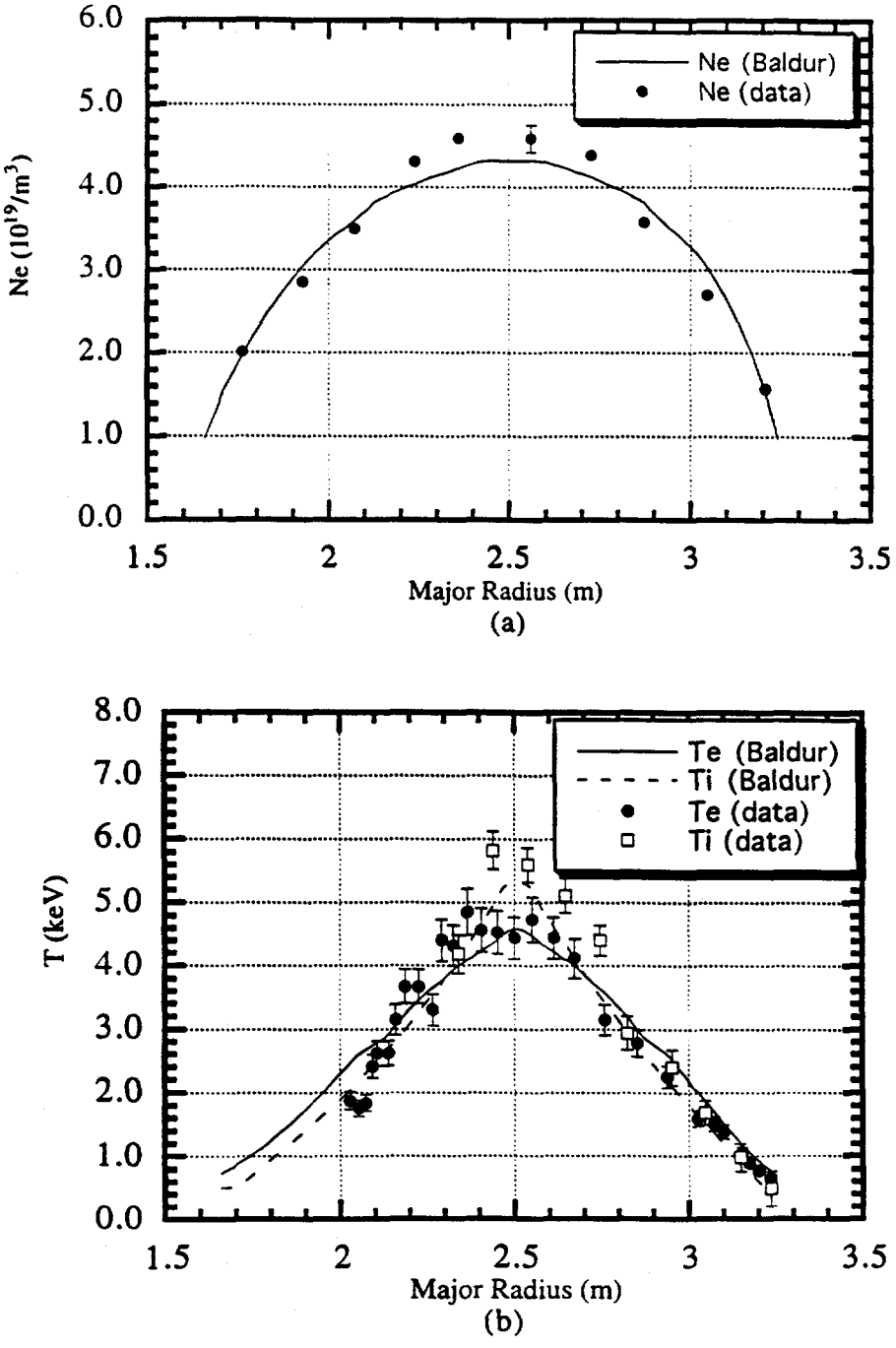

Fig. 7.13: (a) Electron density and (b) electron and ion temperature as functions of minor radius compared with experimental data from TFTR, shot 45980.

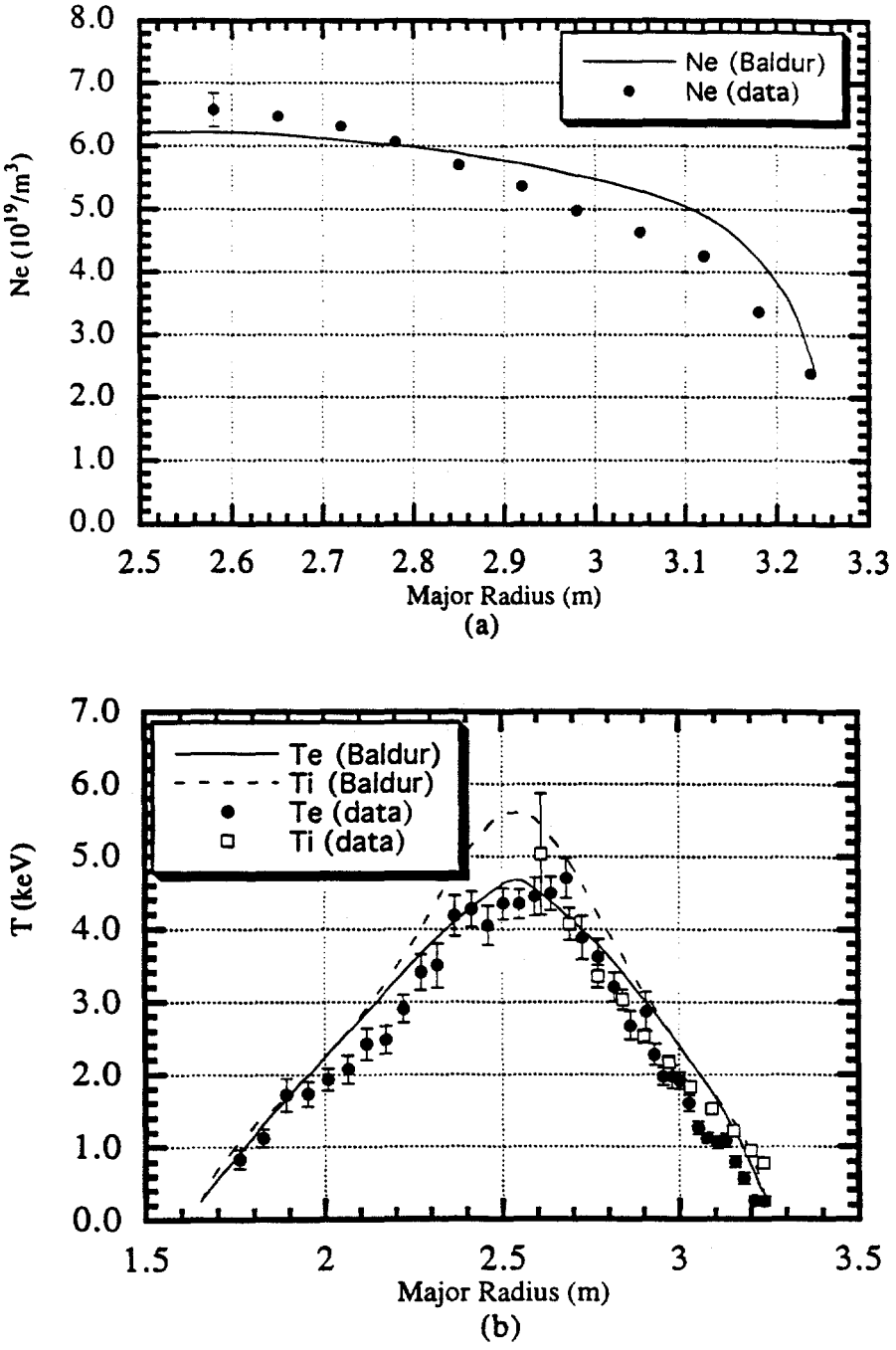

Fig. 7.14: (a) Electron density and (b) electron and ion temperature as functions of minor radius compared with experimental data from TFTR, shot 62248.

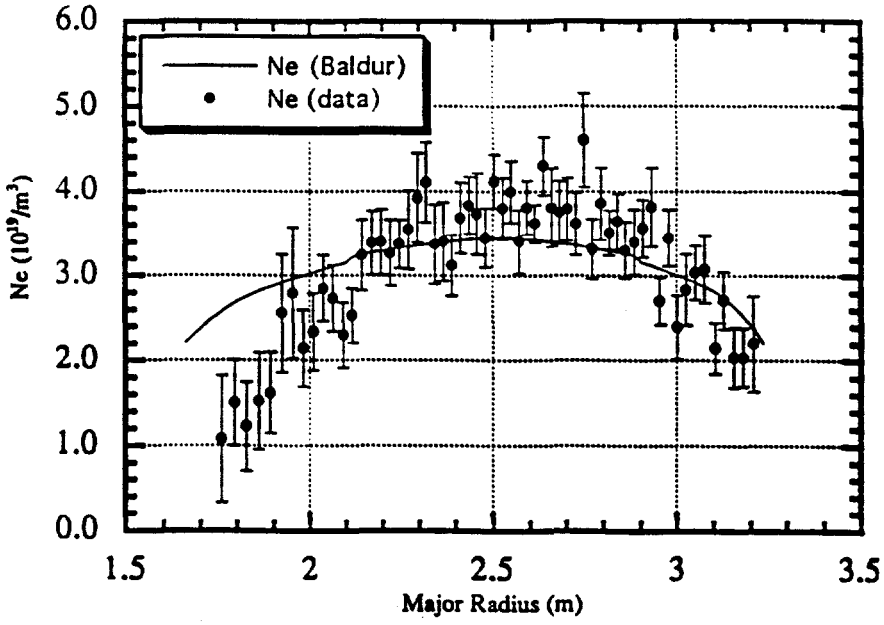

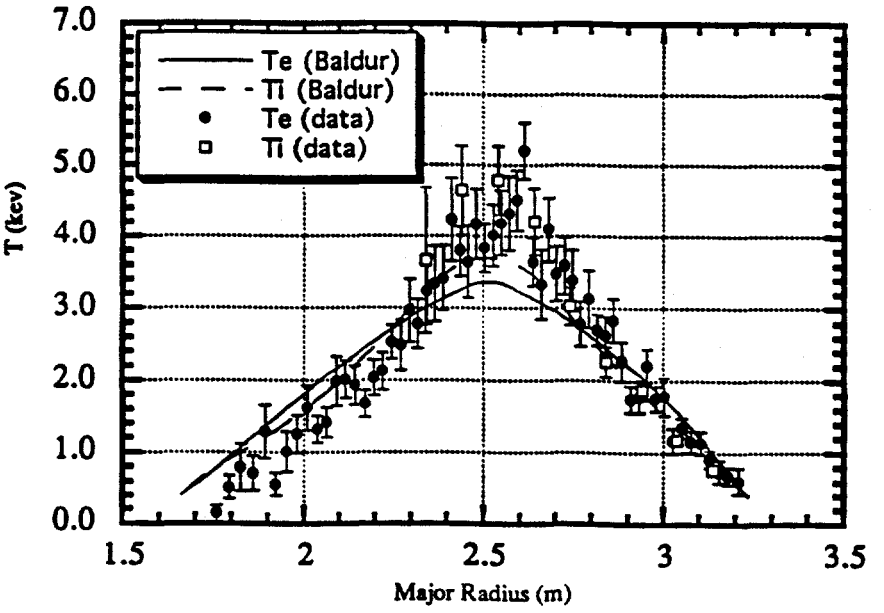

Fig. 7.15: Electron density and electron and ion temperature as functions of minor radius compared with experimental data from TFTR, shot 50904.

Chapter 8

Simulation of JT-60 Discharges with Calibrated Multi-mode Transport Model

The previous chapter gave a systematic calibration of a nominal multi-mode transport model. In this chapter, this experimentally calibrated theoretical transport model has been employed to study five $L-$mode discharges from the JT-60 tokamak. The transport model successfully reproduced electron temperature and ion temperature profile data. In the following sections, an introduction is given in Section 1; physical model is restated in Section 2; experimental data is presented in Section 3; transport analysis is given in Section 4; and summary is given in Section 5.

8.1 Introduction

A theory-based predictive tokamak transport model has been studied and applied to a variety of tokamak discharges simulations [61, 62, 60, 71]. This model includes nonlinear estimates of radial transport fluxes related to the drift wave and ballooning branches of the linear dispersion relation. Fluxes from these two branches of turbulence are linearly combined in the flux formulas to account for the anomalous transport in tokamak. Multipliers are assigned to two branches to represent two

turbulence saturation level calibrations. A systematic statistical method has been employed to calibrate the multipliers used here against 12 discharges from 7 different tokamaks to account for a wide range of operation conditions. The detailed calibration process was discussed in the last chapter. In this chapter, we apply this calibrated transport model to studying five $L-$mode discharges from the JT-60 tokamak [167]. Three discharges operated using a limiter; the other two operated using a divertor. Two limiter discharges have been analyzed by Shirai et al. using transport based on the drift wave branch [58]. That study was limited the ion temperature profiles which were reproduced using their model. In our study, both electron temperature (T_e) and ion temperature (T_i) profiles were successfully reproduced using theory-based model with global plasma parameters as inputs. In the theoretical model used here, the drift wave branch dominates the anomalous transport of plasma during neutral beam heating in the discharge simulation.

8.2 Multi-mode Transport Model

The multi-mode transport model used here is a theory-based transport model. The flux formulas used in this model include a linear combination of contributions from drift wave branch and ballooning branch to account for two primary anomalous turbulence in tokamaks. The drift wave branch consists of trapped particle effects including trapped electron (TEM) and ion temperature gradient (η_i) modes and circulating electron (CE) mode. A drift wave branch was employed in previous transport modeling to reproduce some experimental data [56, 57]. However, by itself, it has poor scaling of global energy confinement plasma current compared with empirical results [45, 63]. The strong dependence on temperature of its heat fluxes also gives overly steep predicted temperature gradients near a limiter. The ballooning branch includes effects from resistive (RB), kinetic (KB) ballooning and neoclassical (NM) MHD modes, which have been studied in a high β (kinetic pressure /magnetic pressure) tokamak [40, 103, 111, 115, 109]. The rationale for the multi-mode transport model has been explained elsewhere [61]. One multiplier each is assigned to the drift wave branch and ballooning branch fluxes. These multipliers represent

two turbulence saturation level calibrations. They were previously calibrated against a relatively broad database. A Bayesian probability method was employed there to optimize the multipliers. A normal distributed likelihood function was established including the calibration and/or model offset factor and "error bar" rescaling factor. Probability distribution appropriate to prior knowledge of the accuracy of theory, experiment and modeling methods were used for that calibration. The prior distributions of parameters were assumed. A posterior probability function of multipliers was obtained from Bayesian theorem. By maximizing the posterior probability function versus these two multipliers, we obtained 1.03 times the nominal drift wave branch theoretical fluxes and 0.50 times the nominal ballooning branch theoretical fluxes respectively. The 95% confidence intervals are [0.9, 1.2] for the first multiplier and [0.4, 0.6] for the second multiplier. The resulting anomalous fluxes are added to neoclassical transport and incorporated into a set of time-dependent, flux-surface-averaged particle and energy conservation equations. This set of equations with realistic source and sink terms is solved in the "one and half" dimensional transport code BALDUR. [138] The general form of fluxes used here can be written as

$$Q_e = -n_e[e^{c_1}(\chi_e^t + \chi_e^{CE}) + e^{c_2}(\chi_e^{RB} + \tilde{\chi}_e^{RB} + \chi_e^{NM} + \tilde{\chi}_e^{NM} + \chi_e^{KB})]\frac{\partial T_e}{\partial r} \quad (8.1)$$

$$Q_i = -n_i[e^{c_1}(\chi_i^t + \chi_i^{CE}) + e^{c_2}(\chi_i^{RB} + \chi_i^{NM} + \chi_i^{KB})]\frac{\partial T_i}{\partial r} \quad (8.2)$$

$$\Gamma_a = -[e^{c_1}(D_a^t + D_a^{CE}) + e^{c_2}(D_a^{RB} + D_a^{NM} + D_a^{KB})]\frac{\partial n_a}{\partial r} \quad (8.3)$$

Here $Q_{e,i}$ is the flux-surface-averaged radial fluxes of electron (subscript e) and ion (subscript i) energy and Γ_a of particle species type a. $\tilde{\chi}$ indicates the contributions from the electron motion along stochastic magnetic fields in the modes [103, 111]. The drift wave branch and ballooning branch multipliers e^{c_1} and e^{c_2} are 1.03 and 0.50 here respectively. The detailed expressions for the transport coefficients are given in the Appendix 1.

As the plasma gradients get flat near the magnetic axis, anomalous transport from drift wave and ballooning branches will vanish. Sawtooth oscillations are included here to reproduce occasional additional electron energy and density rear-

rangement near the center. This is done by interchanging the particle and energy around the $q = 1$, where q is safety factor, using Kadomtsev's model [168]. Only 10% of the poloidal flux is exchanged during each sawtooth crash, as suggested by a study of q profiles on Tokamak Fusion Test Reactor (TFTR) [169]. The sawtooth period and/or crash phasing are prescribed using what experimental data is available in order to obtain proper sawtooth phasing for temperature profiles.

The initial time of each simulation is taken well before the diagnostic time so that uncertainties about the initial state will not yield significant effects on simulations of diagnostic profiles. The initial temperature and density profiles are assumed to be parabolic in radius. As the transport model is not applicable near the scrapeoff layer, a radial boundary (r_λ) in the calculation is set $0.05/B_t$ inside the outmost closed flux surface, where B_t is toroidal magnetic field (all is SI units). The temporal boundary conditions of temperature and density can be calculated using the model of Singer et al. [71, 170]. with temporal current, line-averaged density and input power from experimental measurements. These time evolution data from one typical discharge (10643) are shown in Fig. 8.1.

The neutral transport is simulated using Monte Carlo algorithm by influxing enough neutral hydrogen isotopes at 0.04 kev to match the reported line or volume averaged electron density. The same technique is employed in calculation of higher energy neutral beam injection heating. Impurity radiation losses are treated by radiating 10% of the heating power, using a power per unit volume which increases linearly from zero at $r = 0$ to 0.9 r_λ and decreases linearly to zero at r_λ. The uncertainty in radiation will bring about some systematic errors in the transport modeling. Electron energy losses of 0.03 kev per electron ionization as well as ion energy losses due to charge exchange transport of neutral hydrogen isotopes are also included.

8.3 Experimental Data

Five L-mode discharges from $JT-60$ are studied in this chapter. This includes three limiter and two divertor discharges. The power changes from 5.17 MW to 11.7 MW using 65 KeV perpendicular neutral beam (NB) injection heating.

Hydrogen neutral beam injection into target hydrogen plasmas was utilized in these discharges. The primary plasma parameters from experimental data are given in Table 8.1. These are the major radius R_0, minor radius a, loop voltage V_l, toroidal field B_t, toroidal plasma current I_p, the effective charge Z_{eff}, the neutral injection power P_{NB}, atomic number A_i, neutral beam injection time t_{beam} and diagnostic time t_{diag}. Note that the Z_{eff} is appreciably lower in the divertor discharges, with a minimum at 1.25 versus a maximum at 3.72 in limiter discharges.

The diagnostic electron and ion temperature data were measured versus major radius, and then mapped to the flux surfaces computed in the equilibrium code and reduced to profile data as a function of mid-plane halfwidth [171]. The electron temperature profiles were from Thomson scattering measurement and also from electron cyclotron emission (ECE) measured by a Fourier transform spectrometer (FTS). The profiles of ion temperature were measured using a charge-exchange recombination measurement ($CXRS$) [172].

8.4 Transport Analysis

The multi-mode transport model described above was employed to study the five discharges described in the previous section. The temperature profiles from simulations along with experimental measurements are shown in Figs. 8.2-7. These profiles reasonably reproduce the experimental data. The center temperature profiles from measurements become flatter in five discharges. This suggests that it was not a long time from the last sawtooth crash to diagnostic measurement time [159]. The sawtooth collapse will generally cool the electron and ion in plasma center. The same feature can be seen in the simulation. The small bumps in the simulation curve comes from the sawtooth crashing which interchanges the poloidal flux around the $q = 1$ point. The slope discontinuity corresponds to the outmost mixing radius of the sawtooth crash. We can see that the simulated temperature profiles have around the same turning point as the measurement data. In two divertor discharges, the center ion temperature are higher than that of the electrons, but only by an amount comparable to the uncertainty indicated by quoted measurement error bars. In the

limiter discharges, the differences between the central electron and ion temperatures are relatively small. These differences can also be seen in the simulation results. There is slight upshift of simulated temperature profiles in the outer region. This discrepancy may be due to systematic error aspect of the simulations other than the turbulent transport flux formulas, such as impurity radiation, which as discussed by another author [71]. Alternatively, it could indicate too little peripheral energy transport in the calibrated model for these discharges. These simulations show that electrons and ions have the very similar temperature profiles in the outer region of plasma. We can also see this relationship in the experimental profiles.

Thermal diffusivities for electrons and ions from a typical discharge simulation are shown in Figs. 8.8a and 8.8b. The contributions from neoclassical transport and anomalous transport of drift wave and ballooning branches are separated in the figures. We can see that the dominant energy loss comes from the anomalous thermal transport in the drift wave branch. The thermal diffusivities are very small in the inner region. This is due to the relatively flat pressure gradient in the inner region, where the instabilities will not be strongly excited. The primary energy loss there is from the sawtooth instability. The peaks in the figures come from the finite radial grid point effects in the numerical algorithm to treat some physical processes, such as the switch in η_i mode in the model. This effect has been extensively investigated without any indication that it significantly affects the overall results [60, 70].

8.5 Summary

In this chapter, the experimentally calibrated transport model has been applied to the simulation of five $L-$mode discharges from JT-60. Even though this theory-based model was calibrated against deuterium discharges, it reasonably successfully reproduces the temperature profile data from global plasma parameters in these hydrogen plasma discharges. The temperature profiles are qualitatively predicted by the transport model, which is consistent with a previously reported empirical scaling [19]. Some deviations exist between the reported temperature profiles and simulation results. This may result from both the imperfection in the simulations,

such as the treatment of impurities radiation loss, and/or from diagnostic calibration variance and/or systematic calibration offsets. This may also arise from the uncertainty of the current transport multipliers or other inaccuracies in the transport model, as indicated by the size of confidence regions in the last chapter. However, the results given in the present chapter indicate that a promising theoretical tokamak transport model has been obtained.

Table 8.1 Discharge Parameters

Discharge	10619	10643	11220	11170	11206
Type	limiter	limiter	limiter	divertor	divertor
$R_0(m)$	3.00	3.02	3.00	2.91	2.92
$a(m)$	0.873	0.886	0.866	0.716	0.726
$V_l(v)$	0.427	0.481	0.582	0.357	0.253
$B_t(T)$	4.5	4.48	4.52	4.65	4.64
$I_p(MA)$	0.965	1.9	2.66	0.95	1.45
$n_e(10^{19}/m^3)$	1.67	3.93	6.51	3.44	4.37
A_i	1.0	1.0	1.0	1.0	1.0
Z_{eff}	3.49	3.72	2.49	1.69	1.25
P_{NB} (MW)	5.17	9.49	9.61	11.7	7.52
t_{beam} (secs)	3.08	6.53	5.05	3.03	5.52
t_{diag} (secs)	8.6	8.6	7.1	4.6	7.0

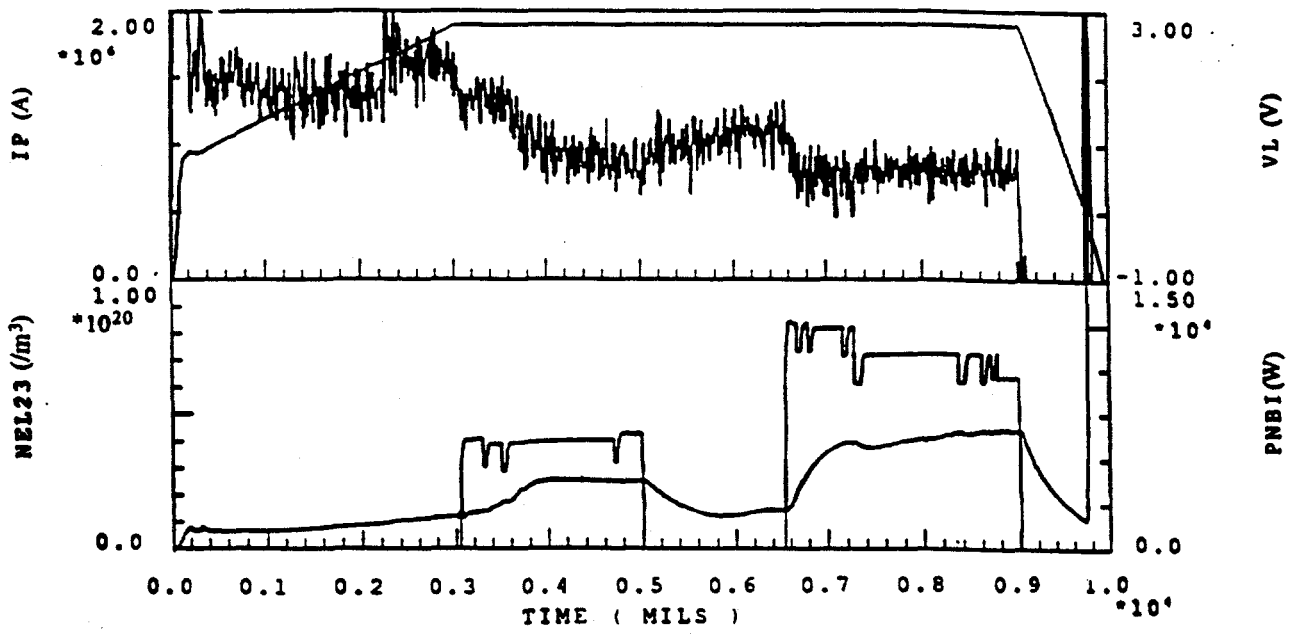

Fig. 8.1: Time dependent current (IP), loop voltage (VL), line-averaged density (NEL23) and neutral beam injection power (PNBI) from experimental measurements in JT-60 shot 10643.

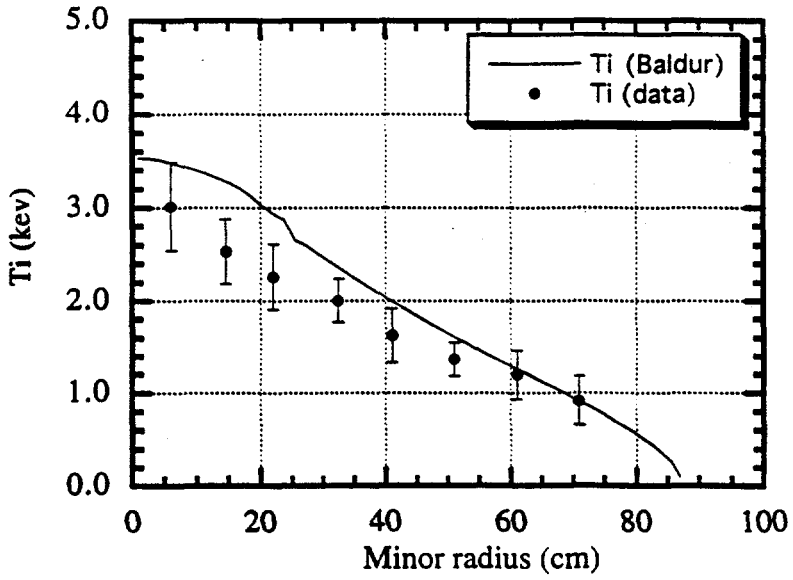

Fig. 8.2: Ion temperature profile from BALDUR
compared with experimental data shot JT-60 #10619 (t = 4.6s)

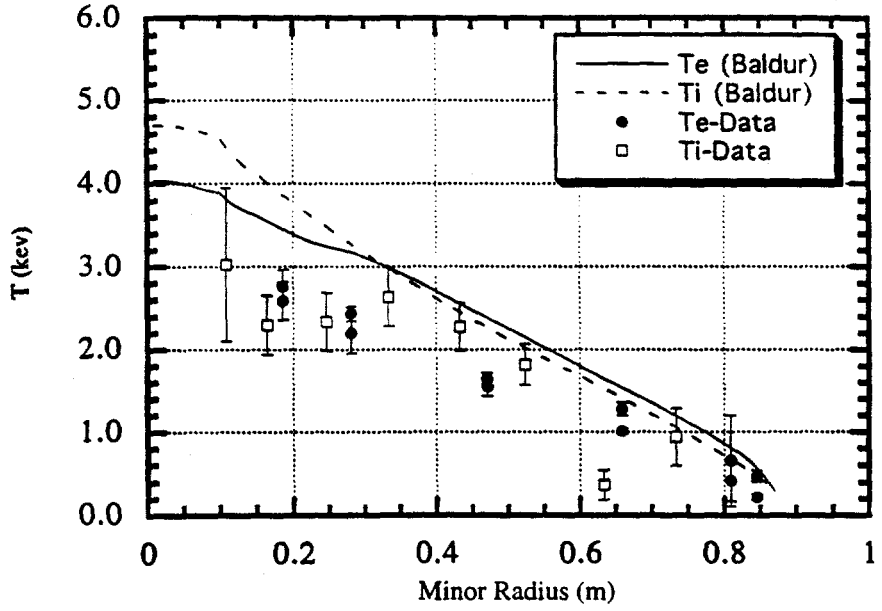

Fig. 8.3 Electron and ion temperature as a function of minor radiuscompared with experimental data from JT-60 limiter shot 10619.

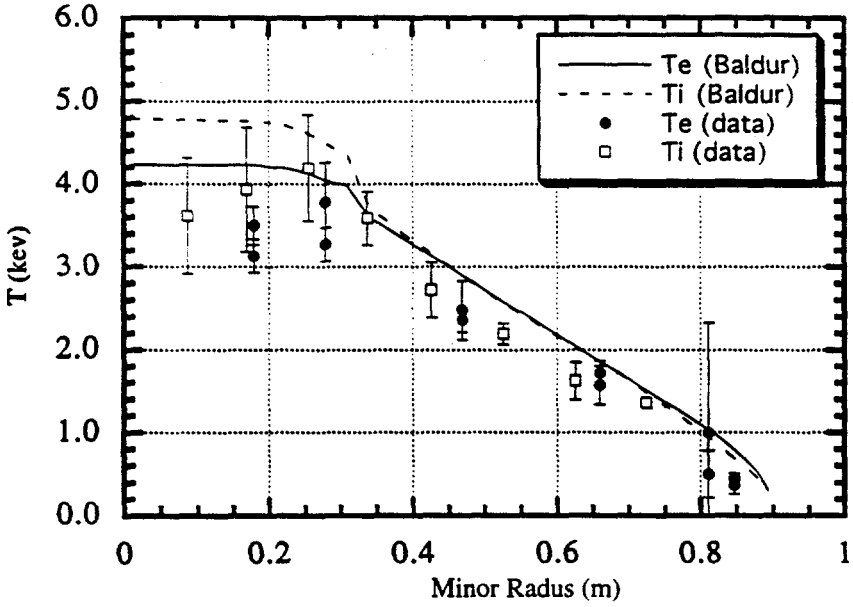

Fig. 8.4 Electron and ion temperature as a function of minor radius compared with experimental data from JT-60 limiter shot 10643.

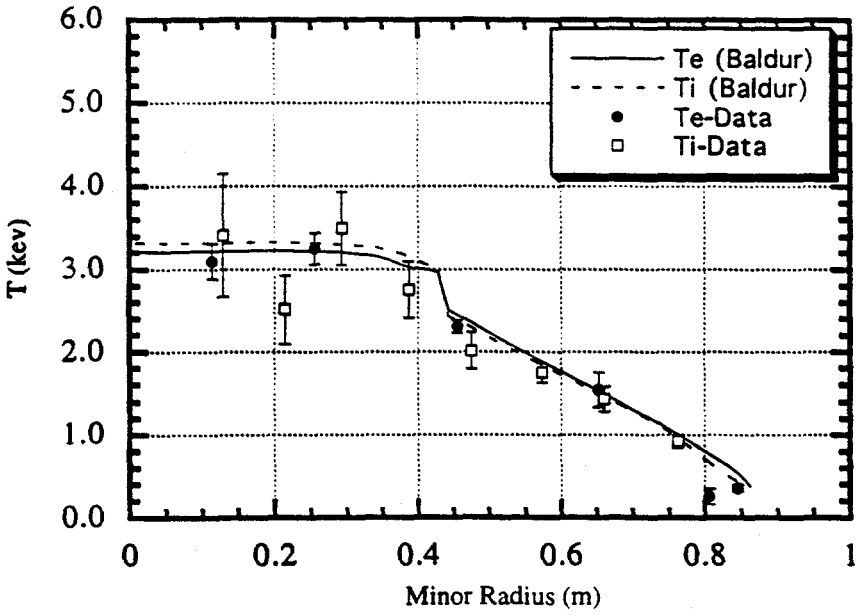

Fig. 8.5 Electron and ion temperature as a function of minor radius compared with experimental data from JT-60 limiter shot 11220.

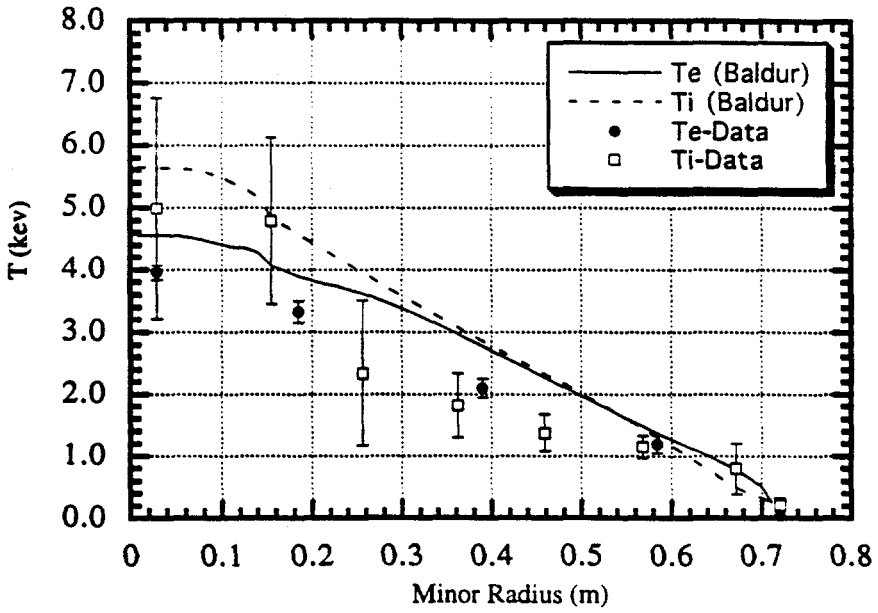

Fig. 8.6 Electron and ion temperature as a function of minor radius compared with experimental data from JT-60 divertor shot 11170.

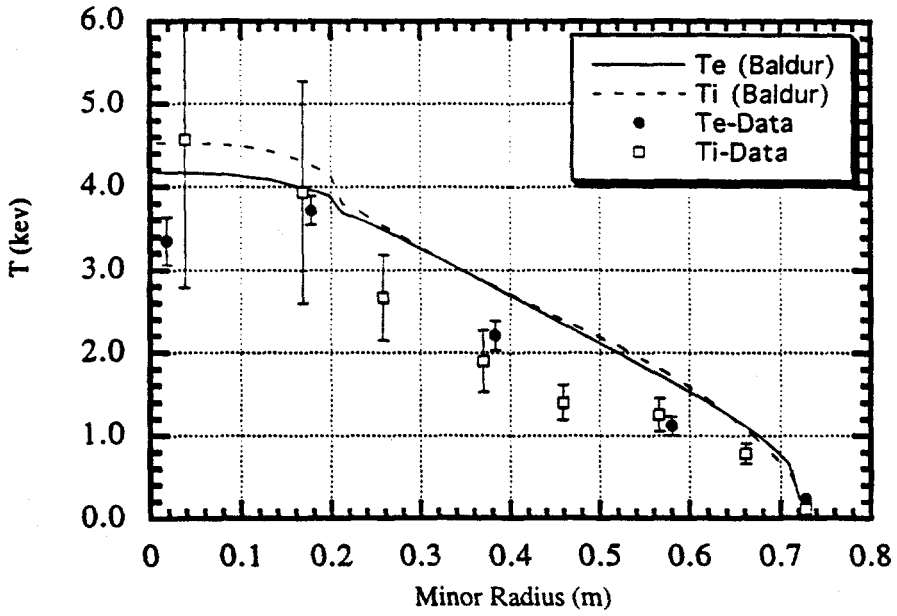

Fig. 8.7 Electron and ion temperature as a function of minor radius compared with experimental data from JT-60 divertor shot 11206.

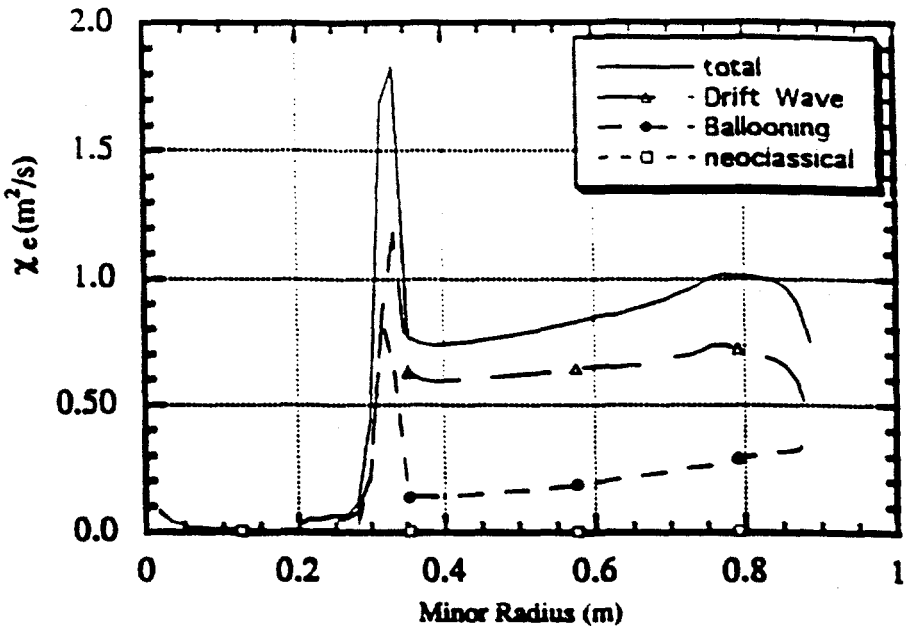

(a)

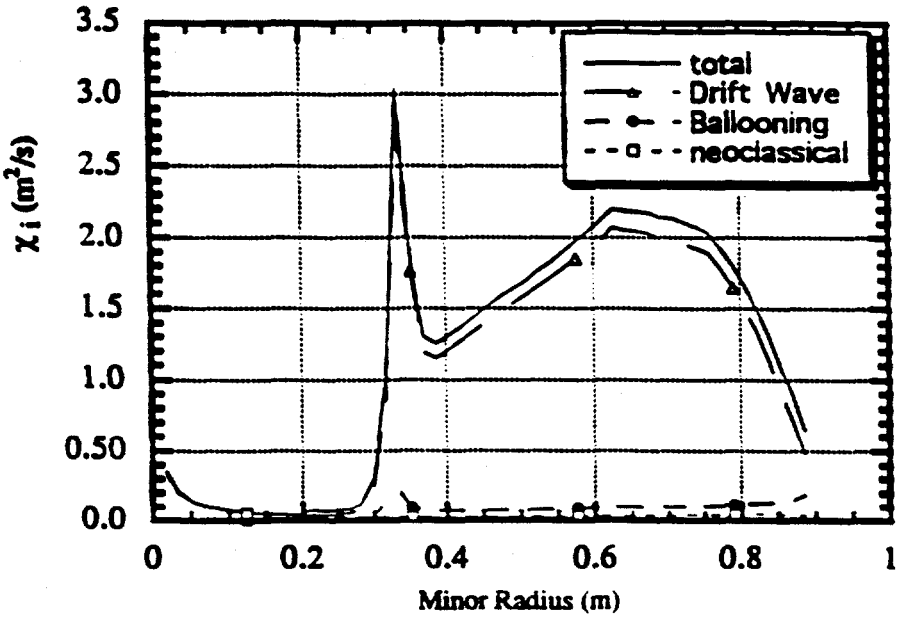

(b)

Fig. 8.8: (a) Electron and (b) ion thermal diffusivities from different contributions as a function of minor radius in JT-60 simulation 10643.

Chapter 9

Application of a Calibrated Tokamak Transport Model to ITER Ignition Studies

A theory-based tokamak transport model has been calibrated and tested against the experimental data in the preceding chapters. In this chapter, this model is applied to ITER ignition studies. The reference simulation of basic ITER Engineering Design Activity (EDA) parameters shows that a self sustained thermonuclear burn can be achieved provided that impurity control makes radiative losses sufficiently small. The ignition probabilities of both ITER EDA and Conceptual Design Activity (CDA) parameters are investigated. These results suggest that a high energy auxiliary heating power significantly less than 100 MW should heat ITER EDA to ignition.

In the following sections: an introduction is given in Section 1; the physical model is described in Section 2; a reference simulation is given is Section 3; probability of ignition is studied in Section 4; and summary is given in Section 5.

9.1 Introduction

Recently, a number of different transport models have been used in the ITER design study [173, 174, 175, 176, 177, 178]. These models employed a "one and

one half" dimensional transport code to solve a full set of time dependent transport equations for plasma profiles. Such results can assist in choosing the design point in parameter space and investigating profile control. Most of these transport models employed empirical or semi-empirical radial flux transport formulas with prescribed constants.

In this chapter, we employ a comprehensive calibrated theory-based radial transport model to investigate start-up and ignition burn in ITER. This model has been studied and optimized over the past several years by several authors [61, 62, 60, 71]. It includes a linear combination of contributions from two different branches of the linear dispersion relation in the radial anomalous transport formulas with two experimentally calibrated constants. The application of the calibrated transport model to basic ITER EDA parameters shows that a self sustained thermonuclear burn with around 1.5 GW fusion power can be achieved using 50.0 MW auxiliary heating power and $1.2 \times 10^{20}/m^3$ volume averaged electron density provided that impurity control makes radiative losses sufficiently small. The probability of ignition is investigated for both ITER EDA and CDA parameters. The results show that an auxiliary heating power significantly lower than 100 MW can be used to heat ITER EDA parameters to ignition.

9.2 Physical Model

The theory-based model used here is called "multi-mode" transport model. This model combines a linear summation of nonlinear estimates of contributions from drift wave and ballooning branch instabilities to account for the anomalous transport. The drift wave branch includes trapped electron, ion temperature gradient and circulating electron effects. The ballooning branch includes effects addressed by resistive, kinetic ballooning and neoclassical MHD treatments. The resulting anomalous fluxes are added to neoclassical transport and incorporated into a set of time-dependent, flux-surface-averaged particle and energy conservation equations. This set of equations with realistic source and sink terms is solved in the "one and one half dimensional" transport code BALDUR [138]. The general form of fluxes used here can be

written as

$$Q_e = -n_e\{e^{c_1}(\chi_e^t + \chi_e^{CE}) + e^{c_2}(\chi_e^{RB} + \tilde{\chi}_e^{RB} + \chi_e^{NM} + \tilde{\chi}_e^{NM} + \chi_e^{KB})\}\frac{\partial T_e}{\partial r} \quad (9.1)$$

$$Q_i = -n_i\{e^{c_1}(\chi_i^t + \chi_i^{CE}) + e^{c_2}(\chi_i^{RB} + \chi_i^{NM} + \chi_i^{KB})\}\frac{\partial T_i}{\partial r} \quad (9.2)$$

$$\Gamma_a = -\{e^{c_1}(D_a^t + D_a^{CE}) + e^{c_2}(D_a^{RB} + D_a^{NM} + D_a^{KB})\}\frac{\partial n_a}{\partial r} \quad (9.3)$$

Here $Q_{e,i}$ specifies the flux-surface-averaged radial fluxes of electron (subscript e) and ion (subscript i) energy and Γ_a of particle species type a. $\tilde{\chi}$ denotes the contribution from electron motion along stochastic magnetic fields. Detailed expressions for these transport coefficients given in Appendix 1 are the same as those used in Chapter 7 except for a change of parameter denoted in that reference, c_{23}. This parameter controls a reduction of particle transport that occurs in the limit of low collisionality and high η_i. This slight change was motivated by a re-examination of the theory, checked against the experimental data, and found to have no clear impact on the goodness of fit. The drift wave branch and ballooning branch multipliers e^{c_1} and e^{c_2} represent two turbulence saturation level calibrations. They were previously calibrated against a relatively broad database including $L-$ mode and $H-$ mode discharges. A Bayesian probability method was employed there to optimize the multipliers. The method used allowed for calibration and/or model offset factors and "error bar" rescaling factors. A posterior probability function of c_1 and c_2 was obtained from Bayes' theorem. By maximizing the posterior probability function versus these two multipliers, we obtained 1.03 times the nominal drift wave branch theoretical fluxes and 0.50 times the nominal ballooning branch theoretical fluxes, respectively, with corresponding confidence regions shown in Fig. 7.1. These anomalous transport fluxes are added to neoclassical flux and incorported into the following flux-surface-averaged tranport equations

$$\frac{1}{V'}\frac{\partial}{\partial t}(n_a V') + \frac{1}{V'}\frac{\partial}{\partial \rho}(\Gamma_a V') = S_a \quad (9.4)$$

$$\frac{1}{V'^{5/3}}\frac{\partial}{\partial t}(E_j V'^{5/3}) + \frac{1}{V'}\frac{\partial}{\partial \rho}(V' Q_j) = S_j \quad (9.5)$$

$$\frac{\partial B_\theta}{\partial t} = -\frac{\partial}{\partial \rho}\left[\frac{\eta_{||}}{FR_0 < R^{-2} >}\frac{2\pi R_0}{\mu_0}\frac{F^2}{V'}\frac{\partial}{\partial \rho}\left(\frac{V' B_\theta}{F}\left\langle\frac{|\nabla\rho|^2}{R^2}\right\rangle\right) + \frac{\eta_{||}}{FR_0 < R^{-2} >} < \mathbf{J}\cdot\mathbf{B} >_{ext}\right] \quad (9.6)$$

Here, the first equation is particle conservation equation, the second equation is energy conservation equation, and the third equation is poloidal magnetic field diffusion equation. This group of tranport equations is differenced using conservative Crank-Niclson method with an adjustable implicit parameter. The time centering of tranport coefficients and source terms is accomplished using predictor-corrector scheme.

The MHD equilibrium code VMOMS is employed here to solve the two dimensional Grad-Shafranov equation with given pressure and current profiles at fixed boundary condition [179] (hence the designation, "one and one-half dimensional") using a moment expansion method. The effective surface area $V'(\rho)$ and various geometric factors are obtained. The plasma density and temperatures are then readjusted adiabatically, and the toroidal current $I(\rho)$ is readjusted by keeping the safety factor fixed. Next, tranport calculations are carried out for one or more timesteps holding V' and the geometric factors fixed. The resulting pressure and current profiles are used for the calculation of a new equilibrium.

Initial temperature and density profiles are assumed to be parabolic in radius. The boundary conditions used here are from an empirical study of the $L-$ and $H-$ mode discharges considering particle and energy transport at the edge of plasma [170]. As the transport model used here is not applicable near the scrapeoff layer, the radial boundary (r_λ) in the calculation is set to $\lambda = 0.05/B_t$ inside the outmost closed flux surface, where B_t is toroidal magnetic field (all in SI units). The boundary density follows

$$n_\lambda = n_b B(-1.0 + \sqrt{1.0 + (\frac{< n >}{n_b B})^2}) \quad (9.7)$$

where B is toroidal magnetic field, $< n >$ is the volume-averaged electron density and $n_b = 2.06 \times 10^{19} m^{-3} tesla^{-1}$ is constant which is calibrated by a least square fit to the data given in Chapter 7.

The boundary temperature below the ideal MHD pressure limits is obtained

by solving

$$(\frac{T_\lambda}{T_*})^2 - \frac{T_*}{T_\lambda} = h\frac{\lambda}{a} + (\frac{T_s}{T_*})^2 - \frac{T_*}{T_s} \tag{9.8}$$

where

$$h = c_0(R_0/a)^{2.2}\kappa^{-0.4}I_{MA}^{0.8}P_{MW} \tag{9.9}$$

In above equations, a is the minor radius, R_0 is the major radius, κ is the elongation, I is the toroidal current and P is the outflow power across the boundary. The constant $T_s = 0.07keV$ is taken from previous studies, and the present results are not expected to be sensitive to this choice. T_* and c_0 are calibrated using the least squares method with boundary data from the same data set that we used to calibrate the transport model. Here, we obtain $T_* = 0.61keV$ and $c_0 = 4.54$. An initial prescribed boundary temperature is used as the first step of simulation. The resulting outflow power is employed to calculate the new boundary temperature. This procedure is repeated three times to attain convergence for the reference transport model, and the resulting boundary conditions are used for all the simulations discussed here. Both empirically and theoretically, we do not expect that $\beta' = d\beta/dr$ at our boundary location, r_λ, is larger than the first ideal MHD β limit, where β is the ratio of kinetic pressure to magnetic pressure. Approximately, that is, $-\beta' \leq 0.6\hat{s}/(q^2R_0)$, where $\hat{s}$ is the dimensionless magnetic shear and q is the safety factor. From this relation, with given density at r_λ, we have the limited boundary temperature T_λ^β. Hence, the boundary temperature used here is $\min\{T_\lambda^{model}, T_\lambda^\beta\}$.

Neutral transport is simulated using a Monte Carlo algorithm by influxing enough neutral hydrogen isotopes at 0.04 keV to match the volume averaged electron density. Operations designed to approximate equal fractions of deuterium and tritium using boundary density and recycling, and 1% of beryllium concentrations are assumed for our reference simulation. The helium concentration is around 10% with 95% of helium crossing the boundary location returning as neutrals with energy 0.04 keV. The α particle heating in fusion is computed using a local plasma heating model [138].

Radiation losses from bremsstrahlung, line, recombination and synchrotron radiation are evaluated in the coronal equilibrium using the radiation tables of Post et al. [180]. More radiation can come from the non-equilibrium impurity radiation as described by Stotler [181]; but we have inadequate information on neutral recycling to accurately model the charge-exchange recombination contribution to this effect, which in any case is expected to be rather modest for the low-Z dominated plasma assumed here. Electron energy losses of 0.03 keV per hydrogen ionization as well as ion energy losses due to charge exchange transport of neutral hydrogen isotopes are also included.

Sawtooth activity is also simulated in the study. This is done by interchanging the particle and energy around the $q = 1$, using Kadomtsev's model [168]. Only 10% of the poloidal fluxes are exchanged during each sawtooth crash as suggested by a study of q profiles on Tokamak Fusion Test Reactor (TFTR) [169]. The Park-Montecillo model for the sawtooth period [182], $\tau_{saw} \propto R_0^2(T_{e0})^{3/2}/Z_{eff}$, is employed and calibrated against one JET H-mode discharge (15894) sawtooth period [71]. Here, T_{e0} is the central electron temperature and Z_{eff} is the effective charge. The result of this calibration (in SI units except with T_{e0} in keV) is $\tau_{saw} = 0.01R_0^2(T_{e0})^{3/2}/Z_{eff}$.

We start the simulation by growing the ITER plasma in the vacuum vessel from the conditions available in an existing present JET experiment, except for larger major radius and higher toroidal field in ITER. Growing the plasma size during the build-up of current can overcome the potential skin current problem, which might otherwise induce disruptions during the stage of start-up [183]. The safety factor at edge is kept approximately constant during the growth of plasma and build-up of current in order to obtain predictable current profiles. The plasma density ramp up during the Ohmic heating stage is chosen to remain to close Greenwald's limit [184], defined by

$$\overline{n}_{Greenwald} = 10^{20} I/(\pi a^2) \tag{9.10}$$

This will help to reduce the shine through loss in the latter phase of auxiliary heating.

The neutral beam injection is used as an auxiliary heating with 50 MW power and 1.0 MeV energy. This follows the suggestion of the ITER Joint Central

Team for achieving a self-sustained thermonuclear burn [185]. It is assumed that this can be obtained by neutralization of negative deuterium ions. The central tangent radius of beam is assumed to be halfway between the vacuum field magnetic axis and our inner plasma boundary for effectively heating the plasma at relatively low density and contributing to current drive.

The basic plasma parameters for the ITER EDA and CDA studies are listed in Table 9.1 [185, 186]. Here, the δ is the triangularity at our boundary location, and the other parameters are the same as previously defined.

9.3 Reference Simulation

For a reference simulation, we apply the transport model to the study of an ITER EDA case with volume-averaged electron density $< n_e >= 1.2 \times 10^{20}/m^3$. The main results from the simulation are shown in Figs. 9.1 - 7. The time evolution of fusion power and β are given in Fig. 9.1 and 9.2. We can see that a self-sustained quasi-steady state thermonuclear burn has been achieved. The total fusion power from thermonuclear reactions is about 1.5 GW, which meets the design goal of ITER team. The total β is around 3.0%, which is lower than Troyon's limit, 3.5%, ($\beta_{troyon} = 2.5I(MA)/(a(m)B(Tesla))$) from MHD instability studies [187].

No evidence is seen of a runaway thermal instability, presumably because of the enhanced loss at higher β in the anomalous transport model. The periodic fluctuation of β results from the periodic activity of sawteeth. Fig. 9.3 shows the time dependent heating power and loss power. The heating power is well balanced by the loss power during the quasi-steady state burn. The heating power includes Ohmic heating, neutral beam injection heating and α particle heating. The loss power consists of the conduction and convection from electrons and ions towards the wall, electron-driven radiation, ion recombination and charge exchange losses. The plasma heating can be divided into three stages. The first stage is from 10 to 90 s. Only Ohmic heating is used during this period. The use of such a long Ohmic heating phase is a computational convenience (and possibly an experimental one for such a large machine), but is not expected to be essential to our conclusions. The α particle

heating at this time is negligible because there is little thermonuclear reaction. The second stage starts from 90 to 150 s. A total 50 MW neutral beam injection is employed as an auxiliary heating to heat the plasma to higher temperature between 90 s to 150 s in our reference simulation. The rapid increasing of plasma temperature enhances the thermonuclear reaction, which results in total heating power rising to above 400 MW. The third stage begins when the neutral beam injection power is turned off at 150 s. The total heating power falls down quickly. The α particle heats the plasma to balance the losses.

The time development of the electron density profile is given in Fig. 9.4. The fuel ion density profile with a similar shape is given in Fig. 9.5. The ratio of fuel ion density to electron density is about 0.86 in quasi-steady state. The appreciable differences between electron and ion density are due to the accumulation of helium from nuclear reaction, which is given in Fig. 9.6. The flat density profile helps to reduce pressure-gradient-driven anomalous transport for a given temperature profile. The line-averaged electron density is above the Greenwald limit which is around $0.8 \times 10^{20}/m^3$ during the burn phase. The Greenwald limit is an observational density limit that can be exceeded using pellet injection [188], which might be necessary for density evolution of the type illustrated here if the power in ITER does not otherwise allow such plasma densities. Fig. 9.7 and 9.8 show the time evolution of electron and ion temperature profiles. It can be seen that electrons and ions have around the same temperature, and that the central temperature of ions is only slightly higher than that of the electrons. Bremsstrahlung radiation profile given in Fig. 9.9 is a noticeable electron energy loss in the center of these high temperature and low central transport rate plasmas. The time dependent profile of safety factor, q, is plotted in Fig. 9.10. The central safety factor $q(0)$ is less than 1.0, which causes the sawteeth. The edge safety factor $q(a)$ is around 3.0. This should keep the plasma away from the $m = 2, n = 1$ tearing mode, which is believed to cause the disruption in tokamak. The radial location of $q = 1.0$ is around one half of the minor radius at the boundary. This brings about a relatively large heat pulse in the radial direction after sawteeth, which is reflected from the substantial central temperature drops after each sawtooth event.

The thermal energy at 300 s is about 1.25 GJ. The global energy confinement time is $\tau_E = 3.80\ s$. The H factor is about 2.0, where $H = \tau_E/\tau_{ITER89-P}$ and

$$\tau_{ITER89-P} = 0.048 I_{MA}^{0.85} R_0^{1.2} a^{0.3} n_{20}^{0.1} B^{0.2} (A_i \kappa / P)^{0.5} \tag{9.11}$$

with $A_i = 2.5$, $n_{20} = 1.2$ and the other parameters as listed in Table 9.1. Note that this is partly a consequence of centrally peaked α particle heating, as the contribution of about 1 keV boundary temperature pedestal is modest in this case.

9.4 Ignition Probability for ITER

In the Chapter 7, confidence regions were derived to account for the uncertainties in the theoretical transport model. The posterior probability density function for the two multipliers c_1 and c_2 with the given data Y used in that study is

$$p(c_1, c_2|Y) = 0.247 \exp\{-1/2(\vec{c} - \vec{c}_*)^t V^{-1} (\vec{c} - \vec{c}_*)\} \tag{9.12}$$

where, subscript t denotes transpose, the covariance matrix V is given by

$$V^{-1} = \begin{pmatrix} 354.58 & 621.08 \\ 621.08 & 193.75 \end{pmatrix} \tag{9.13}$$

and $\vec{c}_* = (0.0298, -0.6879)^t$. This probability density is a bivariate normal fitting to a large number of data points, and it is not expected to be particularly accurate except in the neighborhood of the fitted maximum likelihood point, $\vec{c}_*$. In particular, integrals over this distribution giving values $\geq 90\%$ should be viewed as purely "nominal" estimates. The cumulative ignition probability can be obtained by using the above probability density function and the marginal ignition function, $c_2 = f(c_1)$, in c_1, c_2 space.

$$Pr_{ignition} = \int_{-\infty}^{\infty} \int_{-\infty}^{f(c_1)} p(c_1, c_2|Y) dc_1\, dc_2 \tag{9.14}$$

In this equation, $c_2 = f(c_1)$ comes from the least squares fitting of marginal ignition point c_1, c_2. Operationally, here we define a discharge with β higher than 1.0% at 150 s after the end of auxiliary heating as ignited. The ignition probabilities for several

different cases have been investigated using basic parameter set in Table 9.1. These cases are listed in Table 9.2.

The first case is the reference simulation we just discussed before. The impurity beryllium concentration is set to 2.0% in the second case. In the third case, the total current is reduced to 20.0 MA. In the fourth case, the volume-averaged density of electron is lowered to $1.0 \times 10^{20}/m^3$. A total 40.0 MW of neutral beam injection power is used in the fifth case. The last case is from ITER CDA parameters with $< n_e >= 1.2 \times 10^{20}/m^3$ and 1.0% of beryllium impurity. The corresponding marginal ignition functions $f(c_1)$ for these cases and the posterior confidence region from Eq. 9.9 are given in Fig. 9.11. The cumulative ignition probability is the integral over the possible operating regime $c_2 \leq f(c_1)$ weighted by the probability density in Eq. 9.11. The ignition probabilities for these six cases are obtained and given in Table 9.2. Comparing cases 1 and 2, we find significant effects on ITER ignition from less effective impurity control. The probability of ignition falls sharply from 99.9% to 88.8% when the Be concentration rises from 1.0% to 2.0%. The discharge cools dramatically when too much energy is radiated from the plasma by impurities. Also, changing the current from 24.0 MA to 20.0 MA leads to a significant decrease of ignition probability in case 3. This is because of the degradation of confinement at lower current. In Fig. 9.11, the relatively smaller $< n_e >$ of case 4 gives a somewhat larger ignition probability than the reference simulation case. This may result in part from the higher boundary temperature for the lower density with the same first β limit, which reduces the outflowing heat losses, or the lower impurity and helium ash which cause lower radiation losses. The auxiliary power of the reference simulation decreases by 10.0 MW in the fifth case. There is no appreciable difference in the ignition probability. In Section 3, we have seen that the plasma is overheated during neutral beam injection. Therefore, the probability of ignition is primarily determined by the confinement after turning off auxiliary heating. For the ITER CDA case, the probability of ignition is much smaller than that of the ITER EDA case. Important design parameters in the CDA case are smaller than in the EDA case. This results in a poorer confinement than the EDA parameters. The EDA parameters used here are meant to be a conservative design. The ignition probability analysis gives high

confidence for ignition in the present context, assuming adequate impurity control. However, the EDA case is more expensive to build. The CDA parameters give less confidence of ignition, but they are closer to what may be realistically achievable.

9.5 Summary

Above studies suggest that a lower auxiliary power can be used to heat the ITER EDA parameters to ignition. Adequate confinement is of critical importance in achieving a self-sustained thermonuclear burn. Adequate impurity control is necessary to avoid cooling the plasma through radiation. Reduction of ignition probability with the reduction of machine size has been illustrated here. To achieve ignition in a smaller tokamak, greater emphasis needs to be placed on the optimization of parameters to improve the ignition probability.

While the ignition probabilities summarized in Table 9.2 are quite encouraging, it should be kept in mind that good helium pumping is assumed, only the two dominant a priori uncertain parameters in the theory models are varied to obtain confidence contours for this study, and the posterior confidence contours are fit with a bivariate normal approximation that is unlikely to be very accurate at the extremes, particularly, outside the 10% - 90% confidence range. The largest ignition probability obtained here is thus expected to represent an upper bound estimation for ITER ignition. They could be be overly optimistic if we consider more physical uncertainties, such as effects of operating over the Greenwald density, potential difficulties in obtaining an $L-$ to $H-$ mode transition and use of less than the fully informative limit for other theory model parameters. It should be understood that in a more complete study, performance probabilities well outside the 10% - 90% range can be expected to tend towards more moderate values.

Table 9.1 Basic ITER Parameters

Parameter	EDA	CDA
R_0 (m)	8.1	6.0
a (m)	3.0	2.15
κ	1.55	1.98
δ	0.22	0.38
I(MA)	24.0	22.0
B_t (T)	5.7	4.85

Table 9.2 Ignition Probabilities under Different Cases

case	1	2	3	4	5	6
type	EDA	EDA	EDA	EDA	EDA	CDA
$P_{aux}(MW)$	50.0	50.0	50.0	50.0	40.0	50.0
$< n_e > (10^{20}/m^3)$	1.2	1.2	1.2	1.0	1.2	1.2
$I(MA)$	24.0	24.0	20.0	24.0	24.0	22.0
$Be(\%)$	1.0	2.0	1.0	1.0	1.0	1.0
$Pr_{ignition}\%$	99.9	88.8	0.2	99.9	99.9	62.6

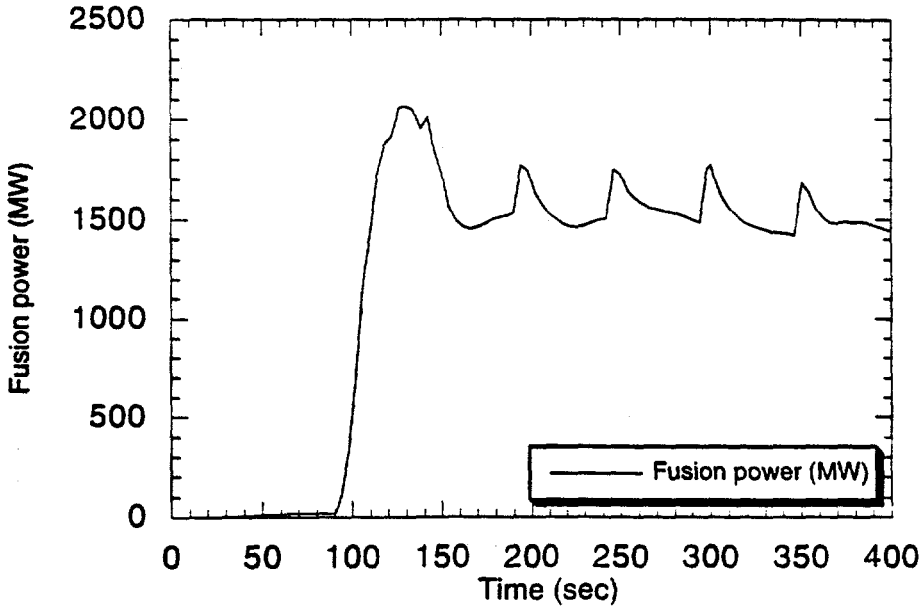

Fig. 9.1: Thermonuclear fusion power as a function of time in the ITER reference simulation.

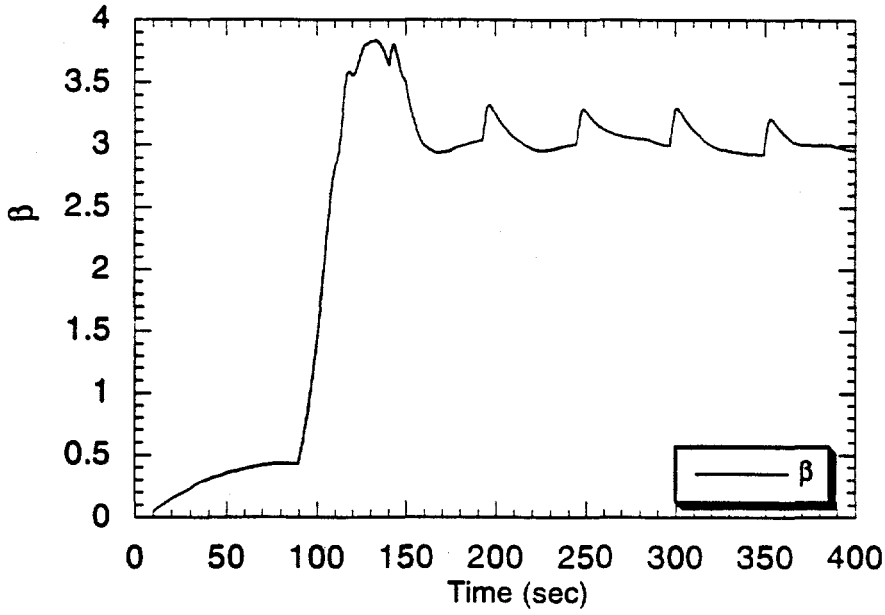

Fig. 9.2: Beta as a function of time in the ITER reference simulation.

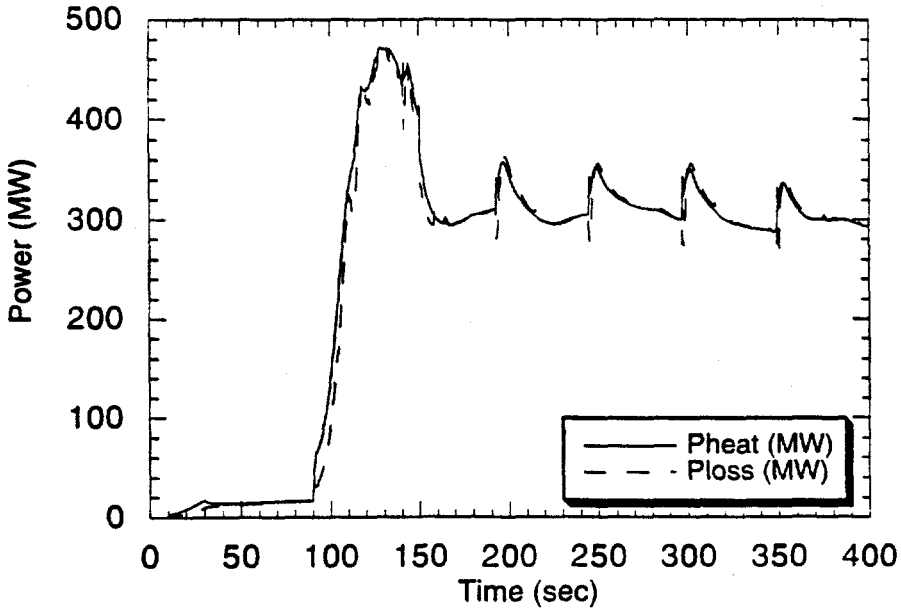

Fig. 9.3: Total heating and loss power as a function of time in the ITER reference simulation.

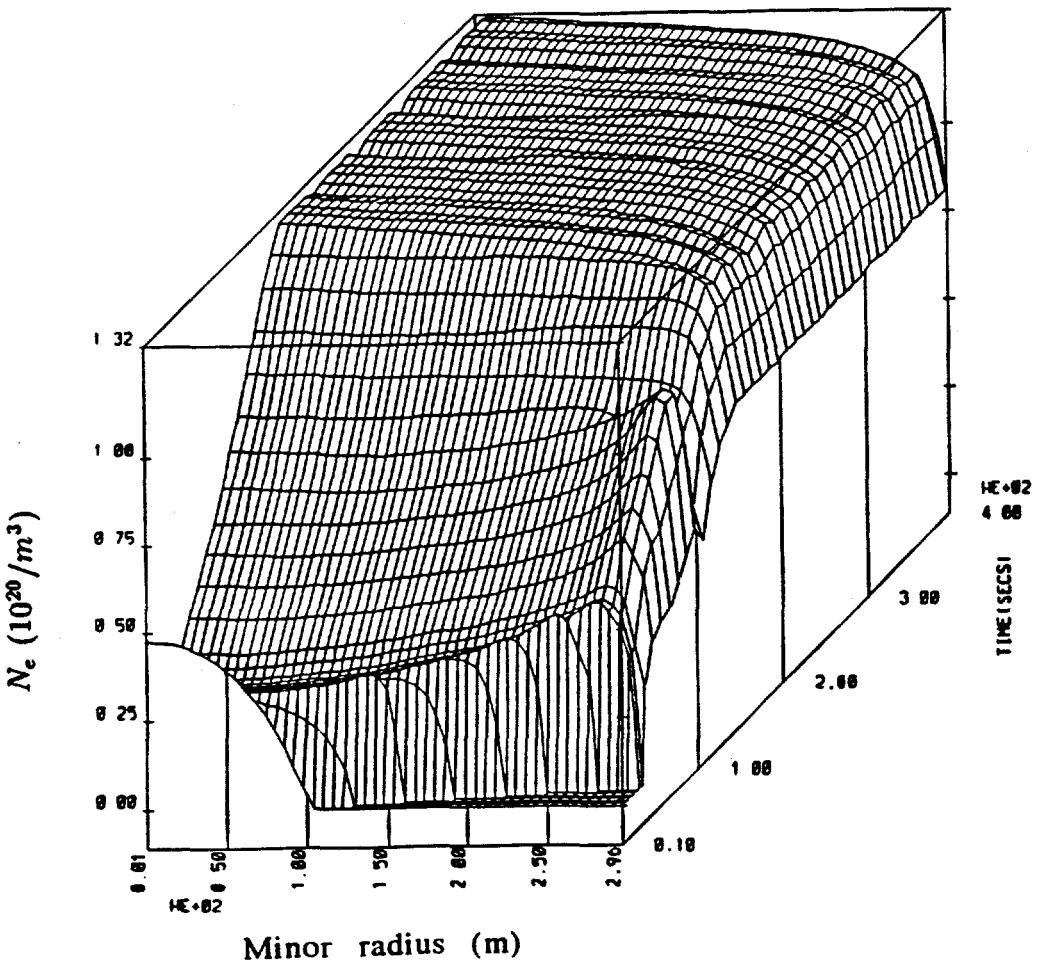

Fig. 9.4: Electron density profile as a function of time in the ITER reference simulation.

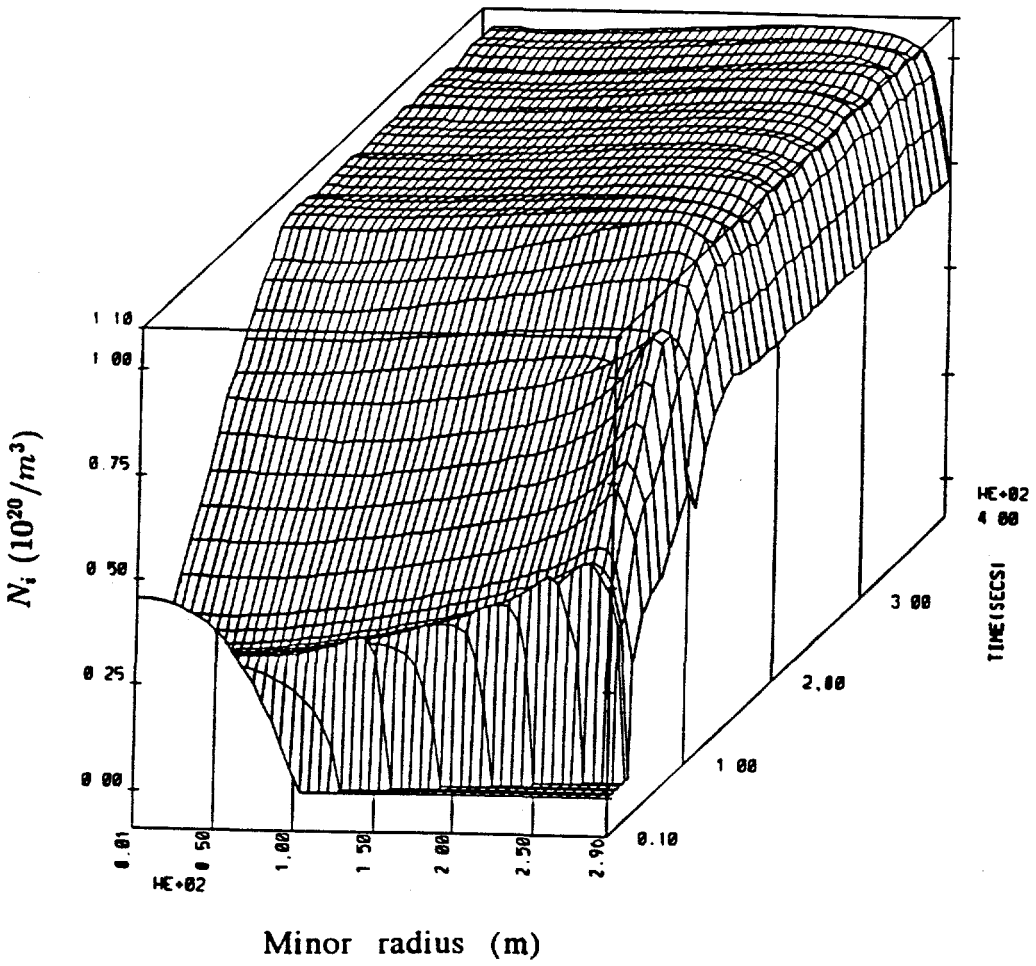

Fig. 9.5: Ion density profile as a function of time in the ITER reference simulation.

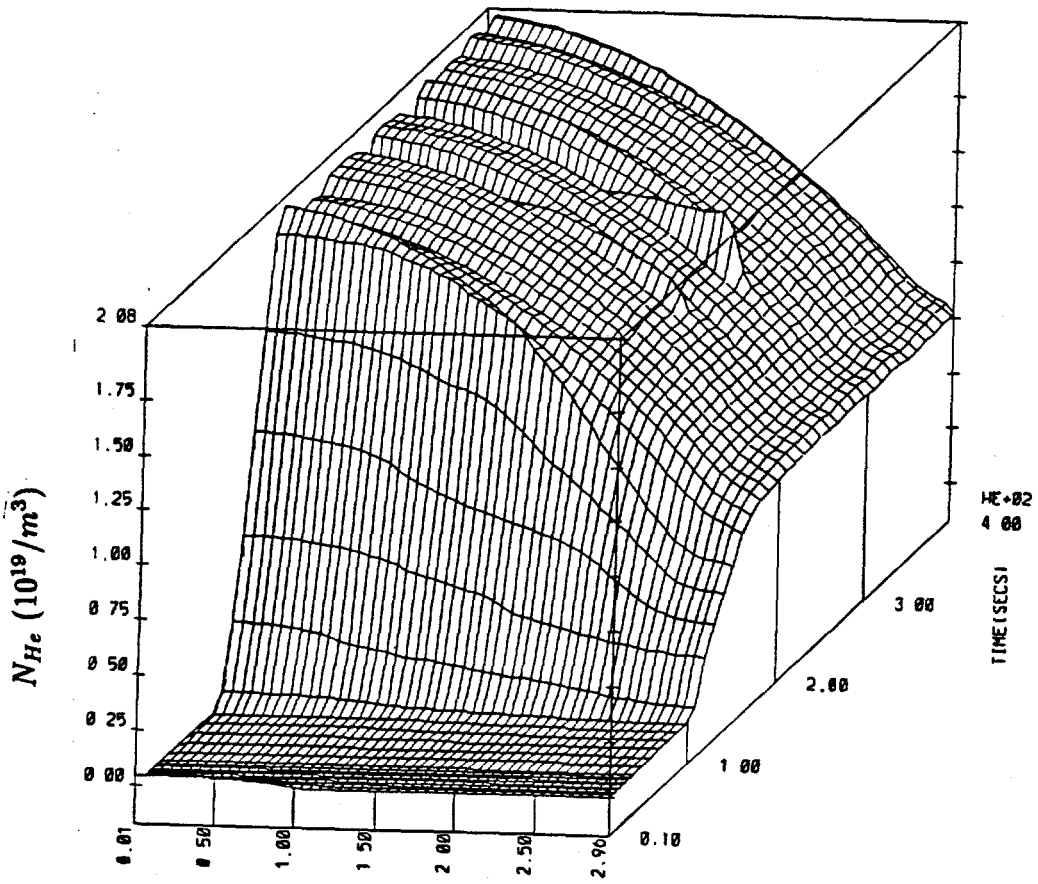

Minor Radius (m)

Fig. 9.6: Helium density profile as a function of time in the ITER reference simulation.

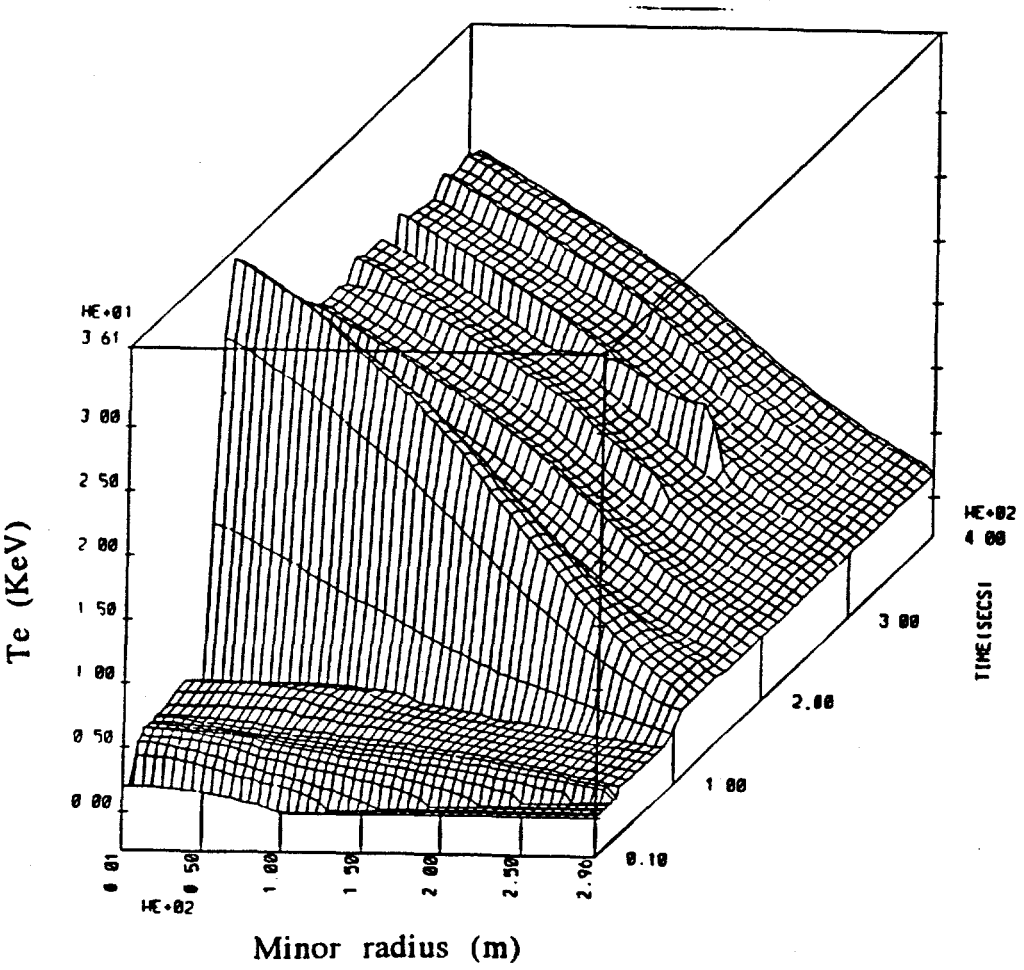

Fig. 9.7: Electron temperature profile as a function of time in the ITER reference simulation.

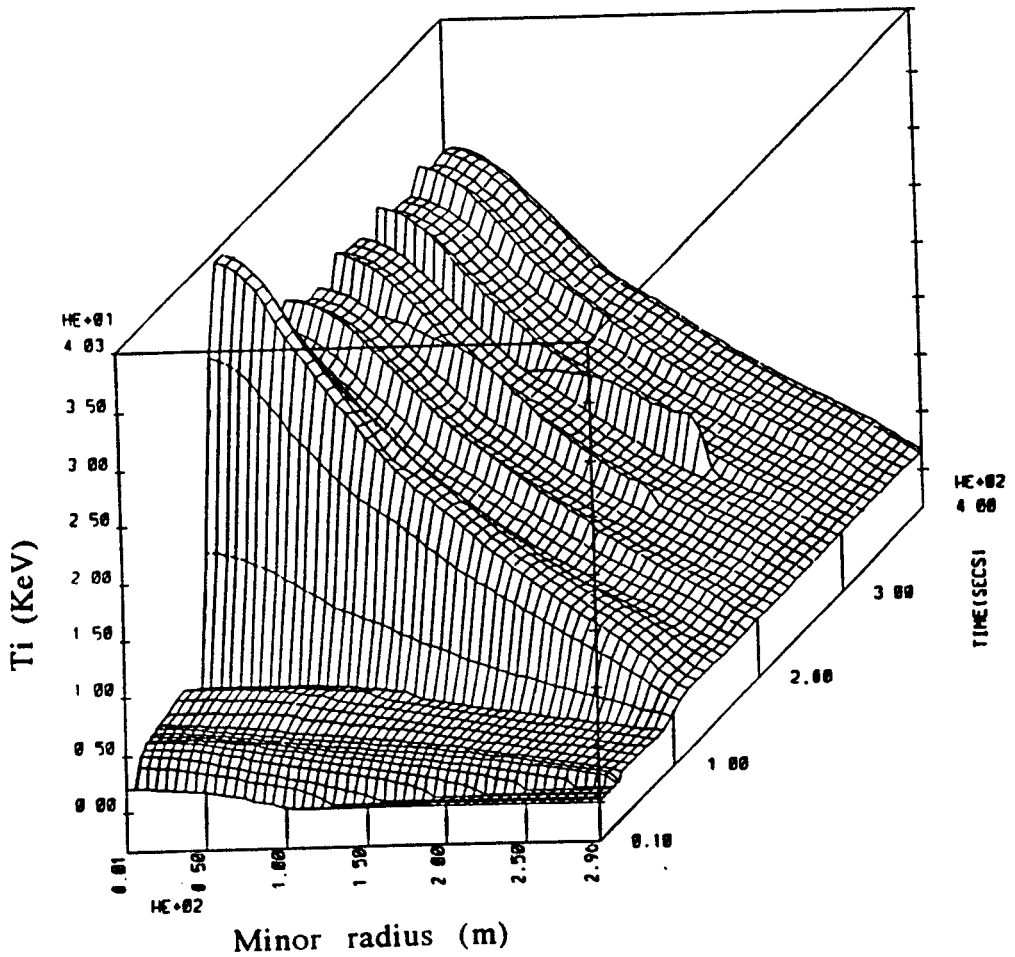

Fig. 9.8: Ion temperature profile as a function of time in the ITER reference simulation.

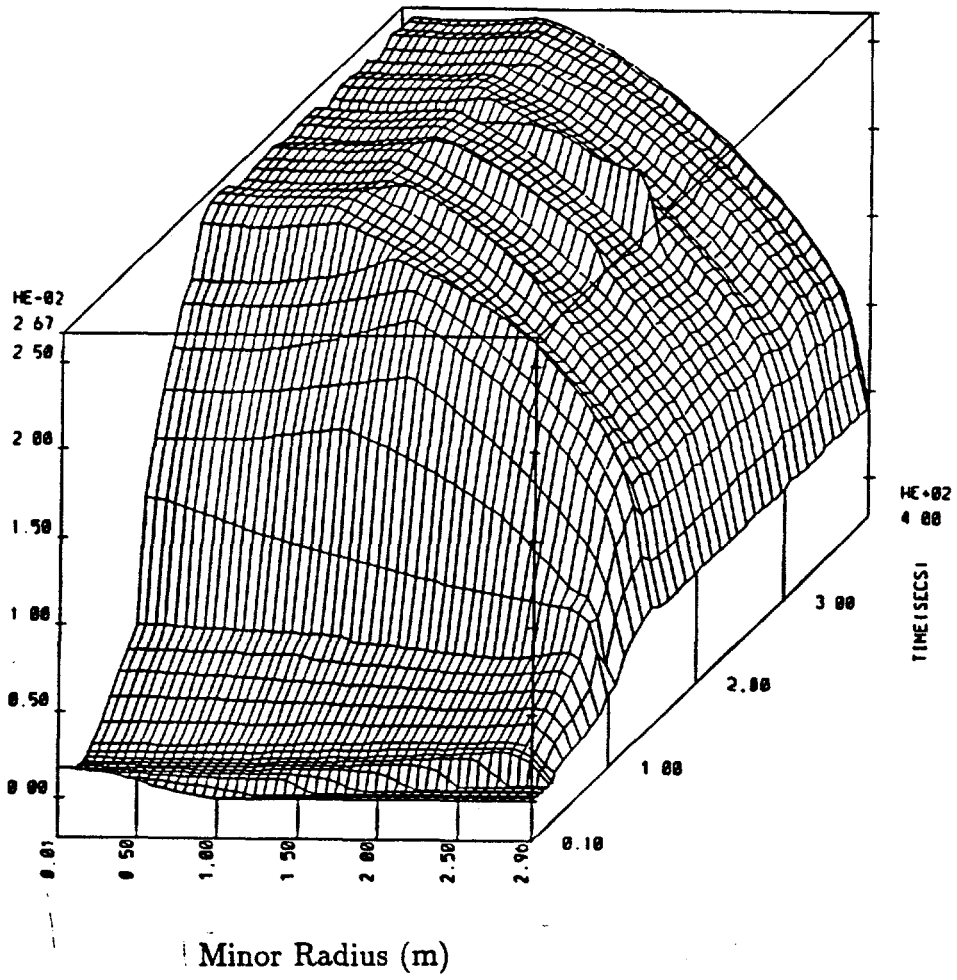

Fig. 9.9: Electron Bremsstrahlung radiation profile as a function of time in the ITER reference simulation.

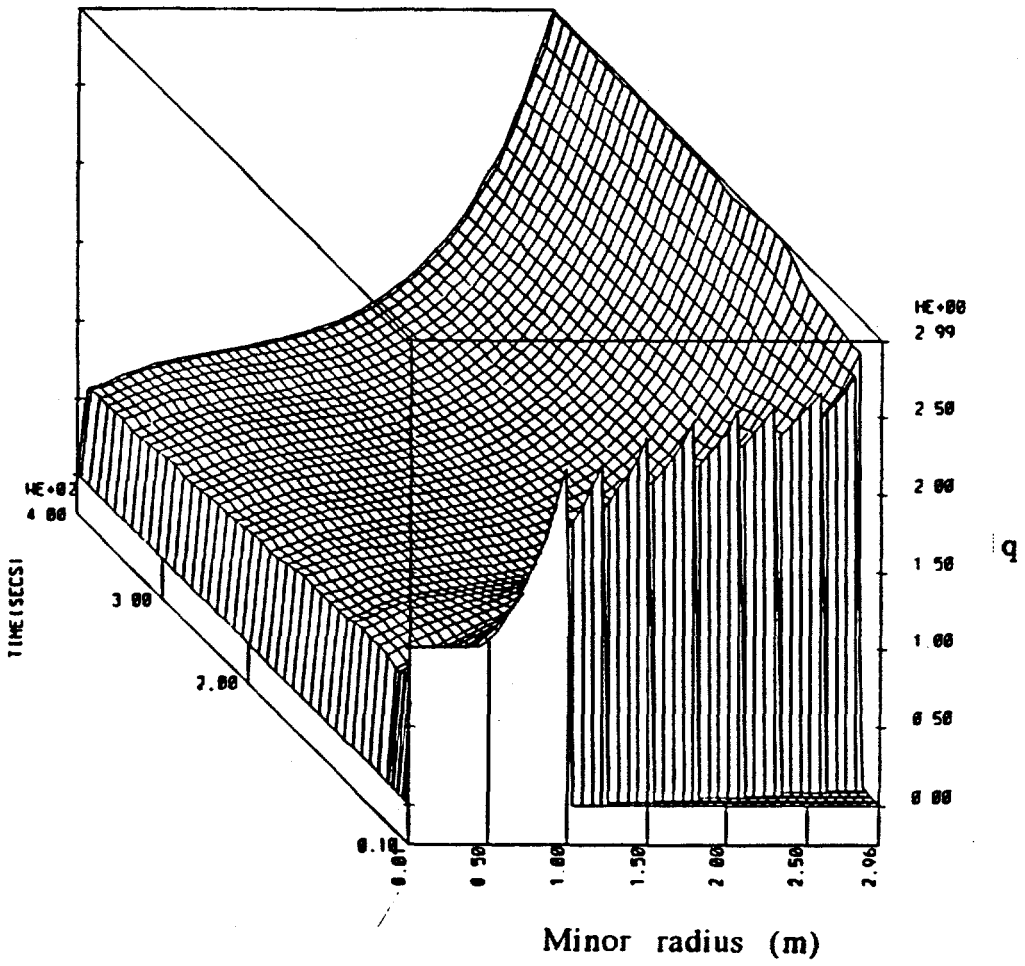

Fig. 9.10: Safety factor (q) profile as a function of time in the ITER reference simulation.

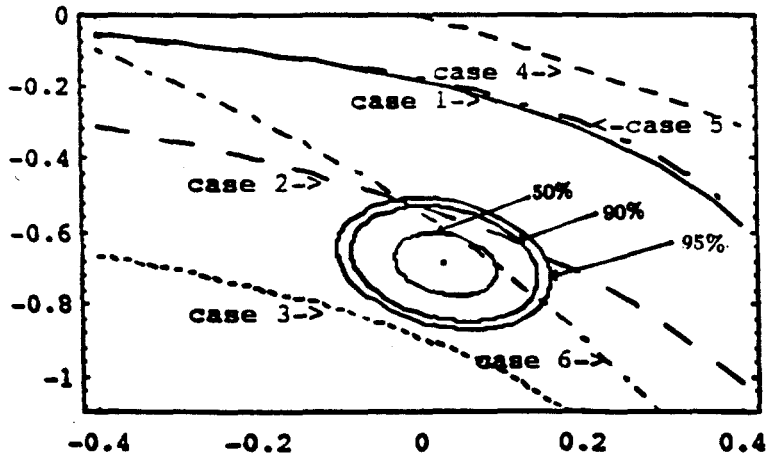

Fig. 9. 11: 50%, 90% and 95% confidence regions and the marginal ignition function for different cases.

Chapter 10

Conclusions

In this work, we have applied the methodology of mathematical modeling to the study of plasma transport in tokamaks using a theory-based multi-mode transport model. This model includes a linear combination of contribution corresponding to the drift wave branch and ballooning branch of the appropriate dispersion relation, together with neoclassical transport in the radial flux formulas. A Bayesian parameter estimation method was established including experimental calibration error/model offsets and error bar rescaling factors to determine the saturation level of drift wave and ballooning branches in the multi-mode transport model with quantitative confidence level of calibrated parameters. A trial application to the calibration of a gyroBohm multi-mode transport model with testing on a pair of DIII-D discharges shows the effectiveness of the Bayesian estimation method. This method was then applied to calibrating the nominal transport model used by Kinsey et al. against a wide range database from seven tokamaks and twelve discharges. The relatively small confidence regions obtained suggest that these estimators may be useful. The calibrated transport model was then verified and tested on five discharges from JT-60 with no adjustable constants. The results showed a reasonablely good agreement with experimental data. Finally, the tested multi-mode tokamak plasma transport model was applied to the transport analysis of the ignition probability in a next generation machine ITER. The reference simulation using basic ITER engineering design activity (EDA) parameters shows that a self-sustained thermonuclear burn with 1.5 GW

output power can be achieved provided that impurity control makes radiative losses sufficiently small in a plasma density $1.2 \times 10^{20}/m^3$ using 50 MW auxiliary heating. The ignition probability of ITER for the EDA parameters can be nominally as high as 99.9%. The same probability for concept design activity (CDA) parameters of ITER, which has small size and lower current, is only 62.6%. Adequate confinement is of critical importance in achieving a self-sustained thermonuclear burn. These results are in agreement with the other ITER physical studies and support the conclusion from ITER expert team, except the results from Texas/PPPL transport model study [189]. This work also shows that the systematic procedure of mathematical modeling is of great use to study the complex process like plasma transport in the tokamaks and make reasonable extrapolation analysis for the engineering design.

The discrepancy between the prediction from this transport model and that from Texas/PPPL model may be due to the different physical model and methodology used in each study. Here, we have used a set of best theoretical transport modes available at the time we started this work with systematic calibration and validation before the final application to ITER ignition study. The Texas/PPPL model represents a state of art of theoretical transport model but without following the systematic calibration and validation before the application to ITER study. One way to solve that discrepancy is to apply the systematic methodology that we have established here to the study of Texas/PPPL model. This will help to understand the difference between two transport models and enhance the confidence in the prediction of ITER from transport model.

Several useful computational tools were developed as byproducts of this study. These include a package of preparation and postprocessing softwares for BALDUR, which were written in Fortran, a numerical solver for one dimensional, time dependent, nonlinear transport equations written in C, and an objected-oriented parameter estimation code for the statistical analysis using C++ programming.

There are two improvements suggested here for the future work. One concerns plasma physics; another is in the computer engineering aspect. Concerning plasma physics aspect, current driven using neutral beam injection and/or fast waves could be investigated using the calibrated multi-mode transport model. Several new

theoretical modes, e.g. Nordman-Weiland mode and Guzdar-Drake mode, could be included and tested in the multi-mode transport model following the methodology we presented here. The same methodology can also be applied to the Texas/PPPL model. Concerning computer engineering, there is a need for an object-oriented tokamak plasma transport model. The transport code used in this study was written starting c. twenty years ago, and it does not have a good extensibility and reusability. These can be achieved using modern object-oriented programming style, e.g. C++. This code was originally implemented on Cray vector machine. The typical execution time is between three and ten minutes. A shorter computation time can be obtained through parallelizing the present code on Cray machine or on another parallel machine.

Appendix

Anomalous Transport Coefficients

The transport coefficients of different modes in the drift-wave and ballooning branches for the transport fluxes used here are given in Tables 1, 2, and 3. In Table 1, the trapped electron mode (TEM) and ion temperature gradient mode are combined in a set of expressions for $\chi^t_{e,i}$ and D^t_a. Except that the c_8 is set to 6.0 and d_{19} to 2.5, the other constants (c_j and d_j for $j \leq 81$) are set to 1.0 in this study.

Table 1. Drift/η_i and Circulating Electron Transport Coefficients

$c_s = [k_b T_e/(m_p A_i)]^{1/2}$	$\tau = T_e/T_i$	$\hat{s}_{cyl} = \lvert(r/q)(\partial q/\partial r)\rvert$
$\omega_{ci} = eB/(m_p A_i)$	$\beta = (2\mu_o k_b/B_o^2)(n_e T_e + n_i T_i)$	$k = 1 - (r/a)$
$v_e = (2k_b T_e/m_e)^{1/2}$	$\Lambda_{Coul} = 37.8 - \ln(n_e^{1/2} T_e^{-1})$	$\hat{s}_{div} = \hat{s}_{cyl} + (k^{-2}\ln^{-1}\lvert 4/k\rvert - \ln^{-1} 4)\delta$
$v_i = (2k_b T_i/m_p A_i)^{1/2}$	$\nu_{ei} = \frac{4(2\pi)^{1/2} n_e \Lambda_{Coul} e^4}{3(4\pi\epsilon_o)^2 m_e^{1/2}(k_b T_e)^{3/2}}$	where $\delta = \begin{cases} 0 & \text{limiter plasmas} \\ 1 & \text{divertor plasmas} \end{cases}$
$\rho_i = v_i/\omega_{ci}$	$\nu_e^* = \nu_{ei} q R_o/(\epsilon^{3/2} v_e)$	$\hat{s}_{lim} = \min[\hat{s}_{div}, r/\rho_{\theta i}]$
$\epsilon = r/R_o$	$f_{coll} = \min[1, .1c_{21}/\nu_{e*}]$	$\hat{s} = \max[.5d_3, \hat{s}_{lim}]$
$\rho_{\theta i} = \rho_i q/\epsilon$	$L_n = \max[\lvert -n_e/(\partial n_e/\partial r)\rvert, \rho_{\theta i}]$	$\beta'_{c1} = \hat{s}/(1.7q^2 R_o)$
$\rho_s = c_s/\omega_{ci}$	$\epsilon_n = L_n/R_o$	$\eta_{e,i} = L_n/L_{Te,i}$
$k_\perp = 0.3/\rho_s$	$L_{Ti} = \max[\lvert -T_i/(\partial T_i/\partial r)\rvert, \rho_{\theta i}]$	$\eta_i^{th} = \max[c_{30}, 5d_{31} L_n/R, 20d_{32} L_n/(R_o q)]$
$\omega_e^* = k_\perp \rho_s c_s/L_n$	$L_{ei} = \max[\lvert -T_e/(\partial T_e/\partial r)\rvert, \rho_{\theta i}]$	$f_{ith} = \begin{cases} 0. & \eta_i < \eta_i^{th} \\ c_6(\eta_i/\eta_i^{th} - 1)/c_7 & \eta_i^{th} \le \eta_i \le (1+c_7)\eta_i^{th} \\ c_6 & \eta_i > (1+c_7)\eta_i^{th} \end{cases}$
$D = \omega_e^*/k_\perp^2$	$L_\beta = \max[\lvert -\beta/(\partial\beta/\partial r)\rvert, \rho_{\theta i}]$	
$\omega_{te} = \hat{s} v_e/(qR_o)$	$\beta' = \beta/L_\beta$	

$F_\beta = (1+\beta'/\beta'_{c1})/[1+(\beta'/\beta'_{c1})^3]$	$\hat{D}_{te} = \epsilon^{1/2} D f_{coll}$	$D^{CE} = (\nu_{ei}\omega_e^*/\omega_{te}^2)(1 + c_{80} f_{ith}\eta_e \epsilon_n) D$
$F_\tau = \exp\{-[d_{22}(\tau^{-1} - 1)/2]^2\}$	$\hat{D}_e^t = F_\kappa F_\tau F_\beta \hat{D}_{te}$	$\chi_e^t = (1 - .6d_{19} f_{ith})\hat{D}_e^t$
$F_\kappa^t = \kappa^{-4d_{12}}$	$\hat{D}_i = (2\eta_i\epsilon_n/\tau)^{1/2} D\kappa^{-4d_{12}}$	$\chi_i^t = \hat{D}_e^t + f_{ith}\hat{D}_i^t$
$F_\kappa^c = \kappa^{-4d_{81}}$	$\hat{D}_i^t = F_\kappa F_\tau F_\beta \hat{D}_i$	$\chi_i^{CE} = \chi_e^{CE} = D_a^{CE} = F_\kappa^c F_\tau D^{CE}$
	$D_a^t = [1 - f_{ith}\eta_e/(c_{23} + \nu_{e*})]\hat{D}_e^t$	

Table 2. Kinetic and Resistive Ballooning Transport Coefficients

$\beta'_{c2} = 4\hat{s}/(q^2 R_o)$	$f_* = [(d_{42}\rho_i)^3 \mu_o \omega_{ci}/(\eta\beta q^2 L_{ni})]^2$
$f_{\beta th} = \{1 + \exp[-L_p(\beta' - \beta'_{c1})/(c_8 \rho_{\theta i})]\}^{-1}$	$f_{dia}^{RB} = (1 + f_*)^{-1/6}$
$\langle n \rangle = \max[3d_{21}, 2]$	$\Lambda = [2/(3\pi)] \ln[(\hat{s}/\langle n \rangle)^4 S^2 L_p/(\beta R_o q^8)]$
$L_{ns} = \max[\lvert - n_i/(\partial n_i/\partial r)\rvert, \rho_{\theta i}]$	$F_\kappa^{RB} = \kappa^{-4d_{14}}$
$F_\kappa^{KB} = \kappa^{-4d_{13}}$	
	$\chi_i^{KB} = \chi_e^{KB} = D_a^{KB} = F_\kappa^{KB} D^{KB}$
$D^{KB} = \omega_e^* \rho_i^2 f_{\beta th}[1 + (\beta'/\beta'_{c1})] \max[(1 - \beta'/\beta'_{c2}), 0]$	$\chi_e^{RB} = \chi_i^{RB} = D_a^{RB} = \Lambda^s f_{dia}^{RB} F_\kappa^{RB} D^{RB}$
$D^{RB} = \beta R_o q^2 r^2/(2^{1/2} L_p \hat{s} \tau_R)$	$\tilde{\chi}_e = (\beta R_o q^2/L_p)^{4/3} v_e r^2/(2^{13/6} \langle n \rangle^{2/3} S^{2/3} \hat{s})$
	$\tilde{\chi}_s^{RB} = \Lambda^{4/3} f_{dia}^{RB} f_\kappa^{RB} \tilde{\chi}_e$

Table 3. Neoclassical MHD Transport Coefficients

$\alpha_e = (1 + 1.198Z_{eff} + 0.222Z_{eff}^2)/(1 + 2.966Z_{eff} + 0.753Z_{eff}^2)$	$\eta = \nu_{ei}/(2\epsilon_o\omega_{pe}^2)$
$\delta_e = [1 + \alpha_e(1 + 1.07\nu_{*e}^{1/2} + 1.02\nu_{*e})(1 + 1.07\epsilon^{3/2}\nu_{*e})/(2.31\epsilon^{1/2})]^{-1}$	$\tau_{hp} = R_o/v_A$
$\Lambda_N = \{3\delta_e^{-1} - 1 + 2[\delta_e^{-1}(2\delta_e^{-1} - 1)]^{1/2}\}^{1/2}$	$S = \tau_R/\tau_{hp}$
$f_\Lambda = (1 - \Lambda_N^{-1})/[1 - 2^{1/2}/(\Lambda_N + \Lambda_N^3)]^{-1/2}$	$L_s = R_o q/\hat{s}$
$v_A = B/(\mu_o n_e m_p A_i)^{1/2}$	$\nu_{ii} = \nu_{ei}/(2\tau^{3/2})$
$\tau_R = r^2\mu_o/\eta$	$\nu_i = (n_i/n_e)(A_i/2)^{1/2}[1 + 2^{1/2}(Z_{eff} - 1)]\nu_{ii}$
$f_{dia}^n = [1 + (d_{75}\omega_e/\gamma_o)^6]^{-1/6}$	$\nu_{*i} = \nu_i R_o q/(\epsilon^{3/2}v_i)$
$\mu_i = 0.66\epsilon^{1/2}\nu_i(1 + 1.03\nu_{*i}^{1/2} + 0.31\nu_{*i})^{-1}(1 + 0.66\nu_{*i}\epsilon^{3/2})^{-1}$	$\omega_e = nq\rho_s c_s/(rL_n)$
$\omega_{pe} = [n_e e^2/(m_e\epsilon_o)]^{1/2}$	$\gamma_o = c_{70}[\delta_e/(4S)]^{1/3}(nq\beta R_o/L_p)^{2/3}v_A/R_o$
$f_\kappa^{NM} = \kappa^{-4d_{71}}$	$f_\gamma = \{[\mu_i/(\mu_i + \gamma_0)] + (1 + 2q^2)\epsilon^2/q^2\}^{1/2}$
$D^{NM} = \eta q\beta L_s\delta_e\Lambda_N^2/(2\mu_o\epsilon L_p)$	
$\tilde{\chi}_e = .046(4\pi)^{2/3}v_e L_e(nS)^{-2/3}(q\beta R/L_p)^{4/3}\delta_e^{5/3}\Lambda_N^{7/3}f_\Lambda f_\gamma$	$\chi_i^{NM} = \chi_e^{NM} = D_a^{NM} = f_{dia}f_\kappa^{NM}D^{NM}$
	$\tilde{\chi}_e^{NM} = f_{dia}f_\kappa^{NM}\tilde{\chi}_e$

Computer Codes

- Baldur preparation and postprocessing codes:

  AutoBaldur - unix shell script for the automatic parameter scan using queue sub mode.

  Baldurshell - unix shell script for the preparation and postprocessing.

  boundary.f - determine the boundary temperature and density for the input.

  chord.f - calculate the chord averaged line density from BALDUR output and compare with experimental data.

  extrTNmajor.f - extract the temperature and density as a function of major radius BALDUR output.

  extrTNminor.f - extract the temperature and density as a function of minor radius from BALDUR output.

  extrdiff.f - extract the radial thermal diffusion coeficients for different modes from BALDUR output.

  extrmhd.f - extract the MHD geometry of plasma in tokamak from BALDUR output.

  extrpower.f - extract the time dependent fusion power of plasma from BALDUR output.

  extrshap.f - extract the shape of magnetic flux surface from BALDUR output.

  extrtime.f - extract the time dependent parameters of plasma from BALDUR output.

  mvarpro.f - calculate residuals and variances from electron density, temperature, and ion temperature against experimental data.

  prepro.f - prepare the input data file for BALDUR.

- Transport equation solver codes:

  chi.c - calculate the transport coefficients.

  ini.c - set up initial conditions.

  mtr.c - calcualte the matrix coefficients.

  nrutil.c - set up vector and matrix.

  readin.c - set up input parameters.

  source.c - calculate the right side of matrix.

  test.c - driver code for transport equation solver.

  tridag.c - solve tridiagonal matrix equation.

- Statistic parameter estimation codes:

  Dmatrix.C - define a real type matrix.
  Func.C - define a real type single and multiple variables function.
  Likelifunc.C - define a likelihood function.
  Min1d.C - define a one-dimension optimization.
  Minmd.C - define a multi-dimension optimization.
  MLEstat.C - define a maximum likelihood estimation.
  SPDmatrix.C - define a real type sysmetric positive definite matrix.
  testmd.C - driver code for statistic parameter estimation.
  Vector.C - define an arbitray type vector array.

Bibliography

[1] W. Stacey, *Fusion: An introduction to the Physics and Technology of Magnetic Confinement Fusion*, John Wiley & Sons, New York, 1984.

[2] J.W.Connor and J. B. Taylor, "Scaling laws for plasma confinement," Nucl. Fusion, vol. 17, 1047 (1977).

[3] C. E. Singer, D. L. Jassby and J. Hovey, "Ignition of an overheated, underdense, fusioning tokamak plasma," Nucl. Fusion, vol. 20, 489 (1980).

[4] J. W. Connor, J. B. Taylor and M. F. Turner, "Ideal MHD ballooning instability and scaling law for confinement," Nucl. Fusion, vol. 24, 642 (1984).

[5] S. M. Kaye, and R. J. Goldston, "Global Energy Confinement Scaling for Neutral-Beam-Heated Tokamaks", Nucl. Fusion, vol. 25, 65 (1985).

[6] K. S. Riedel, "Advanced statistics for tokamak transport colinearity and tokamak to tokamak variation," Courant Institute of Mathematical Science: Magneto-Fluid Dynamics Division Rep., DOE/ER/53223-98, 1989.

[7] P. N. Yushmanov, et al., "Scalings for tokamak energy confinement," Nucl. Fusion, vol. 26, 1999 (1990).

[8] J. G. Cordey, J. P. Christiansen, K. Thomsen, et al., "A preliminary analy the ITER energy confinment H-mode data base," International Atomic Agency Rep., IAEA-CN-53/F-3-19, 1990.

[9] K. S. Riedel, "Random coefficient H-mode confinement scalings," N. vol. 32, 1270 (1992).

[10] A. M. Messiaen, "Experimental transport analysis and scaling to reactors," Fusion Technology, vol. 29, 216 (1995).

[11] K. Imre, K. S. Riedel and B. Schunke, "A hirearchy of empirical mode of plasma profiles and transports," Phys. Plasmas, vol. 2, 1873 (1995).

[12] E. P. Gorbunov, S. V. Mirnov and V. S. Strelkov, "Energy confinement time of a plasma as a function of the discharge parameters in Tokamak-3," Nucl. Fusion, vol. 10, 43 (1970).

[13] TFR Group, "Tokamak scaling laws, with special emphasis on TFR experimental results," Nucl. Fusion, vol. 20, 1227 (1980).

[14] M. Murakami, V. Arunasalam, J. D. Bell, et al., "Confinement studies in TFTR," Princeton Plasma Laboratory Rep., PPPL-2224, 1985.

[15] K. Odajima, Y. Shimomura, "Energy confinement scaling based on offset linear characteristics," Japanese Atomic Energy Research Institute Rep., JAERI-M 88-068, 1988.

[16] B.J.D. Tubbing, K. Thomsen, J. G. Cordey, et al., "H-mode energy confinement scaling from the DIII-D and JET tokamaks," JET Rep., JET-P(90)16, 1990.

[17] C. Daughney, "Empirical scaling for present Ohmically heated tokamaks," Nucl. Fusion, vol. 15, 967 (1975).

[18] W. Pfeiffer, and R. E. Waltz, "Empirically Scaling Laws for Energy Confinement in Ohimically-Heated Tokamaks", Nuclear Fusion, vol. 19, 51 (1979).

[19] R. J. Goldston, "Energy confinement scaling in tokamaks: some implications of recent experiments with Ohmic and strong auxiliary heating," Plasma Phys. Controlled Fusion, vol. 26, 87 (1984).

[20] J. P. Christansen, J. G. Cordey, K. Thomsen, et al., "Global energy confinement H-mode database for ITER," Nucl. Fusion, vol. 32, 291 (1992).

[21] B. Coppi and E. Muzzucato, Phys. Lett., vol. A 71, 337 (1979).

[22] C. E. Singer, "Semiempirical transport in tokamaks," J. Fusion Energy, vol. 3, 231 (1983).

[23] C. E. Singer, M. H. Redi, D. A. Boyd, A. J. Cavallo, B. Grek, D. B. Heifetz, R. A. Hulse, D. W. Johnson, W. D. Langer, B. LeBlanc, D. R. Mikkelsen, F. G. P. Seidl, A. Eberhagen, O. Gehre, F. Karger, M. Keeilhacker, S. Kissel, O. Kluber, D. Meisel, H. D. Murmann, H. Niedermeyer, H. Rapp, H. Rohr, A. Stabler, K. H. Steuer, and F. Wagner, "Semi-empirical models of H-mode discharges," Nucl. Fusion, vol. 25, 1555 (1985).

[24] C. E. Singer, L-P. Ku, and G. Bateman, "Plasma transport in a compact ignition tokamak," Princeton Plasma Physics Laboratory Rep., PPPL-2414, 1987.

[25] V. G. Merezhkin, V. S. Mukhovatov, R. Polevoi, "Transport coefficients in the T-11 tokamak," Sov. J. Plasma Phys., vol. 14, 69 (1988).

[26] P. H. Rebut, P. P. Lallia and M. L. Watkins, "Chaotic magnetic topology and heat transport in tokamaks," JET Rep., JET-P(88)05, 1988.

[27] S. C. Jardin, M. G. Bell, N. Pomphrey, et al., "TSC simulation of Ohmic discharges in TFTR," Nucl. Fusion, vol. 33, 371 (1993).

[28] C. E. Singer, E-S. Ghanem, S. Hu, and G. Miley, "Power and particle control theory I: transport in the core plasma," in Proc. International Engineering Test Reactor Workshop at Princeton, S Cohen, Ed. NJ, May 1989.

[29] F. L. Hinton and R. D. Hazeltine, "Theory of plasma transport in toroidal confinement systems," Rev. Mod. Phys., vol. 48, 239 (1976).

[30] A. A. Galeev adn R. Z. Sagdeev, "Theory of neoclassical diffusion," in *Reviews of Plasma Physics*, vol. 7, p. 257, edited by M. A. Leontovich, Consultants, New York, 1979.

[31] S. P. Hirshman and D. J. Sigmar, "Neoclassical transport of impurities in tokamak plasmas," Nucl. Fusion, vol. 21, 1079 (1981).

[32] C. S. Chang and F. L. Hinton, "Effect of finite aspect ratio on the neoclassical ion thermal conductivity in the banana regime," Phys. Fluids, vol. 25, 1493 (1982).

[33] B. B. Kadomtsev, *Tokamak Plasma: A Complex Physical System*, Institute of Physics Publishing, Bristol and Philadelphia, 1992.

[34] M. N. Rosenbluth and P. H. Rutherford, "Tokamak plasma stability," in *Fusion*, vol. 1, ed. E. Teller, Academic Press, New York, 1981.

[35] B. B. Kadomtsev and O. P. Pogutse,"Turbulent in toroidal systems," in *Reviews of Plasma Physics*, vol.5, ed. by M. A. Leontovich, Consultants Bureau, New York, p 249 (1970).

[36] W. M. Manheimer, *An Introduction to Tranpped-Particle Instability in Tokamaks*, Technical Information Center, ERDA, 1977.

[37] W. M. Tang, "Microinstability theory in tokamaks," Nucl. Fusion, vol. 18, 1089 (1978).

[38] R. D. Stambaugh, et al., Phys. Fluids, vol. 12, 2941 (1990).

[39] H. P. Furth and J. Killeen, "Finite-Resistivity Instabilities of a Sheet Pinch", Phys. Fluids, vol. 6, 459 (1963).

[40] B. A. Carreras, P. H. Dimond, M. Murakami, J. L. Dunlap, J. D. Bell, H. R. Hicks, J. A. Holmes, E. A. Lazarus, V. K. Pare, P. Similon, C. E. Thomas and R. M. Wieland, Phys. Rev. Lett., vol. 50, 503 (1983).

[41] G. Rewoldt, et al., Phys. Fluids, vol. 25, 480 (1982).

[42] H. P. Furth, P. H. Rutherford, H. Selberg, "Tearing mode in the cylindrical tokamak", Phys. Fluids, vol. 16, 1054 (1973).

[43] T. S. Hahm, P. H. Diamond, P. W. Terry, L. Garcia and B. Carreras, Phys. Fluids, vol. 30, 1452 (1987).

[44] C. E. Singer, "Testing predictive transport models," IPSG Working Group Report, September 1986.

[45] D. W. Ross, P. H. Diamond, J. F. Drake, F. L. Hinton, F. W. Perkins, W. M. Tang, R. E. Waltz and S. J. Zweben, DOE/ET5351937 and University of Texas Fusion Research Center Report FRCR #295, 1987.

[46] B. Balet, J. G. Cordey, P. M. Stubberfield, "Determination of local transport coefficients by heat flux analysis and comparisons with theoretical models", JET-P (90) 51, 1990.

[47] J. P. Christiansen, J. G. Cordey, A. Taroni,"The testing of transport models against data," Nucl. Fusion, vol. 34, 375 (1994).

[48] H. Nordman, J. Weiland, A. Jarmen, "Simulation of toroidal drift mode turbulent driven by temperature gradients and electron trapping," Nulc. Fusion, vol. 30, 983 (1990).

[49] M. Frojdh, M. Liljestrom, H. Nordman, Nucl. Fusion, vol. 32, 419 (1992).

[50] K. Itoh, S-I. Itoh, A. Fukuyama, Phys. Rev. Lett., vol. 69, 1050 (1992).

[51] K. Itoh, S-I. Itoh, A. Fukuyama, et al., Plasma Phys. Control. Fusion, vol. 36, 279 (1994).

[52] S. E. Parker, W. W. Lee, and R. A. Santoro, "Gyrokinetic simulation of ion-temperature-gradient-driven turbulent in 3-D toroidal geometry," Phys. Rev. Lett., vol. 71, 2042 (1993).

[53] M. Kotschenreuther, W. Dorland, M. A. Beer and G. W. Hammett, "Quantitative predictions of tokamak energy confinement from first-principles simulations with kinetic effects," Phys. Plasmas, vol. 2, 2381 (1995).

[54] R. E. Waltz, G. D. Kerbel, J. Milovich, et al., "Advances in the simulation of toroidal gyro-Landau fluid model turbulent," Phys. Plasmas, vol. 2, 2408 (1995).

[55] P. N. Guzdar, J. F. Drake, D. McCarthy, et al., "Three-dimensional fluid simulations of the nonlinear drift-resistive ballooning modes in tokamak edge plasmas," phys. Fluids, vol. B 5, 3712 (1995).

[56] R. R. Dominguez and R. E. Waltz, "Tokamak transport code simulations with drift wave models," Nucl. Fusion, vol. 27, 65 (1987).

[57] H. Shirai, T. Hirayama, K. Shimizu, T. Takizuka, M. Azumi, Nucl. Fusion, vol. 29, 805 (1989).

[58] H. Shirai, T. Hirayama, Y. Koide, H. Yoshida, O. Naito, M. Sato, T. Fukuda, T. Sugie, M. Azumi, D. R. Mikkelsen, S. D. Scott, B. Grek, K. W. Hill, D. W. Johnson, D. K. Mansfield, H. K. Park, B. C. Stratton, E. J. Synakowski, G. Taylor, and H. H. Towner, "Ion temperature profile simulation of JT-60 and TFTR plasmas with ion temperature gradient mode transport models," Nucl. Fusion, vol. 34, 703 (1994).

[59] B. A. Carreras and P. H. Diamond, Phys. Fluids, vol. B1, 1011 (1989).

[60] G. Bateman, "Theory-based Transport Simulations of TFTR L-mode Temperature Profiles", Phys. Fluids, vol. B4, 634 (992).

[61] C. E. Singer, "Theoretical particle and energy flux formulas for tokamak," Comment on Plasma Physics and Controlled Fusion, vol. 11, 165 (1988).

[62] E. M. Ghanem, C. E. Singer, G. Bateman, and D. P. Stotler, "Multiple mode model of tokamak transport," Nucl. Fusion, vol. 30, 1595 (1990).

[63] E. M. Ghanem, *Theoretical Transport Model for Tokamak*, University of Illinois at Urbana-Champaign Department of Nuclear Engineering PhD Thesis, 1991.

[64] G. Bateman, J. Weiland, H. Nordman, J. Kinsey, and C. Singer, "Theory-based transport modeling of TFTR," Physica Scripta, vol. 51, 597 (1995).

[65] M. H. Redi and G. Bateman, "Transport simulation of TFTR experiments to test theoretical models for χ_e and χ_i," Nucl. Fusion, vol. 31, 547 (1991).

[66] M. H. Redi, J. C. Cummings, C. E. Bush, et al., "Transport simulations of TFTR: theoretically based transport models and current scaling," Nucl. Fusion, vol. 34, 809 (1994).

[67] S. J. Park, *Tuning Complex Computer Codes to Data and Optimal Designs*, University of Illinois at Urbana-Champaign Department of Statistics PhD Thesis, 1992.

[68] T. Djemil, *Methods for Testing Transport Models*, University of Illinois at Urbana-Champaign Department of Nuclear Engineering PhD Thesis, 1992.

[69] J. Kinsey, *H-mode Transport of Tokamak Plasmas*, University of Illinois at Urbana-Champaign Department of Nuclear Engineering Masters Thesis, 1991.

[70] J. Kinsey, *Systematic Calibration of a Theory-based Transport Model of Tokamak Plasmas*, University of Illinois at Urbana-Champaign Department of Nuclear Engineering PhD Thesis, 1995.

[71] J. Kinsey, et al., "Systematic Comparison of a Theory-based Transport Model with a Multi-tokamak Profile Database", Phys. Plasmas, vol. 2, 811 (1995).

[72] J. Kinsey, C. E. Singer, et al., "Systematic comparison of a theory-based transport model with a muti-tokamak profile database," Phys. Scr., vol. 52, 428 (1995).

[73] J. Kinsey and G. Bateman, "Theory-based transport modeling of the gyro-radius experiments," Phys. Plasmas, vol. 3, 3344 (1996).

[74] J. Qiang, *Calibration and Application of a Tokamak Transport Model in JT-60*, University of Illinois at Urbana-Champaign Department of Nuclear Engineering Master Thesis, 1995.

[75] J. Qiang and C. E. Singer, "Parameter estimation in a tokamak transport model and application to L- and H-mode simulations," IEEE Tran. on Plasma Sci, vol. 24, 1202 (1996).

[76] J. Qiang, J. Kinsey and C. E. Singer, "Confidence contours for calibration of a theoretical transport model against a multitokamak database," Nucl. Fusion, vol. 36, 1019 (1996).

[77] J. Qiang, C. E. Singer and T. Hirayama, "Simulation of JT-60 discharges with an experimentally calibrated theoretical transport model," Jpn. J. Appl. Phys., vol. 35, 2797 (1996).

[78] J. Qiang, C. E. Singer and A. Levinson, "Application of a calibrated tokamak transport model to ITER ignition studies," Fusion Tech., vol. 31, 311 (1997).

[79] N. A. Uckan, J. Hogan, W. Houlberg, et al., "ITER design:physics basis for size, confinement capability power levels and burn control," Fusion Tech., vol. 26, 327 (1994).

[80] R. V. Budny, D. C. McCune, et al., "Transp simulation of International Thermonuclear Experimental Reactor plasma," Phys. Plasmas, vol. 3, 4583 (1996).

[81] G. Bateman, J. Kinsey, et al., "Model for predicting temperature and density profiles in tokamaks," Bull. Am. Phys. Soc., vol. 41, xx (1996).

[82] M. Kotschenreuther and W. Dorland, "First principles simulations of reactor performance," Bull. Am. Phys. Soc., vol. 40, 1727 (1995).

[83] D. Murthy, N. Page and E. Rodin, *Mathematical Modelling: A Tool for Problem Solving in Engineering, Physical, Biological and Social Sciences*, Pergamon Press, Oxford, 1990.

[84] W. Gilchrist, *Statistical Modelling*, John Wiley & Sons, Chichester, 1984.

[85] S. Jacoby, J. Kowalik and H. Burner, *mathematical Modeling with Computers*, Prentice-Hall, Englewood Cliffs, 1980.

[86] J. Berry, D. Burghes, I. Huntley, D. James and A. Moscardini, *Mathematical Modelling Courses*, John Wiley & Sons, New York, 1987.

[87] D. Maki and M. Thompson, *Mathematical Models and Applications*, Prentice-Hall, Englewood Cliffs, 1973.

[88] D. Clements, *Mathematical Modelling: A Case Study Approach*, Cambridge University Press, Cambridge, 1989.

[89] M. Cross and A. Moscardini, *Learning the Art of Mathematical Modelling*, John Wiley & Sons, New York, 1985.

[90] D. Burghes, I. Huntley and J. McDonald, *Applying Mathematics: A Course in Mathematical Modelling*, John Wiley & Sons, New York, 1982.

[91] J. Andrews and R. McLone, *Mathematical Modelling*, Butterworths, London, 1976.

[92] C. Dym and E. Ivey, *Principles of Mathematical Modeling*, Academic Press, New York, 1980.

[93] F. Wan, *Mathematical Models and Their Analysis*, Harper & Row Publishers, New York, 1989.

[94] H. Nayfeh, *Introduction to Perturbation Techniques*, John Wiley & Sons, New York, 1981.

[95] F. Neelamkavil, *Computer Simulation and Modellling*, John Wiley & Sons, Chichester, 1987.

[96] R. McHaney, *Computer Simulation: A Practical Perspective*, Academic Press, San Diego, 1991.

[97] A. Bera, *Intorduction to Statistics for Econonmetricians*, University of Illinois Lecture Notes, 1995.

[98] H. Sorenson, *Parameter Estimation: Principles and Problems*, Marcel Dekker, New York, 1980.

[99] E. Lehmann, *Theory of Point Estimation*, Wadsworth, Belmont, 1991.

[100] E. Lehmann, *Testing Statistical Hypotheses*, John Wiley & Sons, New York, 1959.

[101] H. R. Strauss, "Dynamics of high β tokamaks," Phys. Fluids, vol. 20, 1354 (1977).

[102] K. T. Tsang, "Finite Larmor radius stabilization of ballooning modes in tokamaks," Phys. Fluids, vol. 24, 2017 (1981).

[103] B. A. Carreras and P. H. Diamond, Phys. Fluids, vol. B1, 1011 (1989).

[104] A. B. Rechester and M. N. Rosenbluth, "Electron heat transport in a tokamak with destroyed magnetic surfaces," Phys. Rev. Lett., vol. 40, 38 (1978).

[105] D. W. Swain, et al., in *Controlled Fusion and Plasma Physics*, (Proc. 9th Europ. Conf. Oxford, 1979), vol. 44 (B2.2).

[106] W. H. Choe and J. P. Freidberg, Phys. Fluids, vol. 29, 1768 (1986).

[107] E. A. Frieman, G. Rewoldt, W. M. Tang, and A. H. Glasser, "General theory of kinetic ballooning modes," Phys. Fluids, vol. 23, 1750 (1980).

[108] W. M. Tang, J. W. Connor, and R. J. Hastie, "Kinetic-ballooning-mode theory in general geometry", Nucl. Fusion, vol. 20, 1439 (1980).

[109] W. M. Tang, G. Rewoldt, C. Z. Cheng, and M. S. Chance, "Kinetic analysis of MHD ballooning modes in tokamaks", Nucl. Fusion, vol. 25, 151 (1985).

[110] C. Z. Cheng, "Kinetic theory of collisionless ballooning modes", Phys. Fluids, vol. 25, 1020 (1982).

[111] O. J. Kwon, P. H. Diamond and H. Biglari, "Theory of neoclassical pressure-gradient-driven turbulence", Phys. Fluids, vol. B2, 291 (1990).

[112] J. D. Callen and K. C. Shaing, Phys. Fluids, vol. 28, 1845 (1985).

[113] J. Kinsey, A. Kritz, P. Bonoli and M. Porkolab, "Time-dependent scenario modeling of TPX using a theory-based transport model," submitted to Nucl. Fusion, 1995.

[114] W. Horton, et al., Phys. Fluids, vol. 24, 1077 (1981).

[115] G. Rewoldt, W. M. Tang, and R. J. Hastie, "Collisional effects on kinetic electromagnetic modes and associated quasilinear transport", Phys. Fluids, vol. 30, 807 (1987).

[116] K. Miyamoto, *Plasma Physics for Nuclear Fusion*, The MIT Press, Cambridge, 1976.

[117] F. Romanelli, et al., Phys. Fluids, vol. B1, 1018 (1989).

[118] S. Hamaguchi and W. Horton, Phys. Fluids, vol. B2, 1833 (1990).

[119] W. Horton, D.-I Choi and W. M. Tang, "Toroidal drift modes driven by ion pressure gradients," Phys. Fluids, vol. 24, 1077 (1981).

[120] W. W. Lee and W. M. Tang, "Gyrokinetic particle simulation of ion temperature gradient drift instabilities," Plasma Physics Laboratory Rep., PPPL-2431, 1987.

[121] A. A. Galeev, V. N. Oraevskii, and R. Z. Sagdeev, "Universal instability of an infomogeneous plasma in a magnetic field," Soviet Physics JETP, vol. 17, 615 (1963).

[122] B. Coppi, M. N. Rosenbluth, R. Z. Sagdeev, Phys. Fluids, vol. 10, 582 (1967).

[123] R. Linsker, "Integral-equation formulation for drift eigenmodes in cylindrically symmetric systems," Phys. Fluids, vol. 24, 1485 (1981).

[124] H. Biglari, P. H. Diamond, and M. N. Rosenbluth, "Toroidal ion-pressure-gradient-driven drift instabilities and transport revisited," Phys. Fluids, vol. B1, 109 (1989).

[125] J. Q. Dong, et al., Phys. Plasmas, vol. 1, 3635 (1994).

[126] J. Wesson, *Tokamaks*, Clarendon Press, Oxford, 1987.

[127] T. Antonsen, B. Coppi, R. Englade, "Inward particle transport by plasma collective models," Nucl. Fusion, vol. 19, 641 (1979).

[128] P. N. Guzdar, L. Chen, W. M. Tang, and P. H. Rutherford, Phys. Fluids, vol. 26, 673 (1983).

[129] G. D. Smith, *Numerical Solution of Partial Differential Equations: Finite Difference Methods*, Clarendon Press, Oxford, 1985.

[130] F. L. Stasa, *Applied Finite Element Analysis for Engineers*, Saunders College Publishing, Fort Worh, 1985.

[131] S. Nakamura, *Computational methods in Engineering and Science: with Application to Fluid Dynamic and Nuclear Systems*, Robert E. Krieger Publishing Company, Malabar, 1986.

[132] R. D. Lawrence and J. J. Dorning, "A nodal Green's function method for multidimensional neutron diffusion calculations," Nucl. Sci. and Eng., vol. 76, 218 (1980).

[133] D. F. Duchs, D. E. Post, P. H. Rutherford, Nucl. Fusion, vol. 17, 565 (1977).

[134] W. A. Houlberg, S. E. Attengerger and L. M. Hively, Nucl. Fusion, vol. 22, 935 (1982).

[135] H. C. Howe, "Physics models in the transport code PROCTR," ORNL/TM-9537, 1985.

[136] R. J. Goldston, D. C. McCune, H. H. Towner, et al., J. Comput. Phys., vol. 43, 61 (1981).

[137] R. M. Wieland, H. C. Howe, E. A. Lazerus, M. Murakemi, et al., Nucl. Fusion, vol. 23, 447 (1983).

[138] C. E. Singer, D. E. Post, D. R. Mikkelsen, M. H. Redi, A. McKenney, et al., "BALDUR: a one-dimensional plasma transport code," Computer Phys. Communications, vol. 49, 273 (1988).

[139] M. K. Jain, *Numerical Solution of Differential Equations*, Wiley Eastern Limited, New Delhi, 1984.

[140] L. F. Shampine, *Numerical Solution of Ordinary Differential Equations*, Chapman & Hall, New York, 1994.

[141] M. G. Kendall,"Daniel Bernouli on maximum likelihood," Biometrika, vol. 48, 1 (1961).

[142] G. A. Barnard, "Thomas Bayes essay towards solving a problem in the doctrine of chances," Biometrika, vol. 45, 293 (1958).

[143] K. G. Gauss, *Theory of Motion of the Heavenly Bodies*, Dover, New York (1963).

[144] I. Todhunter, *A History of the Mathematical Theory of Probability*, Macmillan, New York (1865).

[145] R. A. Fisher, "Theory of statistical estimations," Proc. Phil. Soc. Cambridge, vol. 22, 700 (1925).

[146] H. Cramer, *Mathematical Methods of Statistics*, Princeton University Press, New Jersey, 1946.

[147] H. R. Schwarz, *Numerical Analysis: A Comprehensive Introduction*, John Wiley & Sons, Chichester, 1989.

[148] M. Heath, *Scientific Computing: An Introductory Survey*, McGrow Companies, INC., New York, 1997.

[149] R. Fletcher and C. M. Reeves, "Function minimization by conjugate gradients," Computer J., vol. 7, 149 (1964).

[150] W. H. Press, B. P. Flannery, S. A. Teukolsky and W. T. Vetterling, *Numerical Recipes in C*, Cambridge University Press, Cambridge, 1989.

[151] G. Booch, *Object Oriented Design: With Applications*, The Benjamin Cummings Publishing Company, Redwood City, 1991.

[152] P. H. Rebut, M. L. Watkins, D. J. Gambier, and D. Boucher, "A program toward a fusion reactor," Phys. Fluids, vol. 3, 2209 (1991).

[153] J. G. Cordey, D. G. Muir, S. V. Nerdachin, V. V. Parail, E. Springmann, and A. Taroni, "A numerical simulation of the L-H transition in JET with local and global models of anomalous transport," Nucl. Fusion, vol. 35, 101 (1995).

[154] M. Murakami, S. C. Bates, J. D. Bell, C. E. Bush, A. Carnevali, B. A. Carreras, J. L. Dunlap, P. H. Edmonds, O. C. Eldridge, A. C. England, W. L. Gardner, J. H. Harris, H. C. Howe, D. P. Hutchinson, R. C. Isler, T. C. Jernigan, R. R. Kindsfater, P. W. King, R. A. Langley, E. A. Lazarus, J. f. Lyon, C. H. Ma, P. K. Mioduszewski, L . E. Murray, G. H. Neilson, V. K. Pare, M. J. Saltmarsh, S. D. Scott, D. J. Sigmar, J. E. Simpkins, K. A. Stewart, W. L. Stirling, C. E. Thomas, R. M. Wieland, J. B. Wilgen, W. R. Wing, and A. J. Wooton, "Beta scaling experiments in ISX-B," *Plasma Physics and Controlled Fusion Research*, vol. 1, 45 (1984).

[155] G. E. P. Box and G. C. Tiao, *Bayesian Inference in Statistical Analysis*, Reading, MA: Addison-Wesley, 1973.

[156] S.C. McCool, A.J. Wootton, A.Y. Aydemir, R.D. Bengston, J.A. Boedo, R.V. Bravenec, D.L. Brower, J.S. DeGrassie, T.E. Evans, S.P. Fan, J.C. Forster, M.S. Foster, K.W. Gentle, Y.X. He, R.L. Hickock, G.L. Jackson, S.K. Kim, M. Kotschenreuther, N.C. Luhmann, Jr., W.H. Miner, Jr., N. Ohyabu, D.M. Patterson, W.A. Peebles, P.E. Phillips, T.L. Rhodes, B. Richards, P. Ritz, D.W. Ross, W.L. Rowan, P.M. Schoch, B.A. Smith, J.C. Wiley, X.H. Yu, and S.B. Zheng, "Electron thermal confinement studies with applied resonant fields on TEXT," Nucl. Fusion, vol. 29, 547 (1989).

[157] N. J. Lopes Cardozo, "Anomalous transport due to magnetic turbulence," Fusion Technology, vol. 25, 146 (1994).

[158] R. E. Waltz, J. C. DeBoo, and T. H. Osborne, "Modeling of almost dimensionally similar discharges," Nucl. Fusion, vol. 32, 1051 (1992).

[159] F. W. Perkins, C. W. Barnes, D. W. Johnson, S. D. Scott, M. C. Zarnstorff, M. G. Bell, R. E. Bell, C. E. Bush, B. Grek, K. W. Hill, D. K. Mansfield, H. Park, A. T. Ramsey, J. Schivell, B. C. Stratton, and E. Synakowski, "Nondimensional transport scaling in the Tokamak Fusion Test Reactor: is tokamak transport Bohm or gyro-Bhom?," Phys. Fluids, vol. 5, 477 (1993).

[160] J. P. Christiansen, P. M. Stubberfield, J. G. Cordey, C. Gormezano, C. W. Gowers, J. O'Rourke, D. Stork, A. Taroni, C. D. Challis, "The scaling of transport with normalized Larmor radius in JET," Nucl. Fusion, vol. 33, 863 (1993).

[161] W. Dorland, M. Kotschenreuther, M. A. Beer, G. E. Hammett, D. Mikkelsen, and J. Q.Dong, "Detailed comparisons of nonlinear gyrofluid ITG simulations and experiment," Bull. Am. Phys. Soc., vol. 39, 1664 (1994).

[162] W. Dorland, M. Kotschenreuther, M. A. Beer, G. W. Hammett, S. M. Smith, "Progress toward a complete gyrofluid/gyrokinetic transport model," Bull. Am. Phys. Soc., vol. 40, 1647 (1995).

[163] N. L. Johnson and F. C. Leone, *Statistics and Experimental Design*, vol. 1, J. Wiley and Sons, Inc., 1964.

[164] C. L. Jahns, R. J. Groebner, and H. St. John, "Comparison of transport in H- and L- phase discharge in the DIII-D tokamak," Nucl. Fusion, vol. 29, 1271 (1989).

[165] J. Kinsey, G. Bateman, A. H. Kritz and A. Redd, "Comparison of two resistive ballooning mode models in transport simulations," submitted to Phys. Plasmas, 1995.

[166] Personal Communication with Dr. J. F. Drake of University of Maryland, 1995.

[167] T. Hirayama, H. Shirai, M. Yagi, K. Shimizu, Y. Koide, M. Kikuchi and M. Azumi: Nucl. Fusion **32** (1992) 89.

[168] B. B. Kadomtsev and O. P. Poguste, Nucl. Fusion, vol. 11, 67 (1971).

[169] K. Young, M. Bell, W. Blanchard, N. Bretz, J. Cecchi, J. Coonrod, S. Davis, H. Dylla, P. Efthimion, R. Fonck, R. Goldston, D. Grove, R. Hawryluk, H. Hendel, K. Hell, J. Isaacson, L. Johnson, R. Kaita, R. Krawchuk, R. Little, M. McCarthy, D. McCune, K. McGuire, D. Meade, S. C Medley, D. Mikkelson, D. Mueller, E. Nieschmidt, K. Owens, A. Ramsey, A. Roquemore, L. Samuelson, N. Sauthoff, J. Schivell, J. Schmidt, S. Sesnic, J. Sinnis, J. Strachan, G. Tait, G. Taylor, F. Tenney and M. Ulrickson, Plasma Phys. Control. Fusion, vol. 26, 11 (1984).

[170] C. E. Singer, G. Bateman and D. P. Stotler, Princetion Plasma Phys. Lab. Rep. PPPL-2527, 1989.

[171] T. Hirayama, K. Shimizu, K. Tani, H. Shirai, M. Kikuchi, Jap. At. Energy Res. Inst. Rep. JAERI-M 88-043, 1988.

[172] T. Hirayama, H. Shirai, K. Shimizu, Y. Koide, H. Yoshida, M. Sato, K. Nagashima, T. Nishitani, T. Fukuda, H. Kubo, Y. Kawano, M. Kikuchi and M. Azumi, ITER-IL-Ph-4-0-J-01, 1990.

[173] J. Mandrekas, W. M. Stacey, and H. He, "1-1/2D transport studies of ITER burn control scenarios," Fusion Technol., vol. 19, 1307 (1991).

[174] W. A. Houlberg and N. A. Uckan, "Transport analysis of ITER startup, burn, and shutdown scenarios," Fusion Technol., vol. 21, 1421 (1992).

[175] G. Becker, "Investigation of transport in the ignition ITER plasma by computer simulations," Nucl. Fusion, vol. 33, 1435 (1993).

[176] G. Becker, "Transport simulations of the ignition ITER with high helium fraction," Nucl. Fusion, vol. 34, 507 (1994).

[177] G. Becker, "Simulation of transport in the ignition ITER with 1.5-D predictive code," Nucl. Fusion, vol. 35, 39 (1995).

[178] J. Mandrekas and W. M. Stacey, "An impurity seeded radiative mantle for ITER," Nucl. Fusion, vol. 35, 843 (1995).

[179] L. L. Lao, R. M. Wieland, W. A. Houlberg, and S. P. Hirshman, "VMOMS - a computer code for finding moment solutions to the Grad-Shafranov equation," Computer Phys. Commun., vol. 27, 129 (1982).

[180] D. Post, R. V. Jensen, C. B. Tarter, W. H. Grasberger, and W. A. Lokke, "Steady-state radiative cooling rates for low-density, high-temperature plasma," At. Data Nucl. Tables, vol. 20, 397 (1977).

[181] D. P. Stotler, "Transport simulation of a density limit in radiation dominated tokamak discharges II," Fusion Technol., vol. 22, 199 (1992).

[182] W. Park and D. A. Monticello, "Sawtooth oscillations in tokamaks," Nucl. Fusion, vol. 30, 2413 (1990).

[183] D. Post, G. Bateman, W. Houlberg, L. Bromberg, D. Cohn, et al., "Physics aspects of the compact ignition tokamak," PPPL-2389, 1986.

[184] M. Greenwald, et al., "A new look at density limits in tokamaks," Plasma Fusion Center, Massachusetts Institute of Technology, PFC/JA-8622, 1986.

[185] ITER Joint Central Teams (ed. by F. W. Perkins), "Heating scenarios for ITER 1: sustained ignition discharges," San Diego Joint Work Site, S 92 RE 1 94-08-17 F1, 1994.

[186] "ITER conceptual design report," IAEA/ITER/DS/18, 1991.

[187] F. Troyon, R. Gruber, H. Saurenmann, S. Semenzato, and S. Succi, "MHD limits to tokamak confinement," Plasma Physics and Controlled Fusion, vol. 26, 209 (1984).

[188] F. Alladio, M. L. Apicella, G. Apruzzese, R. Bartiromo, F. Bombarda, et al., "Density limit and confinement in FTU Ohmic plasma," Plasma phys. Contr. Nucl. Fusion Research, vol. 1, 141 (1992).

[189] ITER Confinement Database and Modeling Working Group, "Energy confinement scaling and the extrapolation to ITER," Presented by J. G. Cordey on the EPS meeting, June 1997.